2025
PhD thesis

Advanced multifunctional hybrid textiles via Vapor Phase Infiltration

Ana Álvarez Yenes

Supervised by
Prof. Dr. Mato Knez and Dr. Catalina Mansilla

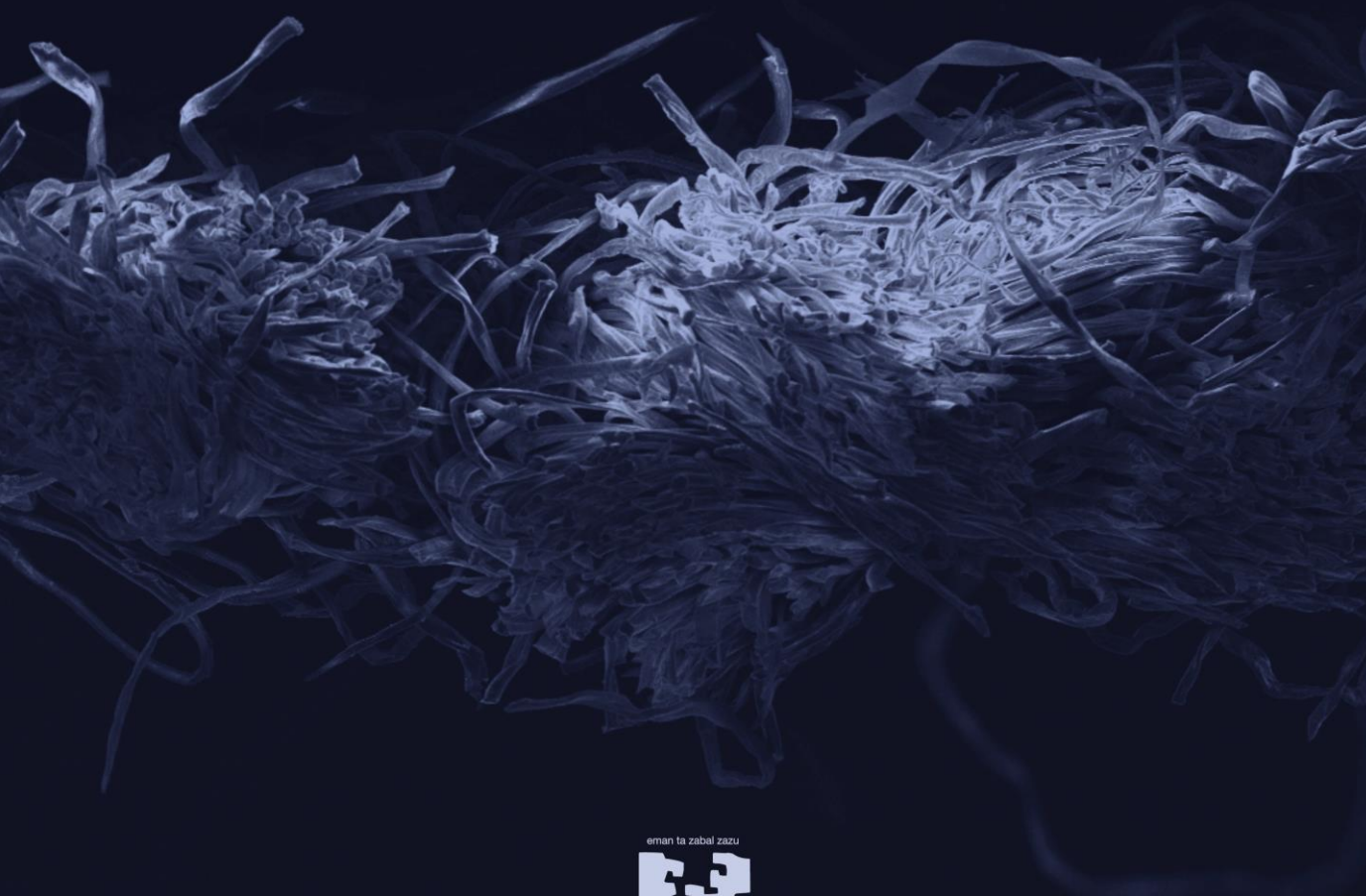

eman ta zabal zazu

Universidad del País Vasco
Euskal Herriko Unibertsitatea

2025

PhD thesis

Advanced multifunctional hybrid textiles via Vapor Phase Infiltration

Ana Álvarez Yenes

Supervised by

Prof. Dr. Mato Knez and Dr. Catalina Mansilla

eman ta zabal zazu

Universidad del País Vasco

Euskal Herriko Unibertsitatea

This PhD thesis has been carried out at:

Nanomaterials group, CIC nanoGUNE

CTECHnano Coating Technologies, S.L.

Donostia-San Sebastián, Spain.

"The most profound technologies are those that disappear.
They weave themselves into the fabric of everyday life
until they are indistinguishable from it."
- Mark Weiser

"Las tecnologías más influyentes son las que no se ven.
Se entrelazan al tejido de la vida cotidiana
hasta que se vuelven indistinguibles de ella."
- Mark Weiser

Resumen

La necesidad de obtener textiles ha sido uno de los principales motores del desarrollo tecnológico desde el surgimiento de las primeras civilizaciones. La agricultura se desarrolló para obtener fibras y alimento, la necesidad de hilo impulsó la creación de máquinas que sustituyeran el esfuerzo humano, el teñido de telas se convirtió en precursor de la química, y los patrones utilizados para tejer son considerados el antecedente matemático de la programación. Hoy en día, los textiles están tan presentes en nuestra vida cotidiana, con usos tan esenciales, que dejamos de percibirlos como tecnología y los reconocemos como una parte natural de nuestro entorno.

Las fibras de origen natural, como el algodón, el lino o la lana, se han utilizado durante siglos para fabricar textiles gracias a sus propiedades intrínsecas. Son materiales de fácil obtención, abundantes y de bajo coste, que pueden tejerse para producir tejidos ligeros, flexibles, transpirables, resistentes, biodegradables y adaptables al cuerpo humano. Este conjunto de cualidades hace de los tejidos naturales materiales casi ideales para cubrir y proteger nuestra piel, incluso por encima de muchos textiles sintéticos.

Sin embargo, las fibras naturales también presentan limitaciones que reducen su campo de aplicación. Retienen la humedad, son permeables a la radiación ultravioleta, inflamables y vulnerables a ataques microbianos, que provocan manchas y malos olores. Aunque los textiles convencionales cumplen con las funciones básicas de las telas, sus propiedades resultan insuficientes para aplicaciones avanzadas que requieren funcionalidades específicas. En este contexto surgen los textiles multifuncionales, diseñados a través de su composición, construcción o tratamientos de acabado, con el objetivo de incorporar una combinación de propiedades físicas y químicas específicas seleccionadas a medida para cada aplicación, mientras se preservan las ventajas intrínsecas de la tela original.

Los materiales híbridos, desarrollados mediante la combinación sinérgica de componentes orgánicos e inorgánicos, ofrecen una solución a estas limitaciones, ya que permiten obtener nuevos materiales con propiedades mejoradas, versátiles y ajustables. Esta estrategia permite obtener

materiales que cubren la brecha entre cerámicas y polímeros, resultando en un rendimiento superior en una amplia variedad de aplicaciones. Este concepto ya ha sido aplicado al ámbito de los textiles; sin embargo, las técnicas de síntesis actuales aún presentan limitaciones que dificultan su implementación en aplicaciones reales. La estructura porosa, deformable y tridimensional de los textiles, junto con los estrictos requisitos de apariencia, textura y durabilidad, convierten la síntesis de textiles híbridos en un desafío.

En esta tesis se ha aplicado la técnica de infiltración en fase vapor (VPI, por sus siglas en inglés) para la síntesis de textiles híbridos multifuncionales. Esta técnica, derivada de la deposición por capas atómicas (ALD), incorpora un tiempo de exposición adicional entre el pulso y la purga propios del ciclo de ALD, durante el cual los precursores se difunden en el material formando enlaces químicos tanto en la superficie como en el volumen de sustratos porosos, favoreciendo la infiltración. Como resultado, se deposita una capa delgada sobre la superficie del sustrato a la vez que se genera un gradiente subsuperficial entre el material inorgánico y el sustrato. Los procesos de VPI conservan todas las ventajas del ALD, como las bajas temperaturas necesarias para trabajar con polímeros, su versatilidad, escalabilidad y el bajo consumo de precursores. Además, la formación del gradiente infiltrado bajo la superficie minimiza las diferencias de tensión y esfuerzo asociados al movimiento y doblado de las fibras, lo que permite preservar la flexibilidad original de los textiles y mejorar la durabilidad de las funcionalidades incorporadas. Un valor añadido del VPI es que posibilita la funcionalización de fibras textiles a través del tratamiento de tejidos ya confeccionados, lo cual resulta especialmente valioso en el caso de las fibras naturales.

El potencial del VPI para la síntesis de textiles híbridos orgánicos-inorgánicos aún no ha sido explorado. El objetivo de esta tesis es desarrollar y caracterizar tejidos híbridos multifuncionales mediante la infiltración de óxido de zinc (ZnO) y dióxido de titanio (TiO_2) en sustratos basados en el algodón. Estos óxidos metálicos han sido seleccionados por su capacidad para absorber radiación ultravioleta y por sus conocidas propiedades fotocatalíticas y antimicrobianas que, en combinación con su excelente estabilidad y biocompatibilidad, los convierten en materiales

idóneos para su incorporación en textiles híbridos. Adicionalmente, estos óxidos presentan la ventaja de poder ser depositados mediante ALD a bajas temperaturas empleando precursores estándar, económicos y fácilmente obtenibles.

Se han seleccionado dos tipos de tejidos basados en el algodón como sustratos. El primero corresponde a un algodón natural sin blanquear, la tela tejida de algodón más natural que se puede obtener, con una composición de 100% algodón. El segundo es un tejido vaquero comercial, compuesto por una mezcla de 50% algodón, 44% polietileno, 5% elastomultiéster y 1% elastano.

Se ha desarrollado y optimizado un proceso de VPI estándar para la infiltración simultánea de tres muestras de tela de 5x5 cm^2. Los parámetros de procesado se seleccionaron atendiendo a las limitaciones impuestas por la resistencia térmica de los sustratos, la posible degradación química y la necesidad de garantizar una infiltración homogénea en toda la cámara del reactor.

En el primer capítulo experimental de esta tesis doctoral (**Capítulo 3**), se caracterizó la estructura y composición de las fibras que conforman ambos tejidos antes y después de la infiltración, con el fin de confirmar la modificación exitosa de los polímeros. Las imágenes y el mapeo químico de la sección transversal de las fibras, obtenidas mediante SEM y EDX, muestran que el proceso de VPI desarrollado permite el crecimiento de los óxidos metálicos dentro de los hilos entretejidos, infiltrando individualmente cada una de las fibras que los forman. Se cuantificaron los átomos de Zn y Ti en los tejidos híbridos preparados, concluyendo que el algodón natural permite una mayor infiltración de los óxidos metálicos que el tejido vaquero. Las medidas de difracción de rayos X indican que la infiltración no altera el orden estructural de los polímeros textiles, el ZnO infiltrado crece en su fase cristalina wurtzita con la celda unidad comprimida, mientras que el TiO_2 crece en fase amorfa. Finalmente, se realizaron ensayos de tracción uniaxial para asegurar que el proceso de infiltración no deteriora las propiedades mecánicas de los tejidos.

El segundo capítulo experimental (**Capítulo 4**) se centra en la evaluación de las funcionalidades adquiridas por los tejidos mediante la infiltración.

Los resultados confirman que propiedades como la foto protección, la auto limpieza a través de fotocatálisis e hidrofobicidad, la actividad antimicrobiana y anti-olor, así como el retardo de la llama pueden incorporarse en los textiles a través de un único proceso de VPI.

La protección frente a la radiación ultravioleta dañina se logró ampliando la absorción de los tejidos hacia las regiones UVA y casi visible. La actividad auto limpiante química del algodón infiltrado con ZnO se evaluó mediante la foto degradación de rodamina B bajo luz solar simulada, demostrando que los tejidos híbridos podían degradar repetidamente el colorante orgánico sin pérdida de eficiencia. La autolimpieza física se estudió a través de la medición del ángulo de contacto. El algodón natural mantuvo su hidrofobicidad original tras la infiltración, mientras que el tejido vaquero pasó de ser super hidrofílico a hidrofóbico, alcanzando ángulos de contacto superiores a 120°. Además, las gotas permanecieron sobre la superficie del tejido sin ser absorbidas entre varios minutos y más de una hora. La combinación de actividad fotocatalítica y repelencia al agua dota a los tejidos híbridos de capacidad para autolimpiarse.

La actividad antibacteriana se evaluó frente a las cepas modelo *S. aureus* y *E. coli*, así como frente a la cepa *C. striatum*, causante del mal olor corporal, logrando una actividad bacteriostática sin lixiviación que impidió la adhesión y proliferación bacteriana sobre los tejidos. La actividad antifúngica de los tejidos infiltrados con ZnO se estudió frente al hongo modelo *A. nidulans*, mostrando actividad antifúngica parcial, efectiva inhibiendo la germinación de esporas, pero no el crecimiento de hifas.

La resistencia al fuego se evaluó exponiendo los tejidos híbridos a una llama abierta y analizando visualmente su comportamiento durante la combustión. Se observó un retraso significativo en el tiempo de ignición y una rápida autoextinción de la llama, minimizando los daños causando por el fuego en el tejido y suprimiendo la generación de humo.

La durabilidad de las funcionalidades obtenidas se evaluó comparando la foto protección y la actividad antibacteriana de los tejidos híbridos antes y después de someterlos a repetidos programas de lavado convencionales. Los resultados demostraron que los tejidos infiltrados con ZnO

conservaron sus funcionalidades, mientras que aquellos infiltrados con TiO_2 experimentaron una pérdida parcial de rendimiento.

El tercer capítulo experimental (**Capítulo 5**) está dedicado a la evaluación de la percepción humana de los tejidos tras la infiltración. Los cambios en la percepción visual se identificaron mediante mediciones de color en el espacio CIELAB. Todas las muestras, excepto los tejidos vaqueros infiltrados con 300 ciclos de ZnO, se mantuvieron dentro de los umbrales aceptables de variación cromática. Adicionalmente, los tejidos de algodón tratados con hasta 80 ciclos de infiltración de ZnO resultaron visualmente indistinguibles de los tejidos originales. La percepción táctil se analizó mediante la combinación de mediciones de fricción y movimiento de la yema del dedo con un estudio de muestra intrusa (*Odd Sample Out*) realizado con 30 voluntarios. Los resultados mostraron que los tejidos infiltrados con menos de 80 ciclos se percibían, en general, como idénticos a los tejidos sin tratar, mientras que aquellos tratados con 80 ciclos o más fueron distinguidos por al menos el 50% de los participantes. El coeficiente de fricción aumentó con el número de ciclos de infiltración; sin embargo, el análisis de diferencias de fricción reveló que algunas muestras podían identificarse como diferentes incluso sin un aumento medible de dicho coeficiente. Un análisis más detallado de los atributos sensoriales confirmó que la textura y la estructura de los tejidos también se modificaron durante el proceso de infiltración, volviéndose más lisos y rígidos al tacto.

La combinación de ambos estudios permite determinar la cantidad óptima de cada óxido metálico a infiltrar y aplicar este conocimiento al uso del VPI con el fin de obtener tejidos con múltiples funcionalidades nuevas sin comprometer su aspecto ni su tacto originales.

Los dos últimos capítulos de esta tesis presentan trabajo adicional realizado fuera del ámbito de los tejidos híbridos. El **Capítulo 7** está dedicado a la deposición por ALD a bajas temperaturas, entre 100 y 275°C, de nitruro de boro utilizando la descomposición de carbamato de amonio como fuente de nitrógeno. Finalmente, el **Capítulo 8** resume el trabajo de investigación e innovación realizado en un entorno industrial, como parte de la empresa CTECHnano Coating Technologies S.L., en el marco de un doctorado industrial.

Abstract

Textiles form an essential part of our daily lives, having become so common that we no longer perceive them as technology. Natural textile fibers provide multiple advantages, often outperforming synthetic alternatives, yet their capabilities become insufficient in applications that demand advanced, highly specific functionalities. Hybrid materials combine organic and inorganic components to create systems with enhanced and tunable properties, offering a route to overcome these limitations. This concept has already been applied to textiles; however, the existing synthesis techniques still face drawbacks that hinder their implementation in real-world applications.

In this thesis, multifunctional cotton-based hybrid textiles were developed via Vapor Phase Infiltration (VPI), a technique that enables the incorporation of inorganic materials, specifically ZnO and TiO_2, both at the surface and within the bulk of textile fibers, forming strong chemical bonds with the organic matrix. A process was established to treat macroscopic pieces of woven fabric, achieving the uniform infiltration of all individual fibers. The functional properties of the resulting hybrid textiles were characterized, demonstrating the successful, durable integration of photoprotective, self-cleaning, antimicrobial, and flame-retardant capabilities through a single VPI treatment. The visual and tactile perception of the fabrics were assessed to ensure the preservation of the original aesthetic appeal and physical qualities of the fabrics.

This work, conducted as part of an industrial PhD, aims to bridge scientific research and industrial applications by developing washable, durable hybrid textiles through a single, scalable VPI process, thereby advancing the implementation of VPI for multifunctional textile development in industrial settings.

Table of contents

1

Introduction to multifunctional organic-inorganic hybrid textiles

The story of textiles is the story of human invention. Since the first thread was spun, the need for textiles has been a driving force behind technological advancement. Agriculture was developed to cultivate food and fiber crops. The demand for threads sparked the invention of machines that reduced manual labor, leading to the Industrial Revolution. Fabrics turned the first dyers into chemists, while the logic and patterns needed for weaving are considered the mathematical antecessor of modern programming [1]. From the moment we are born and wrapped in a blanket, we are surrounded by textiles. We use them to cover our bodies, beds, and homes. They provide shelter and protection in the form of camping tents, seatbelts, sanitary masks, and even allow us to survive in outer space. Textiles are everywhere, so essential and familiar that they are rarely perceived as technology, but rather as a natural part of our surroundings.

Conventional textiles serve the basic functions of clothing, covering the human body and providing protection, comfort, and decoration, while functional textiles are engineered through their composition, construction, or finishing to possess specific physical or chemical properties in addition to the inherent characteristics of regular textiles [2]. Furthermore, multifunctional textiles are designed to achieve a combination of various properties tailored to specific applications while preserving comfort, flexibility, and aesthetics. Commonly sought after functionalities include UV protection, self-cleaning properties, moisture management,

antimicrobial activity, flame retardance, electrical conductivity, thermal regulation, and sensing capabilities.

1.1. Hybrid materials

The goal of materials science is to develop and optimize material properties for a specific purpose needed for the advancement of technological applications. While many traditional applications can be met with existing materials, emerging technologies increasingly demand properties that are not intrinsically found in any conventional material. In some cases, typical characteristics of polymers are required alongside those of metals or ceramics. Therefore, combining multiple elements, compounds or materials while preserving the beneficial aspects of each component becomes necessary [3].

At the macroscopic scale, composite materials achieve this by combining organic and inorganic phases while maintaining the integrity of each phase. Hybrid materials come from the extension of this concept into the micro and nanoscales. Although no exact definition of the term *hybrid material* exists, it typically describes materials obtained through the synergistic blend of selected organic and inorganic compounds, where each component contributes to the overall performance of the final material in a beneficial way, resulting in a unique combination of properties. With this strategy, materials that cover the gap between the worlds of ceramics, metals, polymers, and organics can be obtained, resulting in improved performance in a wide variety of applications.

Two classifications are commonly used to identify hybrid materials. The most used one is based on the type of interactions between the organic and inorganic components. *Class I* hybrids are formed through weak interactions including hydrogen bonds, Van der Waals, and weak electrostatic interactions, while *class II* hybrids are based on strong chemical interactions such as covalent or ionic bonds. The second classification attends to the nature of the structural matrix and hosted components. A hybrid material is organic-inorganic when the matrix is an organic phase with integrated inorganics, and inorganic-organic when there is an inorganic host with added organic guests [4].

Hybrid materials composed of a soft organic matrix with hard inorganic additions have been present in nature long before humans even existed. Bone, composed of a collagen matrix intermixed with calcium-based minerals, is one of the prominent examples. The combination of lightness, elasticity and toughness obtained from the mixture of materials enables our bodies to withstand the stress of movement. Similar natural hybrids include nacre and ivory, which form the protective shells and fangs of animals [5].

Humans have always taken inspiration from nature and have mimicked hybrid materials, consciously or not, to fulfill their needs since the Paleolithic. Indeed, the first humans already mixed organic fluids like blood and grease with inorganic pigments like rust to paint their caves. Thousands of years later, the Mayans produced a blue pigment called *Maya Blue* from the combination of indigo natural dye and clay [6]. The resulting pigment has been preserved over centuries thanks to its remarkable chemical stability and resistance to sunlight radiation and high temperatures. Around the same period, Chinese artisans improved the plasticity of kaolin clay by adding urea, which enabled the creation of porcelain with extremely thin walls [7]. In these cases, the creation of hybrid materials with improved properties was fortuitous.

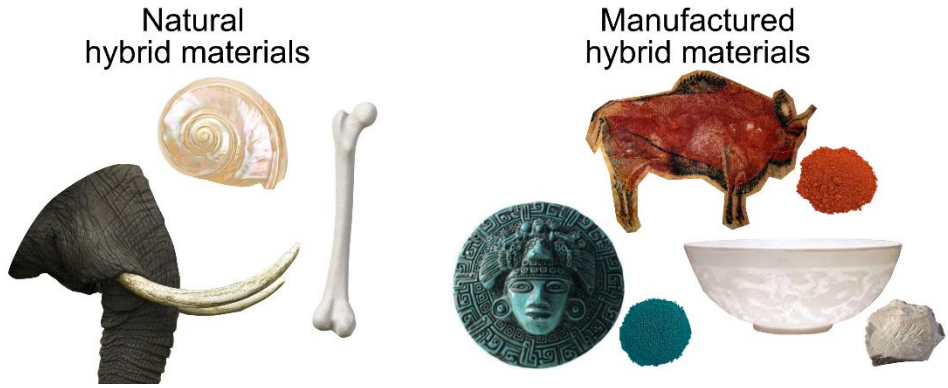

Figure 1.1. Examples of natural (nacre [8], ivory [9], and bone [10]) and manufactured ancient hybrid materials (prehistoric pigments [11], Maya Blue [12], and Chinese porcelain [7]).

It was not until the 20th century that the intentional synthesis of a hybrid organic-inorganic material was first reported. In 1996, Belfiore et al. combined two diene polymers, widely used in tires, automotive parts, and protective gear, with palladium salts, resulting in materials with enhanced

resistance and altered solubility [13]. In the last years, the study of hybrid materials has expanded so rapidly that some types of hybrid materials like intercalated materials, perovskites or metal-organic frameworks (MOFs) have consolidated as new specialized fields within materials science [4]. These examples demonstrate that hybrid materials can be intentionally designed and synthetized to exhibit exceptional properties suitable for emerging technologies.

1.2. Multifunctional textiles

Natural fibers such as cotton, flax, silk and wool, have been used in textiles for centuries due to their numerous interesting innate advantages. They are readily available from plants and animals in a low-cost and abundant manner, and can be woven into fabrics that are lightweight, flexible, breathable, mechanically strong, non-toxic, biodegradable, and highly adaptable to the human body. These merits make them almost ideal materials to cover and protect our skin. However, natural fibers have inherent limitations in their usability. They absorb moisture, have poor chemical and fire resistance, are permeable to UV radiation, susceptible to mechanical damage during washing, and vulnerable to microbial attacks, which lead to stains and odor. These characteristics, although acceptable for traditional applications, limit the development of more advanced, functional uses [14].

The introduction of hybrid materials offers a pathway to achieve multifunctional fabrics that maintain the benefits of natural fibers while overcoming their weaknesses. By combining them with other functional materials, it is possible to produce multifunctional textiles with new tunable, enhanced, and versatile properties that are better suited for demanding applications.

1.2.1. Functional materials

A wide variety of functional materials have been incorporated into pristine fabrics to develop hybrid textiles with various functionalities that improve their original performances.

Bio-based functional materials have been applied for textile enhancement since ancient times, when the Egyptians used spices and herbal coatings on cloth to prepare antimicrobial mummy wraps [15]. Today, biopolymers such as chitosan and lignin, or various essential oils, are incorporated into fabrics to make them antimicrobial. In addition, functionalization of textile surfaces by enzyme immobilization became a very popular technique in the textile industry, imparting long lasting functionalities such as controlled wettability and shrink resistance [16].

The earliest modern hybrid textiles arise from the combination of conventional textile fibers with functional fibers through mechanical interlocking. Examples of such functional fibers include carbon, glass, and aramid fibers. These materials focus on the reinforcement of the mechanical and thermal resistance of the textile while remaining lightweight and are mainly applied in sectors such as the construction and the automotive industry [17].

Another approach to textile functionalization involves the incorporation of synthetic polymeric materials that impart specific, desirable properties to the fabrics. Conductive polymers such as polypyrrole (PPy) [18] and polyaniline (PANI) [19] are used for their electrical conductivity, making them suitable for applications in wearable electronics and sensors. Other polymers, like polyurethane (PU) and silicones contribute to waterproofing fabrics while preserving their breathability. Fluoropolymer coatings such as PTFE repel both water and oil, producing durable stain-resistant textiles [20].

Carbon-based nanomaterials are among the most researched areas for high-performance nanocomposite coatings due to their high aspect ratio, unique conductivity, and mechanical properties. They have remarkable potential for advanced textile applications, however, their integration into fabrics remains a challenge due to their poor dispersion in polymeric media and the need for additional binding components to adhere to textile surfaces. As a result, current research is focused on the functionalization strategies needed to improve their compatibility rather than on their functionalities [21].

The functionalization of textiles with metal and metal oxide nanoparticles is one of the most studied strategies for the incorporation of multiple functionalities into a single fabric. Silver (Ag) and copper (Cu) nanoparticles are used for their antimicrobial and antiviral properties. Zinc oxide (ZnO) and titanium dioxide (TiO_2) nanoparticles integrate UV protection and photocatalytic self-cleaning under light exposure. Other oxides, such as iron oxide (Fe_3O_4), provide magnetic response, while aluminum oxide (Al_2O_3) enhances mechanical resistance and thermal stability [22].

1.2.2. Functionalization strategies and challenges

The porous, deformable, and high aspect-ratio structure of textiles, combined with strict requirements for appearance, texture, and durability in multifunctional textiles, makes the incorporation of functional materials considerably challenging. Given the determining effect of the processing techniques on the final materials, fiber functionalization has been extensively explored. Although many synthetic methods exist, functionalization is usually based on either of two strategies: fiber functionalization or textile functionalization [14].

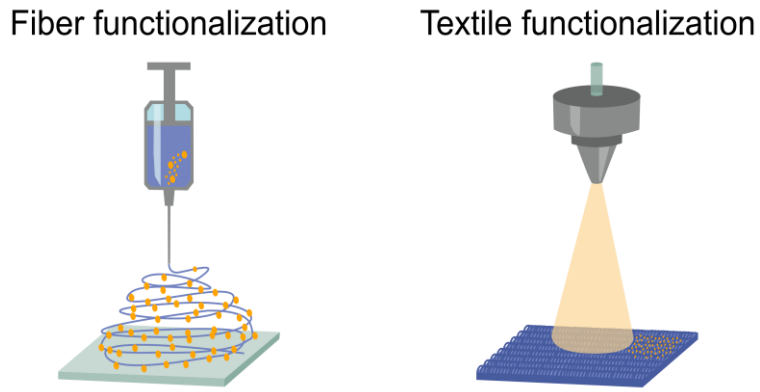

Figure 1.2. Schematics of the two functionalization strategies: fiber and textile functionalization.

In the first strategy, the functional materials are incorporated during the fabrication of the fibers that will later form the textile. In this process, the fiber is produced by extruding a spinnable liquid into a continuous stream,

which is then solidified in analogy to the way spiders and silkworms produce their threads. The resulting fibers can then be woven into textiles. This group of techniques, known as spinning techniques, includes melt spinning, wet spinning, microfluidic spinning, electrospinning, thermal drawing, blow spinning, and solution extrusion. These methods have been used to embed functional materials like PANI, PPy, carbon nanotubes or metal colloids into synthetic polymers. However, they remain limited in terms of mechanical strength and durability, and their applicability to natural textile fibers is considerably constrained.

The second strategy, known as surface modification, involves adding functional materials directly onto the formed textiles through coating or deposition methods. One of the most common coating methods is dip coating, in which the fabric is immersed in a solution of the coating material. Alternatively, in spray coating, the solution is atomized into droplets, deposited onto the textile, and followed by a curing process. These methods are easily scalable, but have problems in the uniformity of the coatings, and can alter the breathability and feel of the fabrics. Deposition techniques, on the other hand, rely on controlled chemical reactions to form chemical bonds between the abundant functional groups of the textiles and the functional materials, achieving a more durable functionalization. Examples include chemical bath deposition, hydrothermal reaction, electrodeposition, Physical Vapor Deposition (PVD), and Chemical Vapor Deposition (CVD). Atomic Layer Deposition (ALD), a variant of CVD, has recently emerged as a promising textile functionalization technique due to its precise thickness control, excellent conformality, low processing temperatures, and minimal precursor consumption [23].

Despite the variety of available functionalization techniques, some important issues still need to be addressed to achieve practical utilization. The adhesion of the functional materials on the textiles is generally weak, even when chemical bonds are formed. Textiles are flexible materials that are constantly folded, bent, twisted, and pressed. Moreover, they must withstand regular laundering processes without a significant loss of their functionalities, making durability and washability critical issues. Another concern comes from the potential toxicity of certain functional

nanomaterials, which may pose risks to both human health and the environment. Ensuring the safety and biocompatibility of functional textiles is therefore essential, given their prolonged close contact with the skin [14].

1.3. Vapor Phase Infiltration

Vapor Phase Infiltration (VPI) is a vapor-to-solid technique for the synthesis of organic-inorganic hybrid materials. This process derives directly from ALD. It aroused when researchers attempted to grow thin films on the surface of polymeric materials by ALD. Polymers are porous on the molecular scale so that many of the precursor vapors used in ALD can diffuse into the substrate, leading to subsurface growth. This result, initially considered an inconvenience, was later found to enhance various properties of polymers [24]. The potential of VPI for improving the mechanical strength and toughness of spider silk was first reported in 2009 by the Knez group [25]. Since then, various researchers have demonstrated the enhanced properties of organic–inorganic hybrid materials synthetized by VPI, including stronger cellulosic fibers, more etch-tolerant photoresists, and more efficient hybrid solar cells. The research groups involved developed variations with different process parameters and names, including Sequential Infiltration Synthesis (SIS), Multiple Pulsed Infiltration (MPI), Sequential Vapor Infiltration (SVI), or Atomic Layer Infiltration (ALI). However, these various terminologies describe effectively the same process and can be unified under the term VPI [26].

To promote precursor infiltration into soft substrates, an exposure step is added between the pulse and purge steps of a typical ALD cycle, allowing sufficient time for the precursors to diffuse into the material bulk. A VPI cycle begins with pulsing of the first precursor into the reactor, followed by an extended exposure step, and then purge with an inert gas to remove excess precursor and byproducts. The same sequence is repeated with the second precursor, completing one cycle. In this way, the polymeric substrate is sequentially exposed to two precursors which alternatively infiltrate the substrate and undergo chemical reactions. The first precursor

binds to functional groups both on the surface and within the bulk of the substrate, while the second precursor reacts with the first bound precursor also in both regions. As a result, a thin film is deposited on the substrate surface while the bulk is infiltrated, forming a gradient from the polymer to the inorganic material below the surface. The self-limiting characteristic of ALD is lost for the growth of the hybrid material inside the substrate; however, the depth and density of this gradient can be controlled through the processing temperature, exposure time, and number of cycles.

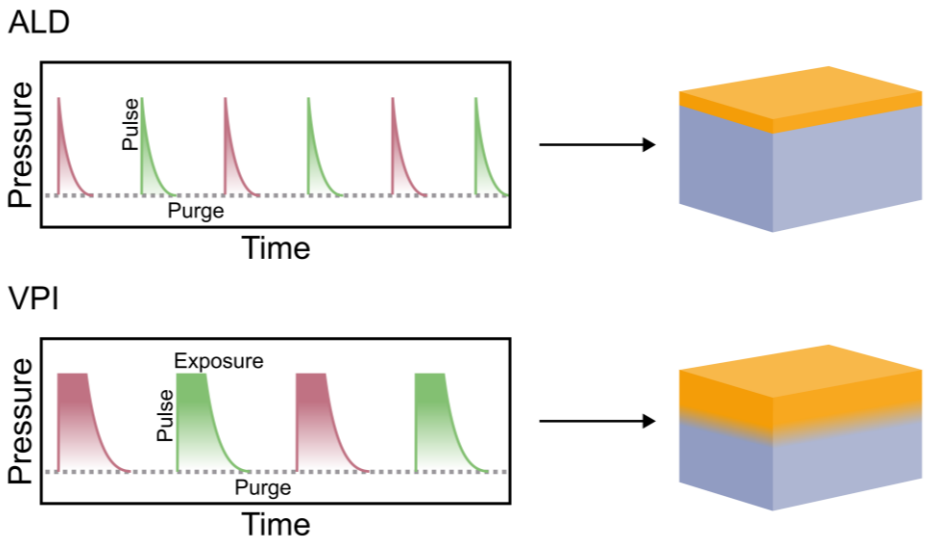

Figure 1.3. Schematic comparison of the pressure profiles and resulting structures of typical ALD and VPI processes.

VPI retains all other advantages of ALD, including low processing temperatures required when working with organic polymers, versatility, and minimal precursor consumption. Moreover, it enables the functionalization of textile fibers by directly treating finished fabrics, effectively combining the two main functionalization strategies. This is especially valuable in the case of natural textile fibers, which have been a significant challenge for spinning techniques. Finally, the durability of the functionalization is improved through the subsurface, in which the inorganic and organic materials gradually merge. This gradient reduces the differences in strain during bending, folding, and twisting of the fibers,

maintaining the flexibility of the hybrid materials, and preserving their functional properties [27].

1.4. Motivation and structure of the thesis

The potential of VPI for the synthesis of organic-inorganic hybrid textiles has not yet been explored. This thesis aims to develop and characterize multifunctional hybrid fabrics through VPI, by infiltrating ZnO and TiO_2 into cotton-based textiles, while maintaining their original aesthetics and feel.

Cotton is a natural fiber, known for its soft and comfortable feel. It is one of the most affordable natural textiles, durable, easy to care for and wash. This combination of properties makes cotton a great option for a wide range of applications, from clothing to household items, even when compared with many technical synthetic fibers.

ZnO and TiO_2 are widely used metal oxides, easily deposited by ALD at low temperatures using standard precursors. Both ZnO and TiO_2 are stable materials and have shown excellent biocompatibility, making them good functional materials for hybrid textiles. They absorb UV light, are effective photocatalysts and present antimicrobial properties [28], [29], [30], [31], [32], [33], [34], [35]. All these functionalities can be incorporated into cotton-based textiles to obtain multifunctional organic-inorganic hybrid textiles with a single VPI process.

Chapter 2 details the experimental techniques and methods used for the synthesis and characterization of hybrid textiles.

Chapter 3 focuses on the characterization of the structure and composition of the fabrics before and after infiltration. A comparison of the durability of the structures obtained by VPI with those obtained by ALD is provided.

Chapter 4 is dedicated to the evaluation of the functionalities of the hybrid textiles including UV protection, chemical and physical self-cleaning, antimicrobial activity, and flame retardance. The resistance of the functionalization against regular laundering is tested.

Chapter 5 evaluates the human visual and tactile perception of the hybrid fabrics. Color measurements, fingertip friction and an *Odd Sample Out* perceptional task are combined to identify the minimum perceivable amount of the infiltrated metal oxides.

Chapter 6 compiles the main conclusions and prospects of this work.

The last two chapters in this thesis describe additional work carried out besides the fabrication of hybrid textiles:

Chapter 7 is dedicated to the low temperature Atomic Layer Deposition of nitrides using the in-situ decomposition of ammonium carbamate as nitrogen source.

Chapter 8 summarizes the research and innovation work done in an industrial setting, as part of the company CTECHnano Coating Technologies S.L., in the framework of an industrial PhD.

2

Experimental techniques and methods

In this thesis, VPI has been utilized to synthesize hybrid organic-inorganic textiles. This chapter details the materials and conditions used in their fabrication, as well as the experimental techniques and protocols applied for their characterization and for the investigation of their resulting functionalities. The experimental techniques and methods are listed in order of appearance in the following chapters.

2.1. Substrates, precursors, and VPI conditions

Two different types of cotton-based woven fabrics were selected as substrates for the infiltration:

- Natural raw cotton fabric, unbleached. This is the most untreated form of cotton that can be obtained in fabric form, with a composition of 100% cotton.
- Commercial jeans fabric, obtained from Andromeda, a company in Vitoria-Gasteiz. The fabric had a blended composition of 50% cotton, 44% polyethylene, 5% elastomultiester and 1% elastane.

Both types of fabrics were infiltrated with zinc oxide (ZnO) and titanium dioxide (TiO_2). Diethylzinc ($Zn(C_2H_5)_2$, DEZ) was used as the zinc source and titanium tetrachloride ($TiCl_4$) as the titanium source. In both processes purified water (H_2O) was used as the oxygen source. The precursor selection was based on their reactivity, availability, and price, selecting

widely studied ALD precursors with higher deposition rates with the aim of optimizing an infiltration process suitable for industrial application.

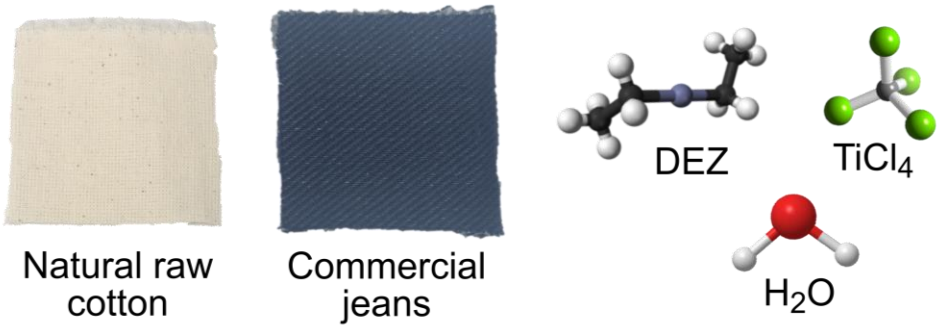

Figure 2.1. Images of the fabrics and chemical structures of the precursors used.

The VPI processes were carried out interchangeably in a Savannah reactor from Cambridge Nanotech or a PLAY reactor from CTECHnano. Both reactors have a controllable vacuum valve between the reaction chamber and the pump which allows VPI processing in a stop flow regime. Initially, the temperature-resistance of the fabrics was tested by heating them in the reaction chambers. Natural raw cotton withstands temperatures over 150°C, while the dye in commercial jeans started to degrade at 120°C. Tests at different temperatures below these respective upper limits were carried out to analyze the induced chemical damage to the fibers and to avoid significant changes to their appearance. Based on the results of the thermal testing, the processing temperature was set to 60°C for the case of ZnO infiltration and 100°C for the case of TiO_2 infiltration for both fabrics. All precursors were kept at room temperature. A continuous flow of nitrogen (N_2) of 20 standard cubic centimeters per minute (sccm) was supplied to the reactor chamber during the entire VPI process to prevent backflow of the precursor into the manifold. First, the corresponding metalorganic precursor was pulsed for 40 ms into the reaction chamber and kept inside for 40 s to allow precursor diffusion and infiltration into the polymer. This exposure step was followed by 60 s of purging to remove any unreacted precursors and reaction by-products. The same steps were repeated for H_2O to complete one VPI cycle. The total number of cycles was varied from 5 to 600. The fabric samples were suspended in the chamber in a way that allows both faces of the fabric to be exposed to the precursors. Typically, three fabric pieces of 5x5 cm^2 each were simultaneously infiltrated in one

process. Thermally oxidized silicon substrates were placed into the reaction chamber to serve as references for deposition homogeneity. These are the standard VPI conditions used throughout this thesis, tweaking of the processing conditions to adapt to different sample sizes or analysis requirements are indicated in the corresponding sections.

2.2. Scanning Electron Microscopy (SEM) and Energy Dispersive X-Ray spectroscopy (EDX)

Electron microscopy is one of the most applicable investigation and visualization techniques for VPI-modified polymers. The interaction of the electrons with atoms in the samples allows to obtain high spatial resolution, in the nanometer range, and in-situ chemical characterization of the samples, which are key for the detection of the infiltrated inorganic materials.

In SEM, an accelerated electron beam scans across the sample surface line by line. At each surface spot, the electrons from the e^--beam interact with the sample. The detection of these interaction events enables topological or compositional imaging of the sample. The interaction mechanisms analyzed for the characterization of the hybrid textiles in this thesis are schematically depicted in **Figure 2.2**.

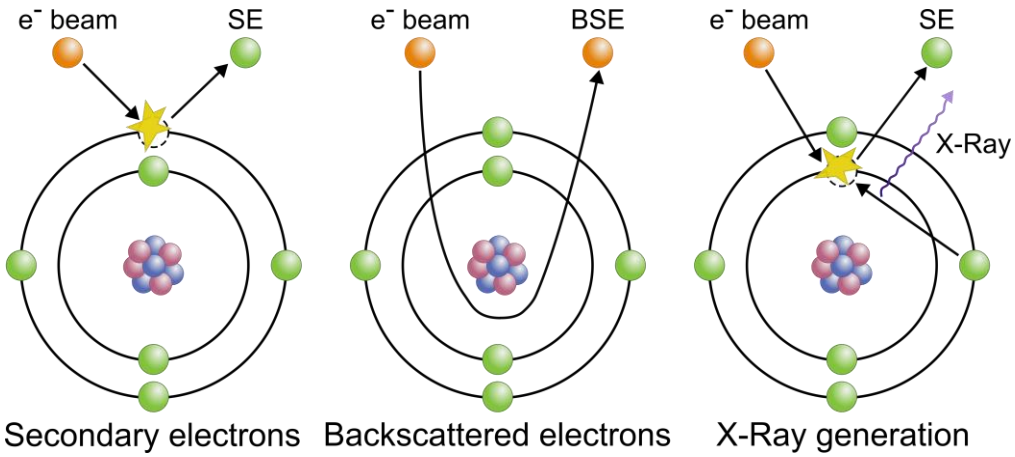

Figure 2.2. Schematics of the mechanisms for the emission of secondary electrons (SE), backscattered electrons (BSE), and characteristic X-Rays during SEM.

Secondary electrons (SE) are low-energy electrons emitted from atoms on the sample surface due to inelastic collisions with the primary beam. SEs possess high spatial resolution but do not carry information about the elemental composition. They are highly sensitive to surface topography and are therefore used to perform high-resolution imaging [36]. Backscattered electrons (BSE) are high-energy electrons from the beam that are elastically backscattered by the sample undergoing a wide-angle directional change. The probability of backscattering depends on the mass of the atomic nuclei. Therefore, BSE can be used to obtain compositional information but with lower spatial resolution [37]. Beam electrons can also excite an electron from an inner shell, leaving an electron hole. This vacancy is filled by an electron from the outer shell, generating an X-Ray photon of an element-characteristic energy. The generated X-Rays can be collected with an energy-dispersive spectrometer to obtain an elemental analysis of the sample.

SEM and EDX measurements were performed to investigate the surface morphology of the fibers before and after infiltration and to spatially resolve their chemical composition to confirm successful infiltration. A FEI Quanta 250 FEG scanning electron microscope was used for this purpose. An Everhart-Thorney detector (ETD) and a large field detector (LFD) were used for the collection of SE in high and low vacuum, respectively. A low voltage high-contrast detector (vCD) was used for the collection of BSE. EDX maps were taken with an EDAX Octane Elect Plus detector at an accelerating voltage of 10 keV.

2.2.1. Cross-section preparation

Cross-section imaging of the fibers is necessary to confirm the infiltration in subsurface areas of the sample. However, cross-sections of cotton fibers are difficult to obtain since they are delicate and easily damaged during cutting. A focused ion beam (FIB) could not be applied for the cross-section preparation since the interaction between the fibers and the ions caused new features, like cavities, in the samples. The infiltration depth is on the order of 100 nm, making it impossible to distinguish between induced damage and infiltration.

Therefore, two alternative strategies were used for the preparation of the cross-sections:

1. Macroscopic pieces of woven fabrics were cut with a sharp scalpel to obtain a cross-section for both optical and electron microscopy. These samples were used to analyze the surface texture of the fabrics and to obtain EDX mapping of the complete threads.

2. Encapsulation of individual threads in resin to further reduce fiber damage during cutting, and subsequent cut with a microtome. The cross-sectioned surface was polished after cutting. These samples were used to obtain high-resolution images of the individual fibers that form the threads. Chemical resolution was obtained by backscattered electrons imaging since the addition of the resin and the high magnification noticeably deteriorate the resolution and accuracy of the EDX mapping.

2.3. Attenuated Total Reflection Fourier Transform Infrared spectroscopy (ATR-FTIR)

ATR-FTIR is an analytical technique that identifies functional groups in a sample by analyzing their interaction with infrared light. When the sample is irradiated, specific wavelengths of infrared light are absorbed, leading to the excitation of chemical bonds into higher vibrational energy states. These absorption bands are characteristic of specific chemical bonds and can be used to determine the functional groups present in the sample [38].

ATR-FTIR was used to investigate the chemical composition of pristine fabrics. The ATR-FTIR spectra were measured with a PerkinElmer Frontier spectrometer equipped with an ATR sampling stage. All spectra were measured in transmittance mode with 10 scans from 600 to 4000 cm^{-1} and a resolution of 1 cm^{-1}.

2.4. Inductively Coupled Plasma – Optical Emission Spectroscopy (ICP-OES)

ICP-OES is used to identify and quantify the elemental composition of a sample. A liquid sample is nebulized into a high-temperature plasma, which provides the energy needed to break the sample molecules into atoms and ions, and to excite their electrons to higher energy states. When these electrons return to a lower energy state, light of a specific wavelength is emitted. The wavelengths of these emission lines are characteristic to each element, while their intensities are proportional to the element's concentration, serving as a fingerprint for both identification and quantification [39].

ICP-OES was used to determine the weight percentage of metal atoms in the hybrid textiles. ICP-OES measurements were done by the Chemical Analytics group at the Leibniz Institute for New Materials (INM) in Saarbrücken, Germany. Circular samples of 1 cm in diameter were cut from infiltrated pieces of fabrics of 5x5 cm^2 and dissolved in 4 mL of H_2SO_4 (conc.) and 7 mL of H_2O_2 (>30%) at 260°C in a chemical digestion equipment from Hach. A Horiba Jobin Yvon Ultima2 spectrometer with a Conikal concentric nebulizer was used. The pressure was set to 2.40 bar and the flow to 1.82 L/min.

2.5. X-Ray Diffraction (XRD)

XRD uses the interferences of X-Rays interacting with a sample to provide detailed information about its crystallographic structure. When a monochromatic X-Ray beam reaches the atoms in the sample, the X-Rays are scattered [40]. The scattered rays interfere with one another, producing constructive interferences only when the conditions satisfy Bragg's law (schematized in **Figure 2.3**):

$$n\lambda = 2d \sin\theta \tag{2.1}$$

where λ corresponds to the wavelength of the X-Ray beam, d to the spacing between diffracting planes and θ to the incident angle of the beam. When scanning over a range of incident angles, the constructive interferences

result in a diffraction pattern formed by a series of peaks of varying intensities which characterize the structure of the sample. The Debye-Scherrer formula is used to estimate the average crystallite size by analyzing the broadening of crystalline diffraction peaks in XRD patterns:

$$D = \frac{K\lambda}{\beta \cos\theta} \tag{2.2}$$

where D corresponds to the average grain size, K to the Scherrer constant, typically with a value of 0.9, λ to the wavelength of the X-Ray beam, β to the full width at half maximum (FWHM) of the diffraction peak and θ to the incident angle of the beam.

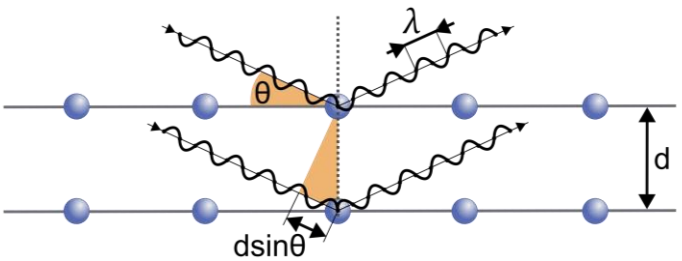

Figure 2.3. Schematic of Bragg's diffraction principle.

XRD was used to determine the crystallographic structure of the infiltrated metal oxide, including their unit cell parameters and mean crystallite sizes. For that purpose, a fabric sample of approximately 2x2 cm^2 was repeatedly cut with a guillotine until powdered. The obtained powder was compressed into a pellet, placed on an amorphous Si disk to reduce background contributions, and measured in gonio mode. The XRD measurements were carried out with a PANalytical X'Pert Pro diffractometer using a *Cu Kα* (λ=0,154 nm) radiation source with a working voltage and current of 45 kV and 40 mA, respectively.

2.6. Uniaxial tensile tests

Uniaxial tensile tests analyze the behavior of a sample when subjected to an external stretching force until its rupture. One end of the sample is clamped to a fixed grip while the other end is clamped to a sliding one, which moves parallel to the sample axis at a constant velocity. The stress σ

is calculated by dividing the applied force by the cross-sectional area of the sample. The strain ε is defined as the relative elongation of the sample in the direction of the applied force. The resulting stress-train curves provide information about maximum force and deformation that the samples withstand, their yield strength and the reversibility, that is, elasticity or plasticity of their deformation.

Uniaxial tensile tests were used to verify the conservation of the mechanical properties of the pristine fabrics after infiltration. These tests were done by collaborators at the Technology Centre GAIKER. Uniaxial tensile tests were carried out on pieces of jeans with sizes of approximately 170x17x0.95 mm^3, following the ISO 13934-1 standard [41]. The width and thickness of each sample were exactly measured before testing. The samples were clamped leaving a distance of 100 mm between both grips of the testing machine. The traction force was applied at a velocity of 50 mm/min.

2.7. UV-Visible absorption spectroscopy

UV-Visible absorption spectroscopy is applied to study electronic structures by measuring the light absorbed by a sample at each wavelength. When the sample is irradiated, specific wavelengths are absorbed, leading to the excitation of electrons from the valence band to the conduction band. The minimum energy required for this transition to happen is the bandgap, which corresponds to a sharp increase in the absorbance [42]. In materials where this increase is not as well-defined, the Tauc method [43] can be used to graphically obtain a better estimation of the bandgap by plotting:

$$(\alpha h\nu)^{1/\gamma} = B(h\nu - E_g) \tag{2.3}$$

where α corresponds to the energy-dependent absorption coefficient, h to the Planck constant, ν to the frequency of the photon, E_g to the bandgap energy and B is a proportionality constant. The exponent γ depends on the type of electronic transition and has a value of ½ for allowed direct transitions and of 2 for allowed indirect transitions. The bandgap is then

found by extrapolating the linear part of the curve to the absorption baseline.

UV-Visible absorption spectra can also be used to determine the concentration of a solution. Many molecules absorb ultraviolet or visible radiation at different characteristic wavelengths and the amount of light absorbed is directly proportional to the concentration of the substance as described by the Beer-Lambert law:

$$A = \varepsilon bc \tag{2.4}$$

where A is the absorbance, ε the molar absorptivity of the compound, b the path length of the light through the sample and c the concentration of the substance in the analyte. In this way, when the path length is kept constant across measurements, changes in the intensity of the absorbance peak of a compound at its characteristic wavelength can be directly correlated to changes in concentration.

UV-Visible absorption spectroscopy was used to study the photoprotection capacity of the hybrid fabrics against ultraviolet radiation, calculate their bandgaps and quantify the degradation of rhodamine B during photocatalytic measurements. A further analysis to obtain photoprotection factor standards is detailed in **Chapter 4**. Absorption spectra were measured using a ThermoScientific NanoDrop 2000c spectrometer from 190 to 840 nm with a resolution of 1 nm. The pedestal mode was used for textile characterization, threads were separated into fibers to achieve the minimal translucency needed to measure. The cuvette mode was used for concentration measurements with a light path of 10 mm.

2.8. Photocatalytic activity measurement protocol

The photocatalytic activity of the hybrid fabrics was quantified by evaluating the photodegradation of rhodamine B (RhB) under simulated sunlight conditions. Simulated solar light was generated with a xenon lamp and an AM1.5G optical filter that recreates the standard solar spectrum at the Earth's surface in the wavelengths between 300 and 1100 nm. Samples

of woven fabric of 2x2 cm^2 were immersed into 10 mL of 10^{-5} M RhB aqueous solution in glass vials to avoid wall absorption of the dye. Before any further measurements, a dark test was performed by submerging the samples in RhB and keeping them overnight without illumination. Only samples that showed no degradation in the absence of light were subsequently tested for photocatalytic activity. To initiate the measurement protocol, samples were immersed into the RhB solution and kept in the dark for 2 hours to ensure adsorption–desorption equilibrium. The vials were then exposed to simulated sunlight irradiation at a distance that provided 1000 W/m^2 (1 sun) of surface power. During irradiation, the vials were placed in an ice bath to avoid variations of the concentration due to heating and water evaporation. A solution of RhB without any submerged sample and a solution of RhB with an untreated sample were measured as references each time the protocol was repeated. The degradation of RhB was quantified by measuring its UV–Visible absorption spectrum at regular time intervals for 5 hours.

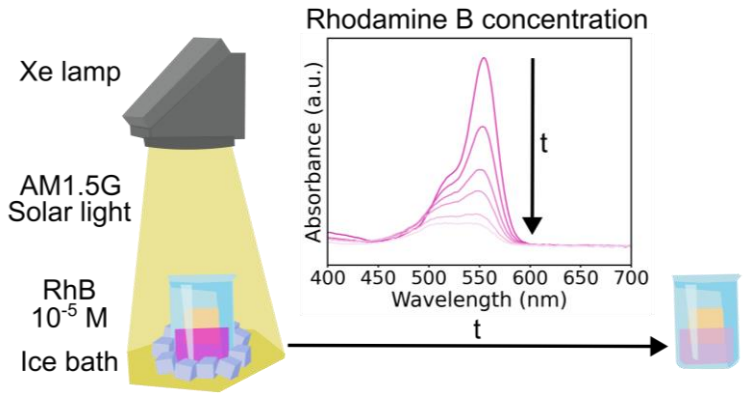

Figure 2.4. Schematic of the photocatalytic activity measurement protocol.

The relative RhB concentration at each time point was calculated applying:

$$\frac{C}{C_0} \propto \frac{A}{A_0} \tag{2.5}$$

where C corresponds to the RhB concentration at each time point, C_0 to the initial concentration, A to the maximum absorbance of RhB at 554 nm at each time point and A_0 to the initial absorbance at 554 nm. This proportionality is explained by **Equation 2.4**. Further data analysis to obtain the photodegradation reaction rate is detailed in **Chapter 4**.

2.9. Contact angle measurements

Contact angle measurements are used to quantify the wettability of a solid surface. Geometrically, the contact angle is defined as the angle formed by a liquid at the three-phase boundary where the liquid, gas (air), and solid (sample) intersect. It serves as an indicator of how well a liquid spreads on a solid surface, surfaces with a contact angle below 90° are classified as hydrophilic whereas those with a contact angle above 90° are considered hydrophobic [44].

Figure 2.5. Schematic of the contact angles of hydrophilic and hydrophobic surfaces.

Contact angle measurements were performed to evaluate the hydrophobicity of the hybrid textiles. Samples were measured using a Krüss G10 contact angle measuring system with a backlit sample stage and controlled movement along the *x*, *y*, and *z* axes. Distilled water droplets (10 µL) were dispensed onto the sample surface and measured using a manual contact angle goniometer.

2.10. Water absorption capacity measurements

The water absorption capacity of the textiles was studied through gravimetric mass absorption measurements according to ISO 62 [45]. The amount of water absorbed by the sample is determined by measuring the mass change of the sample before and after immersion. The water absorption capacity coefficient, w_{AC}, is defined as:

$$w_{AC} = \frac{m_t - m_0}{m_0} \tag{2.6}$$

where m_0 corresponds to the initial dry mass of the sample and m_t to the measured mass at each time interval.

The mass measurements were carried out with a Kern ABT 120-5DM analytical balance with a 0.1 mg resolution. 2x2 cm^2 samples were dried at 60°C overnight. After measuring the dry mass of the samples, they were immersed in 80 mL of distilled water and weighed at different time intervals.

2.11. Antibacterial protocol

The bacteriostatic activity of the hybrid fabrics was evaluated against the bacterial strains *Staphylococcus aureus* (*S. aureus*, ATCC 35556) and *Escherichia coli* (*E. coli*, ATCC 25922), used as model organisms for gram-positive (GRAM+) and gram-negative (GRAM-) bacteria, respectively, and against *Corynebacterium striatum* (*C. striatum*), a bacterium related to body odor.

This protocol was developed as an adaptation of the protocol reported by Liu et. al [35] for the testing of the antimicrobial activity of orthopedic implants. It consists of the following steps:

i. Optical density and bacterial concentration calibration

To establish a relationship between the optical density (OD) and the bacterial concentration in colony forming units per milliliter (CFU/mL) of a bacterial suspension, a bacterial suspension of a certain measured initial OD was plated onto tryptic soy broth (TSB) or lysogeny broth (LB) agar plates for *S. aureus* and *E. coli*, respectively. The bacterial concentration was determined by serially diluting, plating and colony counting following the standard plate count method, choosing the dilution in which the drops had 2-20 CFU. This step was done in triplicate for each bacterial strain and only needs to be done the first time the protocol is applied.

ii. Bacterial culture preparation

A single colony of *S. aureus* or *E. coli* was inoculated into 5 mL of TSB or LB, respectively, and incubated overnight at 37°C. The OD of the bacterial suspension was measured and diluted to a concentration of 5×10^5 CFU/mL using sterile broth.

iii. Sample inoculation

2x2 cm^2 samples were placed in 55 mm Petri dishes and immobilized with labeling tape. A drop of 400 µL of the bacterial suspension was added to the top of each sample and covered with a 4×4 cm^2 piece of Parafilm to evenly cover the sample surface. The samples were incubated overnight at 37°C.

iv. Washing and bacterial recovery

After removing the Parafilm with sterilized tweezers, the samples were washed with 5 mL of sterile phosphate buffered saline (PBS) three times to remove non-attached bacteria. Afterwards, the labeling tape was removed, and the samples were transferred to 50 mL Falcon tubes containing 10 mL of PBS and sonicated for 10 minutes to dislodge the attached bacteria.

v. CFU determination

Serial dilutions of the sonicated PBS bacterial suspension were prepared in a 96-well plate, and 3x10 µL drops of each dilution were plated on TSB or LB agar plates. Plates were incubated overnight at 37°C. CFUs were counted following the standard plate count method, choosing the dilution in which the drops had 2-20 CFU. The final bacterial concentration in the sample, *C*, was calculated using the following formula:

$$C = Average\ CFU\ number\ x\ DF\ x\ AF \tag{2.7}$$

where the *average CFU number* is taken from the 3 drops of the same dilution, *DF* corresponds to the dilution factor and *AF* to the aliquot factor.

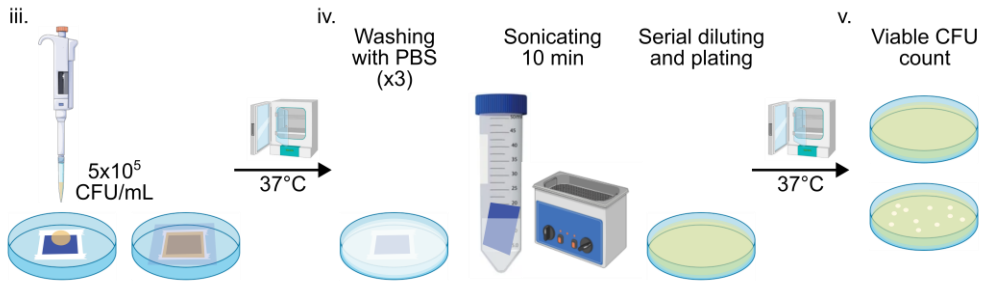

Figure 2.6. Schematic of the antibacterial protocol.

For statistical accuracy, every sample was tested in triplicate and the final CFU value averaged. Samples of the corresponding pristine fabric were tested as positive control each time the protocol was repeated.

2.12. Antifungal protocols

To evaluate the antifungal activity of the textiles, *Aspergillus nidulans* (*A. nidulans*) was taken as model organism for a saprophytic filamentous fungus.

The fungicidal activity of the samples was tested by analyzing their ability to inhibit polar extension of actively growing hyphae. 1×1 cm^2 samples were placed radially and equally spaced from the center of a 15 mL minimal culture medium (MMA) plate. To minimize the influence of sample thickness on fungal growth, 10 mL of liquid MMA was added and allowed to solidify, embedding the samples within the medium rather than leaving them protruding. Asexual spores (conidia) were point inoculated at the center of the plate. After 24 hours of incubation at 37°C, the fungal growth was visually monitored as the hyphae at the periphery of the colony approached the samples.

The fungistatic activity of the samples was tested by analyzing their ability to inhibit spore germination. Conidia were collected from 72 hours-old cultures, washed twice with Tween 20 (0.02%), quantified using a Thoma cell counter and diluted in melted MMA. 1×1 cm^2 samples were placed radially and equally spaced from the center of a 15 mL minimal culture medium (MMA) plate. 10 mL of the MMA spore solution, containing 10^5 conidia, was spread onto the plates and left to solidify. The plates were incubated at 37°C, visually monitoring the germination and growth after 24, 48 and 72 hours until a mycelium is formed.

2.13. Flammability tests

The fire resistance of the hybrid fabrics was evaluated by analyzing their combustion behavior in air. The flammability testing protocol and set up were developed in-house, based on those reported in [46].

2.5×5 cm^2 samples were placed on a metal holder and secured with a magnet, leaving 1 cm of the fabric suspended. One of the suspended corners of the sample was exposed to the flame of a standard lighter until ignition occurred. Fire was allowed to burn either until its extinction or until 4 cm of the sample had burned. The combustion process was recorded on video and timed. Time to ignition, burning duration, char formation, and smoke production were compared visually to those obtained for pristine fabrics.

2.14. Color spectrophotometry

Color spectrophotometry is used to quantify the color of a sample by analyzing its interaction with light. The sample is illuminated with broad-spectrum white light, and the intensity of the light reflected at each wavelength is measured using a spectrophotometer [47]. The resulting spectral data is processed to calculate color values that represent the perceived color of the sample.

Color spectrophotometry was used to study the changes in visual appearance of the samples caused by infiltration. Color measurements were done using a Konica Minolta CM-17d spectrophotometer in reflectance mode with a wavelength range from 400 to 700 nm. The measurement geometry for diffuse and directional illumination was set to 8^o and the aperture size was set to SAV (Small Area View, 3 mm). Both the included (SCI) and excluded (SCE) specular components were measured. 5x5 cm^2 samples were measured in triplicate, taking measurements at 3 different surface points of each sample. Further information on the CIELAB color space and color difference calculations are detailed in **Chapter 5**.

2.15. Fingertip friction and motion capture measurements

Fingertip friction and motion capture measurements were conducted with the participation of volunteer subjects. 6×6 cm^2 samples were mounted on 5×5 cm^2 metallic holders, filled with PDMS of 0-30 on the shore hardness

scale to mimic the stiffness of thigh skin, and secured with metal frames. Participants were presented with sample triplets and asked to sense them with the index fingertip of their dominant hand in a circular motion. During tactile exploration, the applied force, decomposed into its three axial components, was recorded. Simultaneously, finger position and velocity were tracked using an infrared camera system.

Fingertip friction and motion capture measurements, combined with an Odd Sample Out perceptual task, were used to analyze changes in the tactile perception of the fabrics after infiltration. Forces were measured using a ME-Messsysteme K3D120 three-axis force sensor connected to a GSV-8 amplifier. Motion capture was performed with the OptiTrack V120:Trio infrared camera system. Both systems were synchronized using custom LabView programs. Further details on the Odd Sample Out methodology, as well as the analysis of friction and tactile perception data, are provided in **Chapter 5**.

3

Characterization of the organic-inorganic hybrid textiles

This chapter aims to give a complete understanding of the structure and composition of the fabrics before and after treatment with VPI.

The composition and distribution of the threads that are woven to form the cotton and jeans fabrics are explained. Then, the surface and internal changes, introduced by the infiltration of the threads, are studied by electron microscopy and compared to those introduced by coating with Atomic Layer Deposition (ALD).

The chemical composition of the obtained organic-inorganic hybrid fibers is analyzed by Energy Dispersive X-Ray spectroscopy (EDX) and Optical Emission spectroscopy (ICP-OES), and their structural order is investigated by X-Ray Diffraction (XRD).

Finally, the mechanical properties are investigated through tensile testing of the infiltrated fabrics.

3.1. Conformation of the fabrics

The textiles used in this study were woven, that is, fabricated by the interlacing of two sets of threads, called warp and weft. Each of the individual threads was formed by spinning of tens of individual fibers. In the raw cotton fabric, all of these fibers were natural cotton. These fibers were spun together and could not be separated. The commercial jeans had

a composition of 50% cotton, 44% polyethylene, 5% elastomultiester and 1% elastane, according to the description provided by the supplier. This fabric has been dyed and treated by the manufacturer before the infiltration with VPI. We did not receive any information about chemicals and techniques used during this treatment by the manufacturer. The threads could be separated into individual fibers, of which fibers on the outer textile surface were dyed in the typical blue jeans color while inner fibers of the textile were white.

Before any treatment, we first characterized the two types of fibers found in the jeans threads to understand how cotton and polyethylene are distributed in them. This distinction is important, since differences in structure and chemistry of the polymers can affect their response to infiltration, ultimately changing the characteristics and properties of the resulting hybrid material.

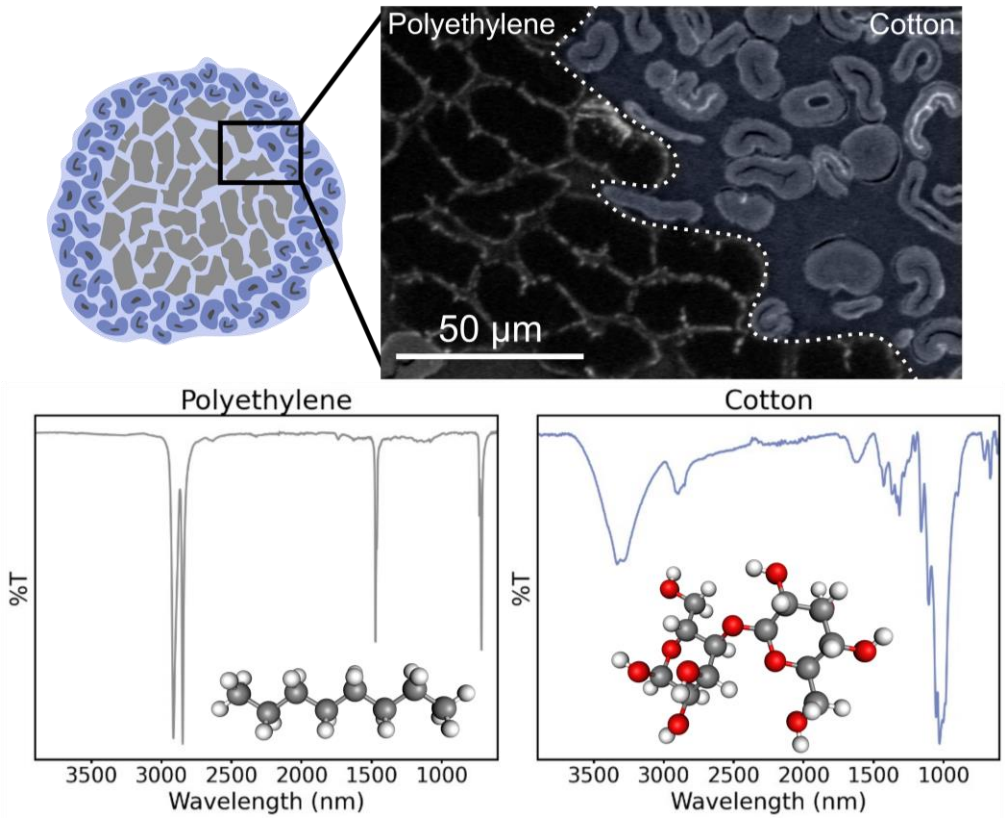

Figure 3.1. Schematics of the sample appearance, backscattered electrons image and infrared spectra of the two main types of fibers, polyethylene (grey), and cotton (blue), forming the threads in jeans.

To do so, we analyzed cross-sectional images of the threads in the SEM using a vCD detector. The backscattered electrons show an image with material dependent contrast, as shown in **Figure 3.1**. Each of the threads is formed by a core of multiple polyethylene fibers (grey), surrounded by a shell of cotton fibers (blue). The polyethylene fibers appear darker, more compact and with an angular shape. Cotton fibers appear lighter and have a more organic shape, with a characteristic hollow nucleus known as the lumen [48]. This distinction was confirmed by measuring FTIR spectra of the individual fibers. Characteristic resonance bands found for each of them coincide with the expected chemical structure of the polymers [49], [50].

3.2. Proof of infiltration

3.2.1. Infiltration process

The chosen fabrics are treated by VPI to produce organic-inorganic hybrids, in which the polymers act as the organic matrix and are infiltrated with zinc oxide or titanium dioxide. Both types of fabrics were infiltrated with ZnO or TiO_2 following the standardized conditions in this thesis. Samples were processed interchangeably in a Savannah reactor from Cambridge Nanotech and a PLAY reactor from CTECHnano. Typically, the samples are suspended in the chamber in a way that allows both sides of the fabric to be in contact with the precursors. DEZ was used as the zinc source and $TiCl_4$ as the titanium source. In both cases purified water (H_2O) was used as the counter precursor. All precursors were kept at room temperature. The processing temperature was set to 60°C for ZnO and 100°C for TiO_2 infiltration. As explained in the previous chapter, the process temperatures were chosen to minimize damage to the fibers and to avoid drastic changes in their appearance. N_2 was used as carrier gas with a constant flow of 20 sccm. Each VPI half-cycle consisted of 40 ms of precursor dosing, 40 s of exposure and 60 s of purge. Three pieces of fabric of 5x5 cm^2 each were treated in the same process.

3.2.2. Morphology of the hybrid fabrics

To analyze the changes introduced into the fabrics by the infiltration process, we first take a look at the morphology of the individual threads and fibers under the electron microscope. Even though our process primarily infiltrates the metal oxides, in most cases a concerted coating of the surface of the substrate with a thin layer of the inorganic material is unavoidable. In the chosen textiles, the outermost fibers are composed of cotton. The cellulosic molecular structure contains high concentrations of hydroxyl groups which are highly reactive towards the used precursors [27]. Therefore, the ALD growth on the surface will occur and provoke changes in the surface topography of the outer fibers of the threads, which can be used to confirm the success of the process. To investigate them, we extract random threads from the treated pieces of fabric and image them, as shown in **Figure 3.2** for ZnO and in **Figure 3.3** for TiO_2 infiltration.

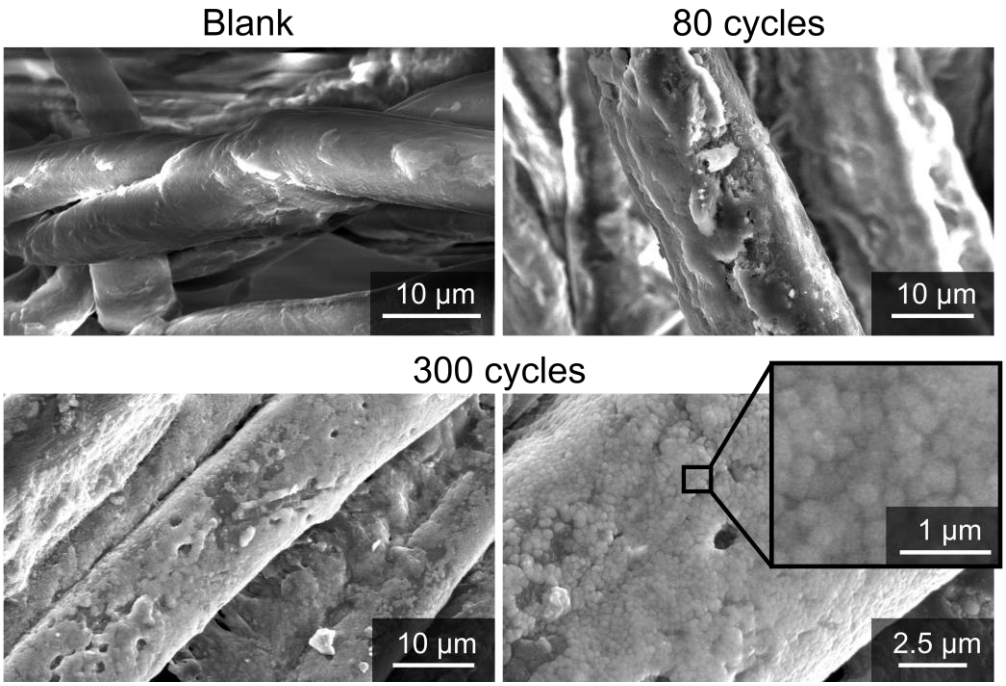

Figure 3.2. SEM images of the surface of jeans fibers before and after 80 and 300 cycles of ZnO infiltration.

The surface of the fibers before treatment (labeled as 'blank') is smooth and presents few features, apart from some deeper trenches due to the natural bending of the fibers or to the union of two separate fibers. After

the treatment with both ZnO and TiO_2, the surface roughness increases. This change is already appreciable after 80 cycles of treatment. The fibers look thicker and less uniform, with bulges appearing on the surface, and the trenches are progressively filled with the coating material. After 300 ZnO infiltration cycles, we can see a granular structure of small circular domains (zoomed area in **Figure 3.2**), characteristic of crystalline materials, completely covering the surface of the fibers.

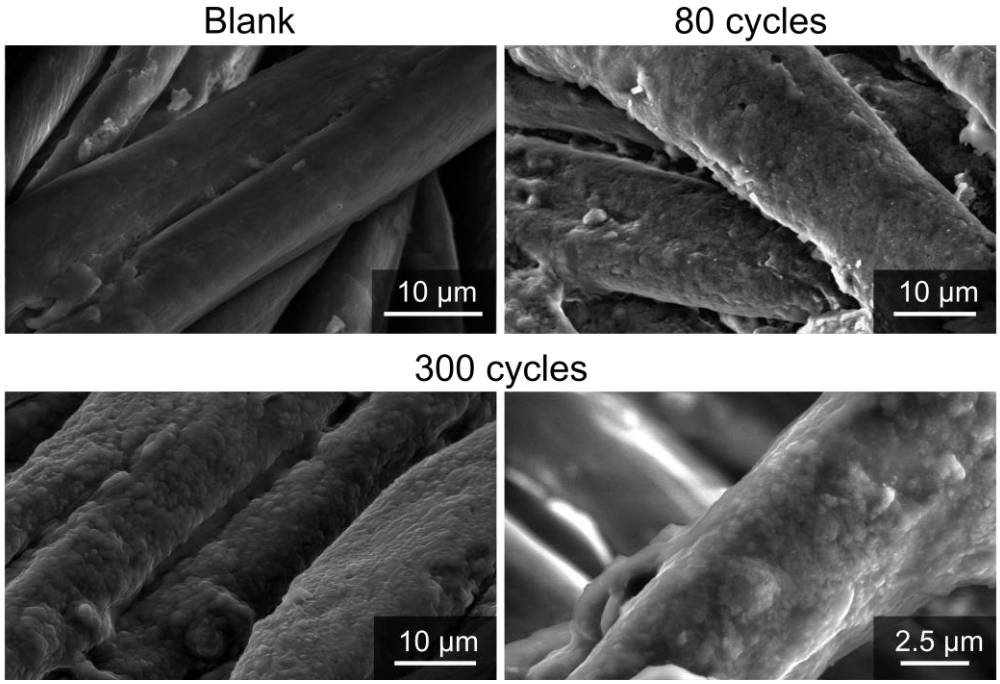

Figure 3.3. SEM images of the surface of jeans fibers before and after 80 and 300 cycles of TiO_2 infiltration.

In the case of TiO_2, the coating does not have a distinct periodicity characteristic of crystalline order. The effectiveness of the treatment can also be appreciated during the imaging of the fibers with SEM through noticeable changes in brightness and contrast, especially after ZnO infiltration. As the fibers become more conductive, due to the addition of the metal oxides, they charge less under the electron beam, making their imaging easier.

Once we knew that the oxides are growing on the fibers, we moved on to confirm infiltration by studying the cross-section of the threads. In order to identify and distinguish the infiltrated zones, we combined imaging with

backscattered electrons and EDX mapping. Here, we focus on treatment with ZnO rather than TiO_2, since the characteristic $L\alpha$ energy of Zn (1.012 keV) [51] is easier to distinguish from the other elements present in the polymers than the $L\alpha$ energy of Ti (0.452 keV), and also lower than the $K\alpha$ energy of Ti (4.510 keV). Emission lines with higher energies need higher accelerating voltages to be correctly detected, which accentuates the charging and damaging of the samples, leading to a lower quality of the images and maps obtained. The resulting images for the cotton fabric infiltrated with 300 cycles of ZnO are shown in **Figure 3.4.**

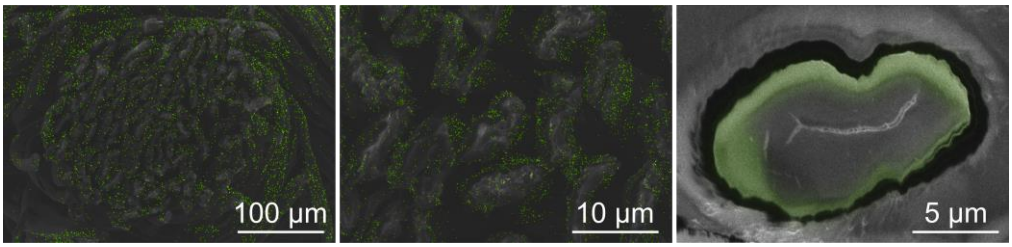

Figure 3.4. SEM images and EDX maps of Zn atoms (green) in the cross-section of a cotton thread after 300 ZnO infiltration cycles.

The left and middle images show the cross-section of a thread obtained after cutting the woven fabric with a scalpel. No further treatment was done to the exposed surface. From the EDX map on the left-hand side (Zn colored green), we can confirm that there is Zn distributed all over the inside of the thread. In the middle image, we magnified the inner section of the fibers of the thread. In this map, Zn is found dominantly covering the individual fibers, suggesting that each individual fiber is at least coated.

To verify whether the fibers are infiltrated or just coated, the thread was encapsulated in resin and cut with a microtome to reduce the damage caused to the fibers when preparing a cross-section. In this case, the surface of the cross-section was polished prior to imaging. The addition of the resin, combined with the high magnification needed to analyze a single fiber, deteriorates the resolution and accuracy of the EDX maps. To get around this, we used imaging with backscattered electrons for a better chemical resolution instead. In the image to the right, the cross-section of an individual cotton fiber is shown. The green coloring marks the inorganic-organic gradient below the surface of the fiber, formed after

infiltration with ZnO. This confirms that each of the fibers of a thread is infiltrated with the metal oxide.

These images prove that the fabrics are infiltrated in two ways. First, each of the woven threads is fully infiltrated since the metal oxide is found even in the most central fibers. Secondly, each of the fibers forming the thread is infiltrated, creating a gradient of metal oxide from the surface into the polymer bulk. Therefore, we achieved the growth of the inorganic materials both inside of the threads and inside of the fibers that constitute them upon treating a macroscopic piece of woven fabric.

3.2.2.1. Comparison with ALD

After having proven successful infiltration of the fabrics, we compared the mechanical properties with those of ALD-coated fabrics. For the preparation of the coated samples, all process parameters described in **Section 3.2.1** were maintained except for the exposure time, which was eliminated. Thus, each half cycle consisted of 40 ms of precursor dosing and 60 s of purging. With this change, the precursor molecules do not have sufficient time to diffuse and penetrate into the threads and fibers of the fabric, and the reactions only happen on the outer surface, coating the samples.

This difference between ALD and VPI becomes greatly important when the organic substrate has a high flexibility, as is the case of textile fibers. The inorganic material is ceramic, adding brittleness to the substrate. Manipulation of the fabrics can cause cracking or even complete detachment of the metal oxide coating, as shown in **Figure 3.5.** Image a. was taken using a vCD detector and backscattered electrons. The metal oxide coating appears brighter than the exposed fiber surface. Images b., c. and d. were taken with a regular ETD detector, sensing secondary electrons. Here, the exposed fibers appear brighter than the coating as they become charged under the electron beam. During an ALD process, a rigid layer of the inorganic material is formed on the surface, creating an abrupt interface between the polymer and the metal oxide. As a consequence, once a crack forms, it can propagate quickly, causing delamination. This damage can be significantly reduced by using VPI. Here, a density gradient forms below the surface gradually blending the inorganic and organic materials. This makes cracks less likely to appear and propagate, since it

minimizes the difference in strain and retains the flexibility of the fibers [27].

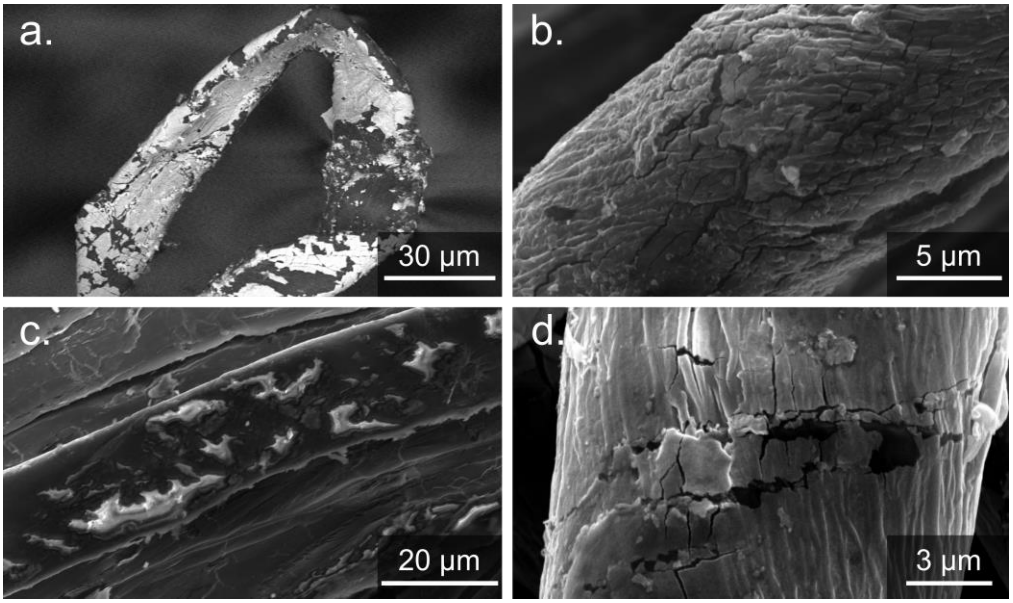

Figure 3.5. SEM images showing cracking and detachment of the coating of cotton (a. and b.) and jeans (c. and d.) fibers after coating with 300 ZnO ALD cycles.

3.2.3. Chemical composition of the hybrid fibers

So far, we have confirmed the successful infiltration of the fibers, creating organic-inorganic hybrids of polymers and metal oxides. Here, we further characterized them with focus on their chemical composition, estimating the amount of metal incorporated into each type of fabric by VPI.

Initially, the analysis was done with energy dispersive X-ray spectroscopy (EDX). Although this technique is not sufficiently precise for a quantitative analysis, it allows us to confirm the presence of metal atoms inside the fibers, estimate their quantity and compare with other materials. All the spectra were taken with an accelerating voltage of 10 keV of the e^--beam, the lowest possible that still can detect the *Kα* energy of Ti. To reduce the error, the mean value of 10 measurements of different fibers and its deviation error are taken. The results obtained after 80 and 300 infiltration cycles of ZnO and TiO_2 are shown in **Figure 3.6**.

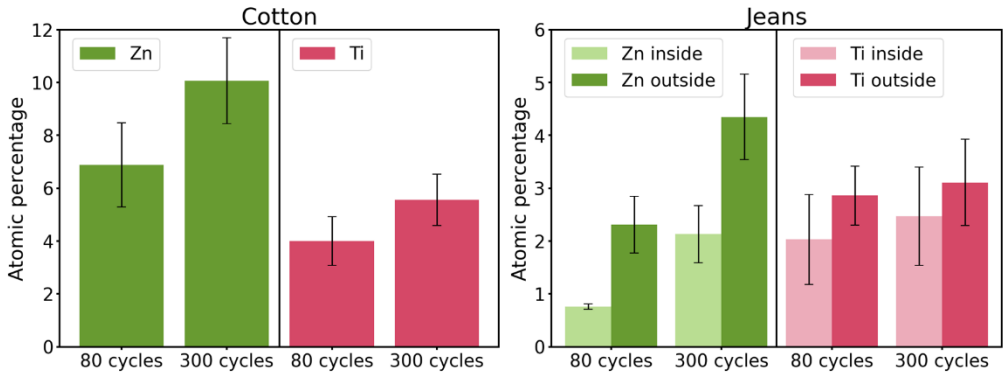

Figure 3.6. EDX analysis, taken at 10 keV, of the atomic percentage of Zn and Ti found in cotton and jeans fibers after 80 and 300 infiltration cycles of ZnO and TiO_2.

Before measuring, the jeans threads were taken apart, separating the polyethylene fibers from the cotton fibers. The analysis of the metal content in each of them was carried out independently. The results are labeled 'inside' for the fibers of polyethylene and 'outside' for the cotton ones, according to their placement in the threads.

Natural cotton fibers have a higher atomic percentage of both Zn and Ti, about two times more than the cotton fibers in jeans after each VPI treatment. This implies that the processing of the cotton fibers in jeans, which is unknown but surely includes chemical modifications like bleaching and dying, reduces the reactivity towards the used precursors or the density of the reactive groups found in the polymer. Therefore, raw natural fibers are more responsive to infiltration treatment and can uptake more ZnO and TiO_2. In both fabrics, the atomic percentage of Zn for a given number of cycles is higher than that of Ti. This is not surprising since the growth rate of the ALD of ZnO from DEZ and water is higher than that of TiO_2 from $TiCl_4$ and water.

The presence of metal atoms in the inner polyethylene fibers, forming the threads in jeans, further confirms the full infiltration, achieved even when treating larger pieces of the fabrics. The amount of Ti found in the inner polyethylene fibers of the threads (inside) was higher, closer to the amount found in the outer cotton fibers (outside), than the amount of Zn atoms. This could be due to a faster growth of ZnO on the surface, blocking the in-diffusion of DEZ into the threads after a lower number of cycles than TiO_2. Another possibility could be the polyethylene fibers being more reactive

towards $TiCl_4$ than DEZ, increasing the amount of TiO_2 that can be grown in the inside of the thread.

Lastly, we observed that the increase in the percentage of metal atoms is not linearly correlated to the number of cycles. In the case of cotton, the atomic percentage of Zn increases from 7% to 10% when increasing the number of cycles from 80 to 300; in the case of Ti, it increases from 4% to 5.5% for the same cycle increment. If the atomic percentages increased linearly the final percentages should be 25 and 15% for Zn and Ti, respectively. The same tendency is observed in the case of jeans. The atomic percentage of Zn rises from 2.3 to 4.4%, but not to 8.7%, and that of Ti rises from 2.8 to 3.1%, instead of 10.7%. This clearly shows the loss of self-limitation when using VPI instead of ALD. Additionally, as mentioned, the coating of the surface of the polymer can eventually prevent the diffusion of the precursor molecules into the polymer. In this way, the inorganic material can no longer be infiltrated and the deposition changes into an ALD regime, growing only as a coating with a thickness proportional to the number of cycles. When looking at the optimization of the process and its applications, this suggests that an increase in the number of cycles will not necessarily ensure significantly better functionalities.

To obtain a more reliable quantification of the metal oxides in the hybrid textiles, we analyzed the fabrics by inductively coupled plasma–optical emission spectroscopy (ICP-OES). Circular pieces of 1 cm in diameter were cut from the 5x5 cm^2 treated fabrics and dissolved in H_2SO_4 at 260°C in a chemical digestion equipment. A Conikal concentric nebulizer was used, the pressure was set to 2.40 bar and the flow to 1.82 L/min. The characteristic emission lines are 213.856 nm for Zn and 334.991 nm for Ti [52]. The obtained weight percentages are shown in **Figure 3.7**.

With this technique, we focused on the weight percentage of the metal in the sample rather than the atomic percentage. Since Zn is approximately 1.37 times heavier than Ti, the differences in quantity become more evident when talking about weight. Again, we confirmed that the deposition rate of Zn is higher than that of Ti and, for the same number of cycles, there will be a higher amount of ZnO than of TiO_2 in the resulting hybrid fabrics.

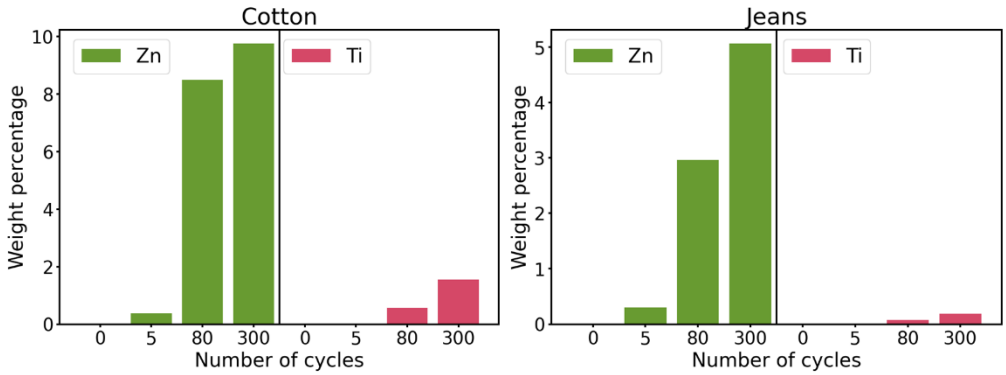

Figure 3.7. ICP-OES analysis of the weight percentage of Zn and Ti found in cotton and jeans fabrics before and after 5, 80 and 300 infiltration cycles.

ICP-OES provides reliable quantification and much higher precision at lower concentrations than EDX. The bars for the weight percentages of Zn and Ti in the untreated fibers were added since they are very low, but not zero. These atoms probably come from cross-contamination during the manufacturing and packaging of the samples or from traces of the metals in water. In the case of infiltration with Ti, the increase during the first 5 cycles is about 30% for both fabrics. Infiltration with 5 cycles of Zn, however, increases the weight percentage of Zn in the samples by 100% already. The weight percentages of the sample treated with 5 cycles are also measured to further analyze the loss of linearity of the growth per cycle of VPI and its saturation. This behavior is different when infiltrating cotton and jeans. In cotton, the uptake of both metal oxides per cycle is the highest at 80 cycles. In jeans, the uptake is highest during the first 5 cycles and is periodically decreased with increasing number of cycles. This gives an idea of how the fabrics saturate differently during the infiltration process. In cotton, the infiltration continues until at least 80 cycles, resulting in hybrid fibers with a higher amount of metal oxide. In jeans, the infiltration starts to become hindered earlier in the process, either due to a lower reactivity or a higher resistance to diffusion, resulting in hybrid fibers with at most half the amount of metal oxides as in cotton.

3.2.4. Structural order in the hybrid fibers

In this section, we focus on the structural order of each of the materials inside the hybrid organic-inorganic textiles. In **Section 2.2**, the SEM images of the surface coatings already hint at crystalline order in ZnO, whereas TiO_2 seems to be amorphous. This corresponds well with the literature, describing ZnO growing crystalline at temperatures as low as 40°C [53], while TiO_2 does not show any crystallinity below 190°C [54]. To further confirm these results, we analyzed the infiltrated textiles by XRD. For that, a piece of approximately 2x2 cm^2 is repeatedly cut until powdered using a guillotine. The obtained powder is compressed into a pellet and measured in gonio mode. The XRD measurements were carried out with a $Cu\ K\alpha$ (λ=0,154 nm) radiation source with a working voltage and current of 45 kV and 40 mA, respectively.

The diffraction patterns obtained from cotton fabrics before and after different cycles of ZnO infiltration are shown in **Figure 3.8**. ICDD diffraction patterns for wurtzite ZnO (04-008-8199) [55] and I_β-cellulose (00-056-1718) [56] are shown as reference. The original raw cotton fabric has three main peaks at 2θ of 14.93, 16.64 and 22.98°, which match those associated with the parallel chains of I_β-cellulose. This phase of cellulose is characteristic of plants, like cotton or flax, and typically contains a mixture of crystalline and amorphous regions. These peaks can slightly shift with ambient moisture absorption. Since the infiltration process involves the heating of the fabrics and can cause changes in the water content through desorption, the untreated samples are heated at the same temperature for the same duration as the process, but without any precursors, to ensure a correct comparison. The cellulose peaks do not shift after infiltration, indicating that the infiltration does not modify the order of the polymer chains.

As the number of ZnO infiltration cycles increases, the characteristic peaks of ZnO in its wurtzite phase become clearer and more intense. At 20 cycles we expect a very small amount of ZnO in the hybrid textile relative to the substrate and its signal is likely covered by that of cellulose. The triplet of ZnO peaks around 35° coincides with a feature in the untreated cellulose making it difficult to detect, only the peak at 32.28° can be clearly distinguished. At 80 cycles, the peaks at 57.19, 63.31 and 65.46°, as well as

the broader peak around 48°, become visible. Finally, at 300 cycles the whole ZnO diffraction pattern can be seen, along with that of cellulose.

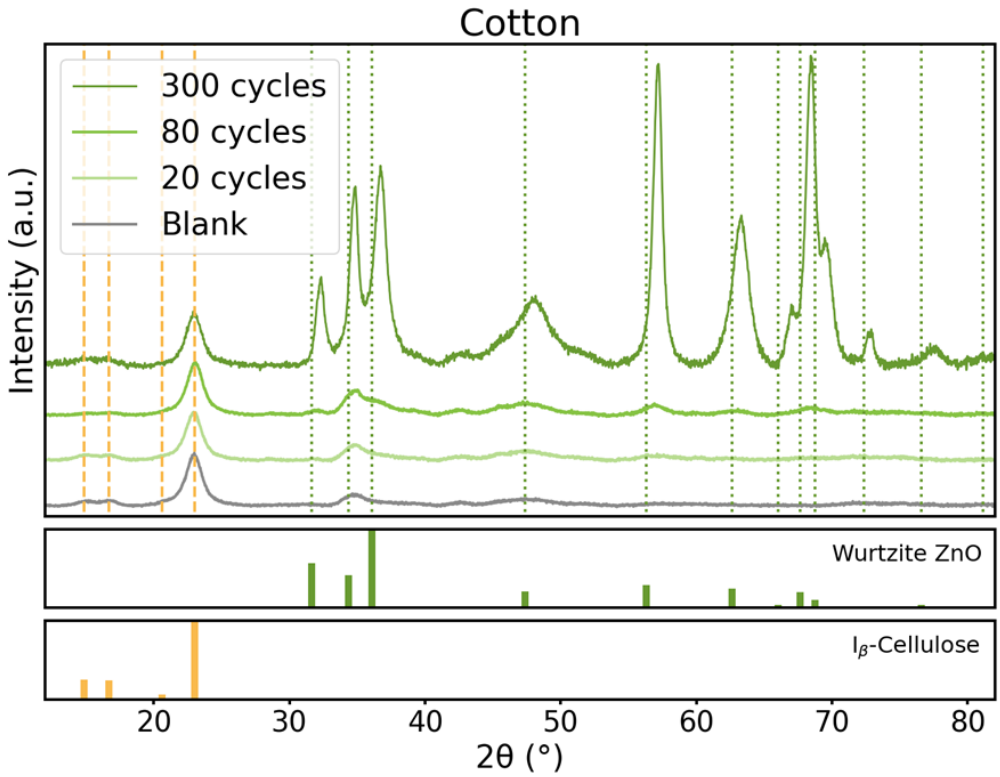

Figure 3.8. XRD patterns of cotton fabrics before and after different ZnO infiltration cycles and reference ICDD patterns for wurtzite ZnO and I_β-cellulose.

The diffraction patterns obtained for jeans fabrics before and after varying cycles of ZnO infiltration are shown in **Figure 3.9**. The ICDD diffraction pattern for β-polyethylene (00-011-0834) is also shown. The untreated fabrics consist of cotton and polyethylene. The characteristic peaks of cellulose appear in the diffraction pattern along with new peaks at 19.64, 21.78 and 24.23°. These peaks, although slightly displaced, match most closely the peaks in β-polyethylene, a crystalline phase of polyethylene, formed in high stress and shear conditions like upon drawing fibers.

Again, the peaks corresponding to the polymer structure are not changing with the infiltration process. In the case of jeans, 80 cycles of ZnO infiltration are necessary to resolve the ZnO peak at 31.54°. Since the untreated fabric has less features at higher angles, the peaks at 56.50, 62.80 and 67.80° are also distinguishable. At 300 cycles, these peaks

become clearer, and at 600 cycles, the whole ZnO diffraction pattern can be appreciated with sharper and well-defined peaks. In the case of cotton, 300 cycles were enough to resolve the ZnO peaks, again showing that raw cotton is more responsive to the infiltration treatment, and the resulting hybrid textiles have a higher percentage of inorganic materials than those of jeans.

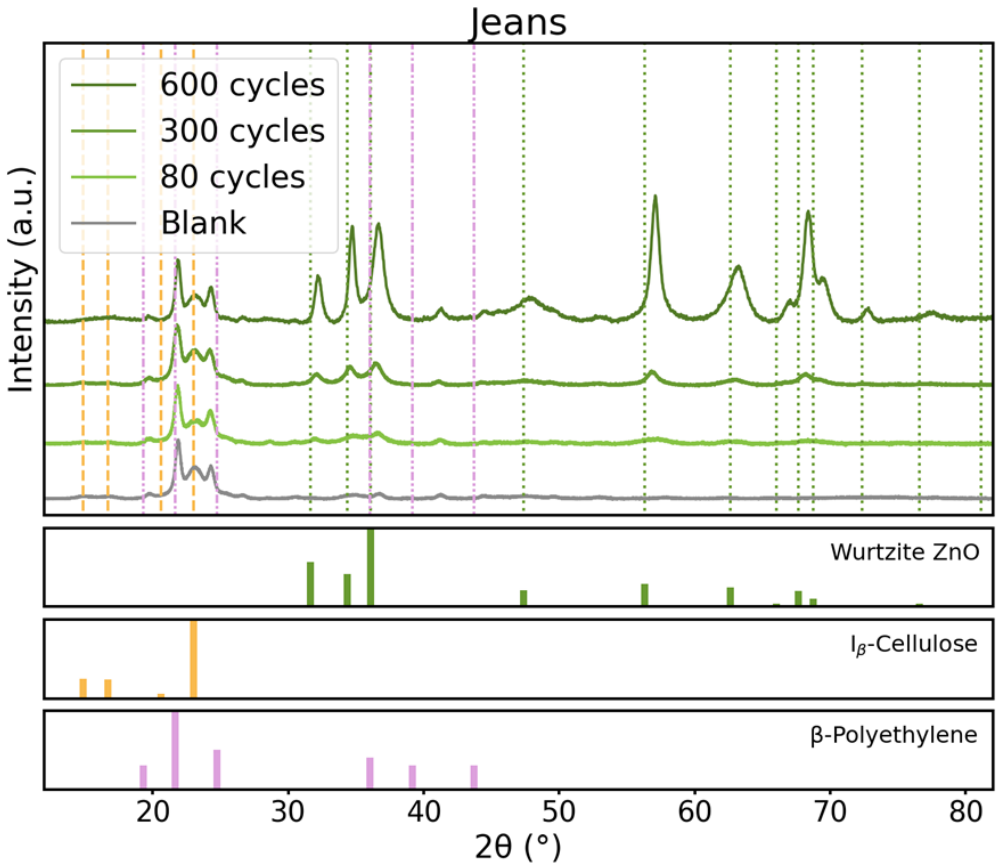

Figure 3.9. XRD patterns of jeans fabrics before and after different ZnO infiltration cycles and reference ICDD patterns for wurtzite ZnO, I_{β}-cellulose and β-polyethylene.

In both diffraction patterns, those of cotton and jeans, there is a significant shift of the ZnO peaks towards higher angles with respect to the reference pattern, which indicates a reduction of the unit cell parameters of the infiltrated ZnO. The main ZnO unit cell parameters calculated from the XRD patterns are shown in **Table 3.1**.

		[100] 2θ (°)	[200] 2θ (°)	a (Å)	c (Å)	V (Å³)
Reference	Wurtzite ZnO	31.619	34.335	3.265	5.219	48.18
Cotton	300 cycles	32.276	34.794	3.200	5.153	45.70
Jeans	600 cycles	32.147	34.628	3.213	5.177	46.27

Table 3.1. Unit cell parameters of reference ZnO and ZnO grown in cotton and jeans.

In both fabrics, all unit cell parameters of the infiltrated ZnO are compressed in comparison to those of self-standing ZnO. In cotton, *a* is reduced to 98% of the reference value while *c* is reduced to 98.7%, making the total volume of the cell 94.8% of the reference value. In jeans, the reduction is slightly smaller, 98.4% for *a*, 99.2% for *c* and 96% for the total volume. Therefore, the infiltrated ZnO has gone through a severe compressive strain, likely induced by defects, which can affect its electric and mechanical properties. Similar characteristics have been reported in ALD-grown ZnO on polysulfone (PSU) electrospun fibers and are attributed to interstitial Zn atoms [57].

The mean crystallite size of the infiltrated ZnO was estimated from the XRD patterns using the Debye-Scherrer formula (**Equation 2.2**). The structure of the grown oxide is composed of nano crystallites of 12.8±1.8 nm in cotton and of 11.5±1.5 nm in jeans.

The diffraction patterns obtained for TiO_2 infiltration in both cotton and jeans only show the peaks corresponding to the polymers, confirming that the TiO_2 in the hybrid textiles is amorphous.

3.2.5. Mechanical properties of the hybrid textiles

After confirming the infiltration of crystalline ZnO into the textile polymers, it is necessary to ensure that this treatment does not worsen the mechanical properties of the resulting hybrid textiles. In order to analyze this, uniaxial tensile tests were carried out on pieces of jeans with sizes of 17x1.7 cm^2 and a thickness of 0.95 mm, approximately, following the ISO 13934-1 standard [58]. Each end of the samples was clamped to the testing tool, which applies a traction force at a velocity of 50 mm/min. The results obtained for jeans before and after 80 and 300 cycles of ZnO infiltration are

shown in **Figure 3.10**. Five replicas of each treatment condition are tested for result reliability.

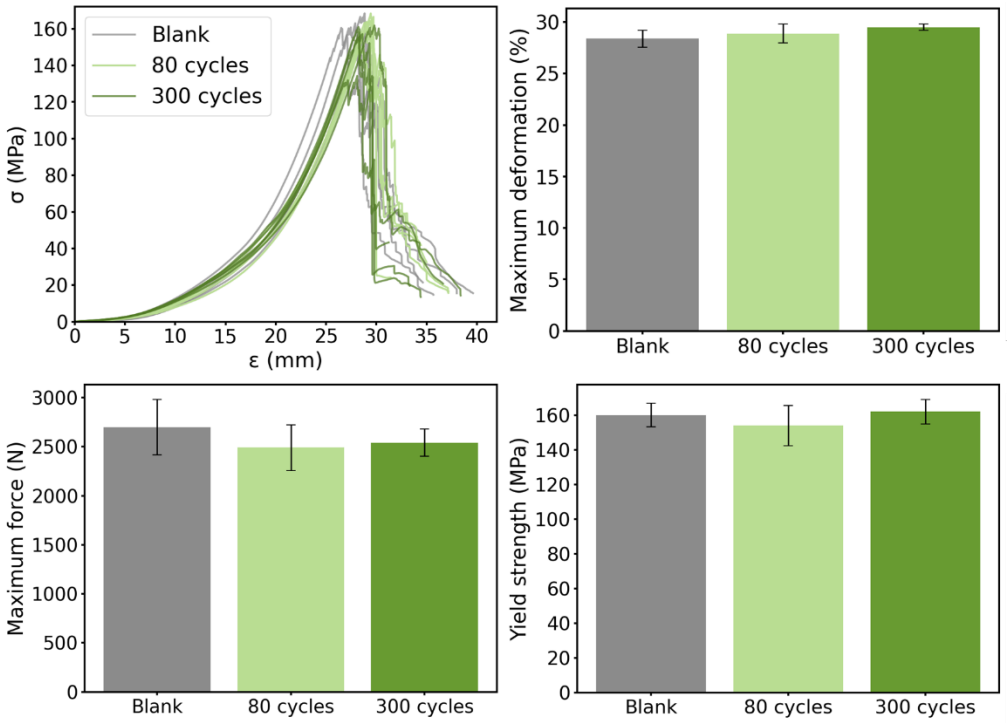

Figure 3.10. Engineering stress-strain curves, deformation and force at breakage and yield strength of jeans fabric before and after 80 and 300 ZnO infiltration cycles.

The engineering strain-stress curves of the textiles before and after infiltration with 80 and 300 cycles of ZnO are very similar. There is no appreciable difference between processing conditions. Moreover, the dispersion between the replicas of a given condition overwhelms the differences between processing conditions. From these curves, some key parameters describing the resistance of the textiles can be extracted. The maximum deformation before breakage is slightly increased with infiltration, rising from 28.6 to 29.5%. The maximum force resisted by the textiles decreased from 2700 to around 2500 N after treatment. The yield strength of the fabrics was maintained, oscillating between 160 and 155 MPa. The variations in these parameters are minimal and, considering the measuring errors, can be neglected. Therefore, we can consider that the resistance of the textiles to uniaxial tension is generally preserved after the infiltration of crystalline ZnO, making the hybrid textiles as apt as the

untreated ones for applications where fabrics are required to withstand a deformation by an applied load.

3.3. Conclusions

We have thoroughly characterized cotton and jeans fabrics before and after different treatments by VPI of ZnO and TiO_2, attending to their morphology, chemical composition, and structural order.

Before any treatment, the conformation of the woven fabrics was investigated to identify the composition of the polymers that form each thread and their distribution, allowing for a better understanding of their response to the infiltration.

After each of the fabrics was infiltrated with a standardized VPI process, the surface and cross-section of the individual threads were analyzed using SEM. The changes in the surface roughness confirmed the homogeneity of the treatment and hint at the structural order of each of the oxides. Imaging and chemically resolved mapping of the cross-section confirms that each of the individual fibers forming the threads were infiltrated. The VPI process is therefore infiltrating the threads in two senses, simultaneously achieving the growth of the metal oxides inside of the threads and below the surface of the fibers that constitute them, all while treating a macroscopic piece of woven fabric.

Additionally, we compared the damage found in the hybrid fibers obtained by VPI with the ones found in fibers coated by regular ALD. The metal oxides grown by VPI are less prone to cracking and peeling with stretching and bending of the textiles due to a gradually changing hybrid interface layer between the polymer bulk and the brittle inorganic coating.

The chemical composition was analyzed by EDX and ICP-OES to confirm the presence of Zn and Ti atoms in the obtained organic-inorganic hybrid fibers. Quantification confirmed that the amount of infiltrated ZnO is higher than that of TiO_2, following the tendency of the known ALD growth rates for each of the processes. Raw cotton allowed more infiltration of the metal oxide than treated commercial jeans, which became saturated faster.

The presence of metal atoms in the inner fibers of the threads further confirms that full infiltration was achieved.

The structural order was investigated by XRD. As expected from the chosen deposition temperatures, the infiltrated TiO_2 grows amorphously, while ZnO grows in its wurtzite crystalline phase. In cotton, the characteristic peaks of I_β-cellulose appeared, while in jeans they appeared in combination with the β-polyethylene ones. These peaks did not shift with infiltration, proving that the structural order of the polymeric chains was not affected by the infiltration. The intensity of the characteristic peaks of ZnO increased with the number of infiltration cycles and reaffirmed that the amount of metal oxide in cotton is higher than in commercial jeans. In both fabrics, a shift in the position of the ZnO peaks indicated that the unit cell of the infiltrated metal oxide is compressed.

Finally, the preservation of the mechanical properties of jeans pieces of fabric infiltrated with ZnO was confirmed through tensile testing of the infiltrated fabrics.

4

Achieved functionalities of the organic-inorganic hybrid textiles

After the characterization of the structure and composition of the cotton-based fabrics infiltrated with metal oxides using VPI, this chapter focuses on the evaluation of their induced functionalities. The goal is to obtain as many as possible properties of relevance for the textile industry with a single VPI process.

The photoprotective function of the hybrid textiles against ultraviolet radiation (UVR) was tested by measuring their UV-Visible absorption spectra and extracting their bandgaps. Ultraviolet Protection Factors (UPF) and UVB and UVA blocking percentages were computed as standardized quantification of the effectiveness in blocking erythema-inducing UVR.

For the analysis of their self-cleaning activity, the photodegradation of organic dyes under simulated solar light was studied as well as the durability of the photocatalytic activity. The changes in contact angle and water absorption capacity of the fabrics induced by the infiltration were quantified.

The antimicrobial properties of the textiles were proven both against bacteria and fungi. The bacteriostatic activity of the hybrid fabrics, prepared with varying number of cycles, was tested against *Staphylococcus aureus* and *Escherichia coli*, model strains of GRAM+ and GRAM- bacteria, respectively. Additional tests against *Corynebacterium striatum* were carried out to assess the elimination of body odors. The antifungal activity

was analyzed by observing the inhibition capability of the textiles against polar extension of actively growing hyphae and spore germination of the model filamentous fungus *Aspergillus nidulans.*

The improvement in fire resistance of the hybrid fabrics was evaluated by visually analyzing their combustion behavior in open air, focusing on parameters such as time to ignition, burning duration, char formation, and smoke production.

Finally, the durability of the obtained UV-blocking and antibacterial properties to conventional washing of the fabrics with water and soap was proved.

4.1. UV protection

Exposure to ultraviolet radiation (UVR) remains the most important risk factor for the development of skin cancer, it can also cause erythema, photoaging and pigment darkening of spots on the skin. It is not possible to completely avoid UVR, making protective methods like sunscreen and protective clothing key in the prevention of such pathologies. Some recent studies have shown that photoprotective fabrics are more effective in absorbing UVR than sunscreen, and their reliability does not depend on correct application. Both ZnO and TiO_2 are widely used as inorganic components in sunscreens, absorbing radiation within the UVB (280-315 nm) and UVA (315-400 nm) wavelengths and reflecting the longer UVA and visible wavelengths. Here, we analyze the UV-blocking efficacy of the organic-inorganic fabrics studied.

4.1.1. UV-Visible absorption spectra and bandgaps

We analyzed the absorption spectra of treated textiles in the UV-Visible range. To measure the absorption, the samples need to be relatively translucent and allow some light to pass through. Therefore, we cannot measure whole pieces of fabric but have to focus on individual threads instead. Still, an individual thread does not allow enough signal to pass to the detector, and no absorption signal can be recorded. In the case of

cotton, these threads cannot be taken apart into individual fibers without them breaking, thus it is not possible to measure their absorption spectra. In the case of jeans, each individual thread can be untightened and fanned out, separating the individual fibers in a way that allows light to pass through them. For this reason, the following discussion in this section refers to the jeans fabrics but, considering the metal oxide quantification discussed in **Chapter 3** and the photocatalysis studies in **Section 4.2.1**, similar results can be expected for raw cotton. The UV-Visible absorption spectra measured for jeans fibers before and after infiltration with ZnO and TiO_2 are shown in **Figure 4.1**.

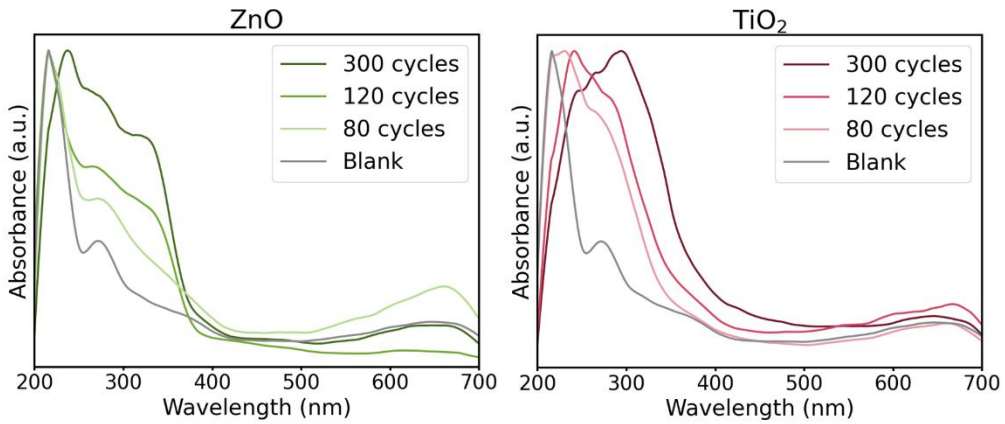

Figure 4.1. UV-Visible absorption spectra of jeans fibers before and after infiltration of ZnO and TiO_2 applying different cycle numbers.

The untreated fibers only show a significant absorption in the UVB region, with a full absorption peak at 215 nm and a smaller one at 270 nm. For both metal oxides, an extension of the absorption into the UVA wavelengths is observed after the infiltration. In the case of ZnO, the total absorption between 200 and 360 nm progressively increases with the number of cycles while the absorption wavelengths do not shift. In the case of TiO_2, however, the absorption curve progressively advances into the UVA and near-visible regions when the number of cycles is increased. From these spectra, we can see that the UV-blocking capacity of the fibers has been improved. The reported values for the bandgaps of cellulose and polyethylene range from 5 to 5.6 eV [59] and from 8 to 9 eV [60], respectively. This implies that they can only absorb radiation in the UVC (100–280 nm) region of the solar spectrum, which is completely

attenuated by the ozone present in the atmosphere before reaching the Earth's surface. These values are in good agreement with our measurements of the untreated jeans fibers. In order to get quantitative information about the changes in the bandgaps of the hybrid fibers prepared, we apply the Tauc method [61] to the absorption curves and calculate their bandgap. The results obtained are shown in **Figure 4.2** for ZnO and **Figure 4.3** for TiO_2 infiltration.

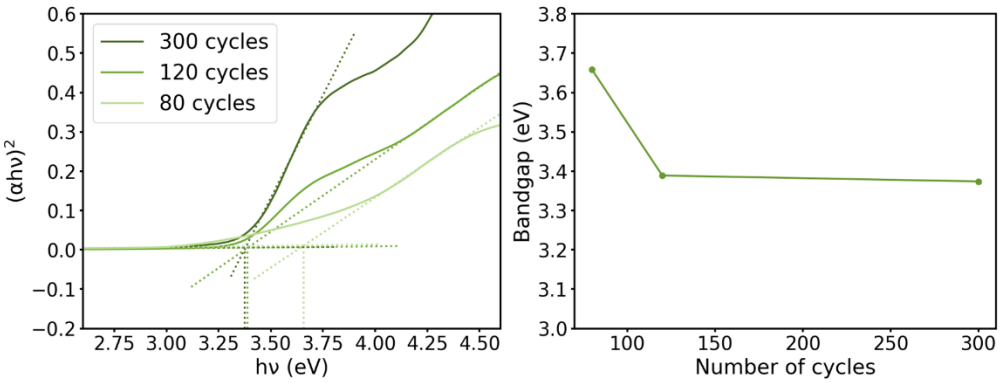

Figure 4.2. Tauc plots and obtained bandgaps for jeans fiber treated with 80, 120 and 300 ZnO infiltration cycles.

ZnO is a direct bandgap semiconductor so the γ factor in the Tauc plots is taken as ½. After 80 infiltration cycles the bandgap of the hybrid fiber obtained is of 3.66 eV (339 nm). Increasing the number of infiltration cycles further reduces the bandgap to 3.40 eV (365 nm) after 120 cycles and 3.37 eV (368 nm) after 300 cycles. The final bandgap value matches that of bulk ZnO at room temperature [62].

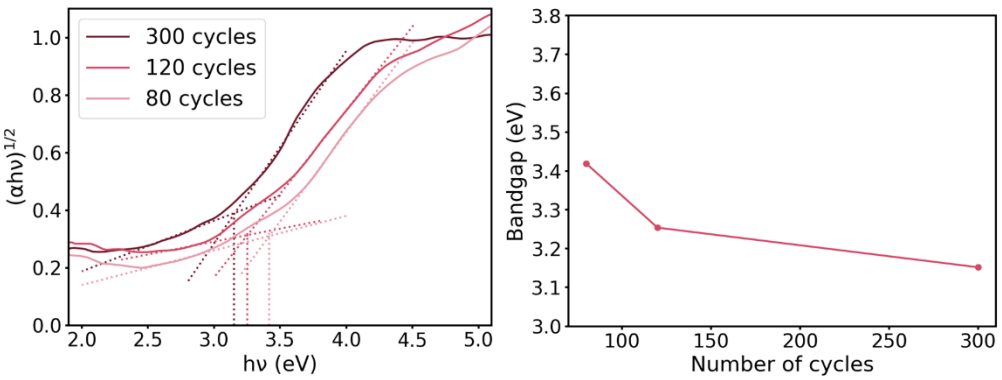

Figure 4.3. Tauc plots and obtained bandgaps for jeans fibers treated with 80, 120 and 300 TiO_2 infiltration cycles.

Amorphous TiO_2 is an indirect bandgap semiconductor, accordingly the γ factor is now taken as 2. The calculated bandgaps are 3.42 eV (363 nm) after 80 infiltration cycles, 3.25 eV (381 nm) after 120 and 3.15 eV (394 nm) after 300. In this case, the last two bandgaps are within the margin of error of the bandgaps measured for different phases of bulk TiO_2, which is usually taken as 3.2 eV for anatase [63].

In both cases, the bandgap of the fiber is effectively reduced by over 2 eV after infiltration. This variation displaces the absorption of the fabrics well into the UVA radiation region, so that they can block most UVR from reaching the skin.

4.1.2. Ultraviolet Protection Factor (UPF)

The Ultraviolet Protection Factor (UPF) is a standard used to quantify the effectiveness of photoprotective fabrics. It is similar to the Sun Protection Factor (SPF), the standard used to measure the effectiveness of sunscreens. The UPF of a cloth represents how much erythemally-weighted UVR is transmitted through its fabric. In contrast to SPF measurements, which only consider erythema caused by UVB radiation, UPF measures all wavelengths of solar light transmitted through the clothing and applies weighting constants to mathematically mimic SPF testing:

$$UPF = \frac{\sum_{280\ nm}^{400\ nm} E_\lambda\ S_\lambda\ \Delta\lambda}{\sum_{280\ nm}^{400\ nm} E_\lambda\ S_\lambda\ T_\lambda\ \Delta\lambda} \tag{4.1}$$

where E_λ is the relative erythemal spectral effectiveness, a constant that adjusts for the ability of each wavelength (λ) to generate cutaneous erythema; S_λ is the solar spectral irradiance, a constant that represents sun intensity at each wavelength at 12 pm in Albuquerque, New Mexico [64]; T_λ is the average measured spectral transmittance of the specimen and $\Delta\lambda$ is the measured wavelength interval. As shown in **Figure 4.4**, these constants heavily weigh UPF toward the UVB range since this is the radiation that primarily induces erythema in the skin.

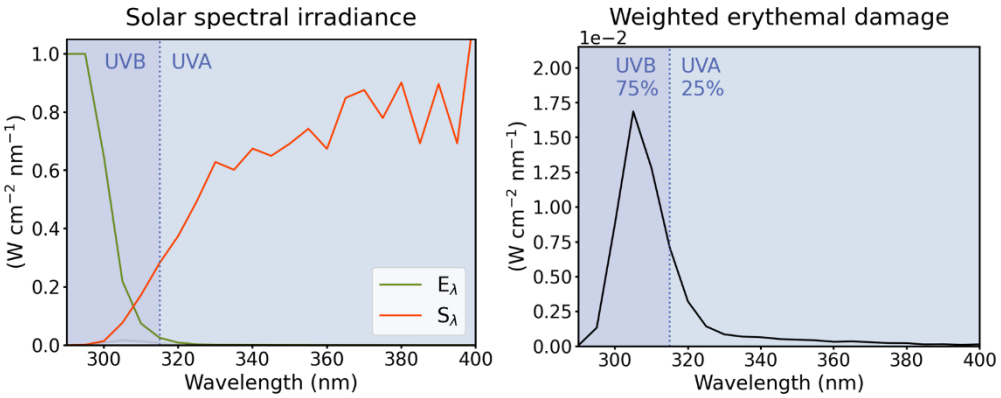

Figure 4.4. Solar spectral irradiance (S_λ) and erythemal effectiveness function (E_λ), when multiplied give the weighted erythemal damage of UV radiation considered in the ultraviolet protection factor (UPF).

UPF calculations also allow us to obtain the absorbance of the fabrics in the UVB and UVA regions independently as:

$$\%\ UVB\ Blocking = 100 - \frac{\sum_{280\ nm}^{315\ nm} T_\lambda\ \Delta\lambda}{\sum_{2805\ nm}^{315\ nm} \Delta\lambda} \tag{4.2}$$

$$\%\ UVA\ Blocking = 100 - \frac{\sum_{315\ nm}^{400\ nm} T_\lambda\ \Delta\lambda}{\sum_{315\ nm}^{400\ nm} \Delta\lambda} \tag{4.3}$$

It is important to note that UPF usually refers to a complete fabric or a piece of clothing. In our case it has been calculated for the individual fibers that form each thread in the fabric. Each thread is made out of tens of these fibers and woven to create the fabric. Consequently, the repeated overlapping of fibers multiplies their protective effectiveness.

The UPF and the UV-blocking percentages in the UVB and UVA regions of jeans fibers before and after infiltration of ZnO or TiO_2 are shown in **Figure 4.5**. The UPF of the untreated fiber is 1.3. This value increases linearly with the number of ZnO infiltration cycles, to 1.7, 2.1, and 3.5 for 80, 120, and 300 cycles, respectively. In the case of TiO_2 the increase is much more pronounced at higher cycle numbers, increasing to 1.9, 2.5, and 9.3 for 80, 120, and 300 cycles, respectively.

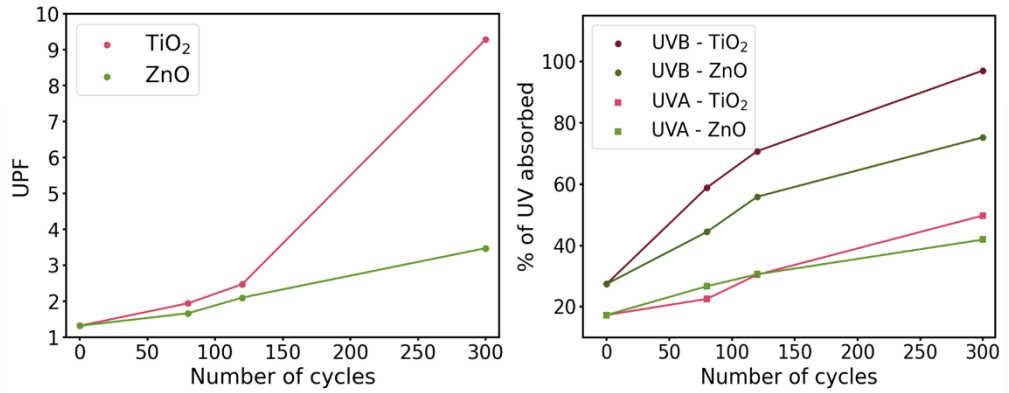

Figure 4.5. Ultraviolet protection factor (UPF) and UV-blocking percentages in the UVB and UVA regions for jeans fibers before and after different infiltration cycles of ZnO and TiO_2.

The untreated fibers block 17% of the UVA and 27% of the UVB radiation. The tendency of the increase of UVA-blocking is similar for both metal oxides, reaching values of 27% and 23% after 80 cycles and of 42 and 50% after 300 cycles of ZnO and TiO_2, respectively. UVB-blocking, however, is more effectively enhanced with the infiltration of TiO_2 than of ZnO. The fibers infiltrated with 80, 120 and 300 cycles of ZnO absorb 44, 56 and 75% of the UVB radiation, while those infiltrated with TiO_2 absorb 59, 71 and 97% of the UVB radiation with equivalent treatments. This difference accounts for the divergence of the UPF of TiO_2-infiltrated fabrics, making them more efficient in blocking the erythema-inducing wavelengths of sun radiation.

4.2. Self-Cleaning

Self-cleaning materials have the ability to remove dirt from their surfaces without external human action. This is of great interest for the textile industry, where this property can be applied to fabrics that are exposed to harsh environmental conditions, like awnings or outside upholstery, which are difficult to clean and replace. It is also applicable in situations where cleanness and hygiene are crucial, like sheets, towels and uniforms used in healthcare. Additionally, reducing the frequency with which fabrics need to be washed both extends their longevity and avoids waste production associated with washing. This can contribute to the reduction of the

environmental impact, one of the greatest challenges that the textile industry currently faces.

Self-cleaning activity can be achieved in two ways: i) using photocatalysis to degrade stains from the fabrics under sunlight, or ii) making them hydrophobic for enabling removal of dirt by the action of water droplets rolling off the material surface. Therefore, to create self-cleaning fabrics it is recommended to control the wettability of their surfaces as well as their photocatalytic activity [34]. The wetting properties of fabric can be modified using metal oxides. These metal oxides, which typically have high surface energies, alter the fabric surface to enhance liquid repulsion. Among various semiconducting metal oxides, ZnO and TiO_2 are most used as photocatalytic self-cleaning coatings due to their excellent physicochemical properties, abundance, and biocompatibility [65].

4.2.1. Chemical Self-Cleaning: Photocatalysis

The decomposition of dirt, harmful microorganisms, and organic pollutants by using photocatalysis is the main mechanism of chemical self-cleaning. Photocatalytic materials utilize the energy from light, typically ultraviolet (UV) or visible light, to accelerate chemical reactions that can degrade pollutants. The proposed photocatalytic self-cleaning mechanism of our hybrid organic-inorganic fabrics is schematized in **Figure 4.6** and described by **Equations 4.4** to **4.9**.

ZnO and TiO_2 absorb sun light radiation with an energy ($h\nu$) higher than their bandgap energy level. This energy can photo-excite the electrons of the valence band promoting them to the conduction band, which generates electron-hole pairs of highly active electrons (e^-) in the conduction band and positive holes (h^+) in the valence band. These pairs can react in three possible pathways: recombination, photoreduction and photooxidation. In recombination the electron-hole pairs quickly recombine on the surface or in the bulk of the photocatalyst without any further reaction. In photoreduction and photooxidation, the charge carriers react with adsorbed water and atmospheric oxygen molecules generating reactive oxygen species (ROS). Electrons diffuse to the surface of the photocatalyst and reduce O_2 generating superoxide radicals (O_2^-). Holes oxidize water

molecules or adsorbed hydroxide ions forming hydroxyl radicals ($\cdot OH$). These species are quite active and readily initiate redox reactions with the organic contaminants in their surroundings breaking them down to harmless compounds such as water and carbon dioxide [66], [67].

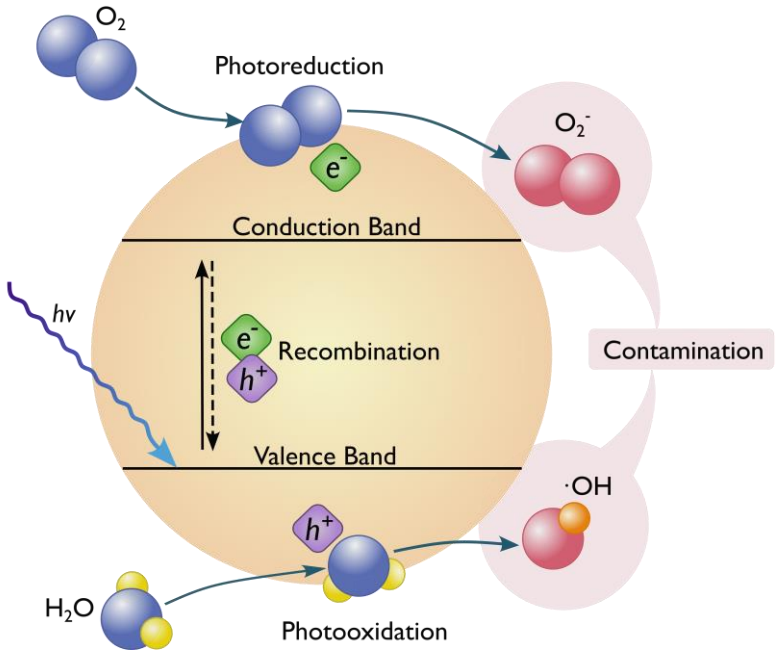

Figure 4.6. Schematic diagram of the photocatalytic self-cleaning mechanism. Based on [66].

$$MO_x + h\nu \rightarrow e^- + h^+ \tag{4.4}$$

$$e^- + h^+ \rightarrow MO_x \tag{4.5}$$

$$e^- + O_2 \rightarrow O_2^- \tag{4.6}$$

$$h^+ + H_2O \rightarrow \cdot OH + H^+ \tag{4.7}$$

$$h^+ + O_2^- \rightarrow 2\,\cdot O \tag{4.8}$$

$$H^+ + O_2^- \rightarrow HO_2^{\cdot} \tag{4.9}$$

As seen from the UV-Visible spectra and the bandgap calculations, the hybrid fibers absorb light in the UV and near visible regions. In order to measure the photocatalytic activity of the treated textiles, we studied the degradation of rhodamine B dye under simulated sunlight conditions. Light was generated with a xenon lamp and an AM1.5G optical filter that

recreates the standard solar spectrum at the Earth's surface with wavelengths between 300 and 1100 nm. Cut pieces of woven fabric of 2x2 cm^2 were immersed into 10 mL of 10^{-5} M rhodamine B (RhB) aqueous solution in glass vials. The vials were placed in an ice bath to avoid variations in the concentration through heating and evaporation. Before measuring, the solution was kept in the darkness for 2 hours to ensure an adsorption-desorption equilibrium between RhB and the sample. A solution of RhB without any submerged sample and a solution of RhB with a pristine sample were measured as references. The degradation of RhB was followed by measuring its UV-Visible absorption spectrum with a NanoDrop 2000c spectrophotometer at regular time intervals for 5 hours.

Before measuring the photocatalytic activity, a darkness test, in which the fabrics were submerged in RhB without any illumination, was carried out. Jeans samples can reduce the concentration of organic dye without a light source, both before and after treatment, meaning that other forms of absorption or degradation simultaneously take place, probably a consequence of unknown dying and other chemical processing of the fabrics during manufacturing. Similarly, samples infiltrated with TiO_2 also show degradation in the darkness due to chlorine residues from $TiCl_4$ which boost the electrochemical degradation of RhB [68]. These mechanisms are also present under illumination and cannot be distinguished from photodegradation. Therefore, to ensure that the degradation measured is only a consequence of the photocatalytic activity introduced by the VPI treatment, the results presented in this section focus on cotton samples infiltrated with ZnO.

4.2.1.1. Dependence on the number of cycles

The dependence of the photocatalytic activity on the number of cycles was studied at a fixed process temperature of 100°C. According to first-order kinetics, the photodegradation reaction rate k of RhB is given by the following equation:

$$\ln \frac{C}{C_0} = -kt \tag{4.10}$$

where C_0 is the initial rhodamine B concentration and C is the RhB concentration at a given irradiation time t [69].

The results obtained are plotted in **Figure 4.7**. The reduction of RhB concentration when irradiating untreated cotton fabric is the same as when irradiating the RhB solution, showing some low level of autocatalytic decomposition of the dye over time. The reduction of RhB concentration observed in contact with infiltrated samples is considerably higher and results from the photocatalytic activity of the hybrid fabrics. The photocatalytic activity increases with the number of infiltration cycles. Samples treated with just 20 cycles of ZnO infiltration degraded over 65% of the RhB in 5 hours, but samples treated with 100 and 300 cycles degraded 80% and 85%, respectively. Finally, samples infiltrated with 500 cycles degraded around 90% of RhB in the same time.

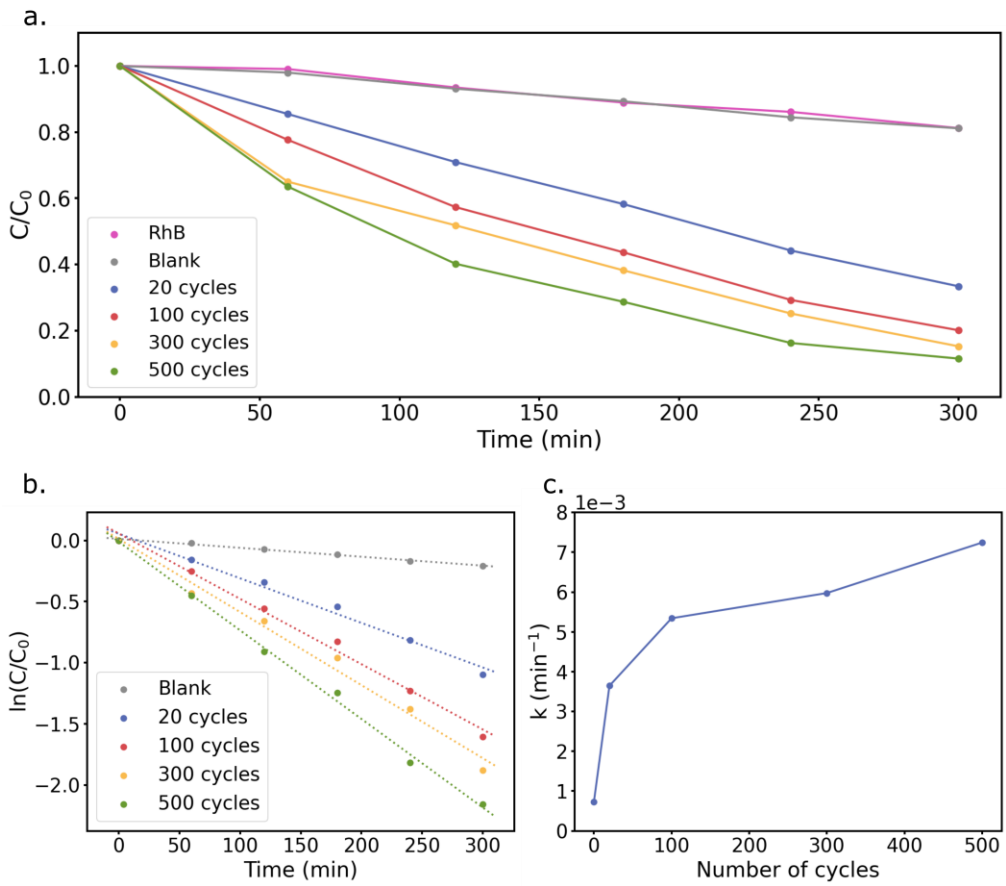

Figure 4.7. (a.) Relative concentration of RhB as a function of irradiation time, (b.) fist-order kinetic analysis and (c.) photodegradation reaction rate (k) for cotton samples treated with different numbers of ZnO infiltration cycles at 100°C.

The percentage of degraded RhB increases with the number of cycles. This is expected since the amount of photocatalytic material should also increase. However, there are other factors that also affect the photodegradation like the charge carrier diffusion length or the exposed surface area, thus a higher amount of material does not necessarily directly imply higher effectiveness. To obtain a better comparison between samples, their photodegradation reaction rate can be obtained from the fitting of the degradation curves following **Equation 4.10**. After 20 cycles of ZnO infiltration, the reaction rate is of 3.64×10^{-3} min^{-1}. After 100 cycles, it reaches 5.34×10^{-3} min^{-1}, increasing by 50% in just 80 cycles. The next 200 cycles (300 cycles in total) only cause an increase of 12% in the photodegradation reaction rate, and the last 200 (500 cycles in total) account for an increase of 21%. Therefore, an increase in the number of infiltration cycles does not result in a proportionally higher photodegradation reaction rate. In order to maximize the efficiency of the processing of hybrid fibers, it is important to consider a compromise between their photocatalytic activity and other parameters like the duration of the infiltration process, its material and time consumption and thus the cost.

4.2.1.2. Dependence on the process temperature

In order to study the effect of the temperature of the reactor during the infiltration process, samples were prepared with a fixed number of cycles of 300 by varying the process temperature from 60 to 140°C. The results are shown in **Figure 4.8**. The reduction of RhB, and consequently the photocatalytic activity, slightly increases with the temperature of the process chamber from 60, where it degrades 82% of the dye after 5 hours of irradiation, to 100°C, where it reaches its maximum at 85%. When the process temperature is further increased, the photocatalytic activity decreases: Samples infiltrated at 120°C degrade 78% and samples infiltrated at 140°C degrade 72% of the RhB in the same irradiation time. From the calculated reaction rates, the photocatalytic activity is not too much dependent on the process temperature in the window between 60 and 100°C, where the reaction rates vary from 5.60 to 5.98×10^{-3} min^{-1}. A further increase of the process temperature negatively affects the photocatalytic activity of the hybrid fabrics, reducing the reaction rate to 4.97×10^{-3} min^{-1} at 120°C and 4.37×10^{-3} min^{-1} at 140°C.

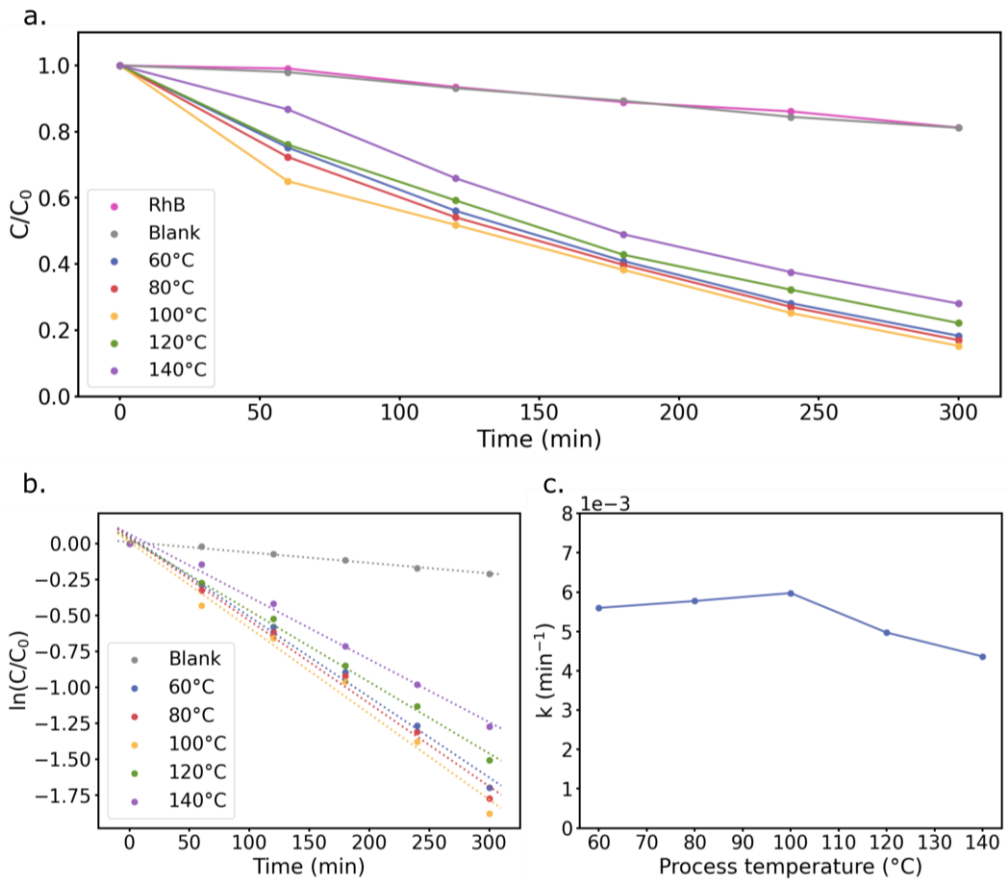

Figure 4.8. (a.) Relative concentration of rhodamine B as a function of irradiation time, (b.) first-order kinetic analysis and (c.) photodegradation reaction rate (k) for cotton samples treated with 300 ZnO infiltration cycles at different process temperatures.

This maximum photodegradation efficiency at low temperatures around 100°C has been previously reported for ALD-grown ZnO both on silicon substrates [70] and on collagen fibers in bactericidal applications [71], although a commonly accepted explanation has not been found. There are various characteristics of the structure of ZnO that can affect its photocatalytic activity, including the crystallite size, the preferential orientation, and the presence of defects being the most relevant ones. The XRD diffraction patterns obtained from the cotton fabrics after 300 ZnO infiltration cycles at different process temperatures and the structural parameters obtained from them are shown in **Figure 4.9**.

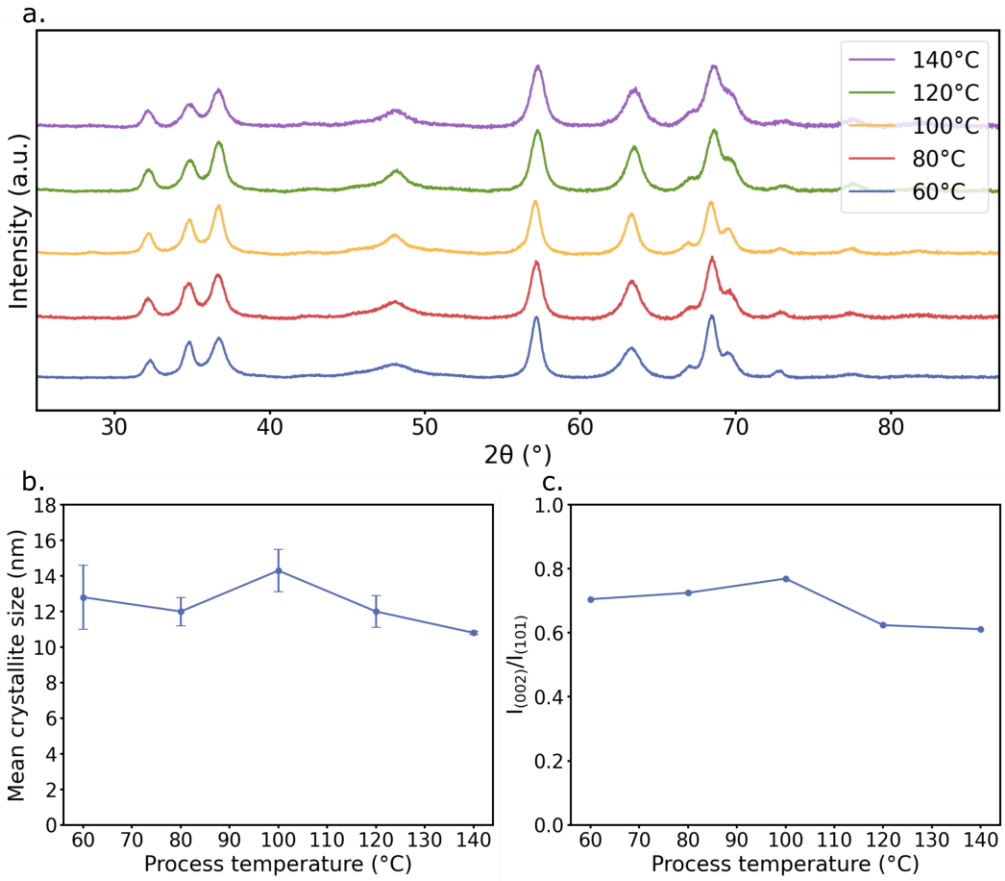

Figure 4.9. (a.) XRD patterns of cotton fabrics treated with 300 ZnO infiltration cycles at different process temperatures, (b.) ZnO mean crystallite size and (c.) ratio of the intensities of the (002) and (101) peaks as a function the process temperature.

Although the XRD diffraction patterns of the infiltrated ZnO at the different process temperatures are very similar, some differences are found from a closer analysis of their features. The mean crystallite sizes are related to the position and width of the peaks and can be obtained by applying the Debye-Scherrer formula (**Equation 2.2**). The mean crystallite size decreases at process temperatures higher than 100°C, following a similar trend as the photodegradation reaction rate. This tendency is in good agreement with literature reports on ALD-grown ZnO [70], [72]. The existence of crystallite boundaries affects the mobility of the charge carriers, a larger crystallite size allows longer mean free paths of the carriers, allowing stronger participation in the photoreactions and enhancing the photocatalytic activity. This increase is limited once the crystallite size exceeds the maximum diffusion length of charge carriers. In

this case the carriers recombine before reaching the surface and do not contribute to the photodegradation [73]. However, this saturated regime is not reached in the studied hybrid fabrics.

The crystallographic orientation of the ZnO crystals can be determined from the intensity of the triplet of diffraction peaks found between 30 and 40°, corresponding to the (100), (002) and (101) planes. The (002) plane is a Zn-terminated polar plane with high surface energy, where polar organic molecules like RhB preferentially adsorb. In contrast, the (100) and (101) are non-polar planes with lower surface energy [73]. Consequently, the degradation of pollutants is more favorable on the (002) surfaces and maximizing the (002)/(101) ratio increases the photocatalytic efficiency. The infiltrated ZnO grows predominantly in the (101) direction at all the process temperatures studied. However, the (002) direction is also prevalent at lower temperatures, with intensities of 70-77% that of the (101) peak. At temperatures above 100°C, this orientation is less common, reducing the intensity of the peak to about 60%. This tendency again matches that of the photodegradation reaction rate.

The presence of defects is related to deformations of the unit cell. Although infiltrated ZnO has a compressed unit cell at all studied process temperatures, no clear tendency relating deformation with the photocatalytic activity of the hybrid fabrics has been found.

4.2.1.3. Durability of the photocatalytic activity

Finally, we tested whether the hybrid fabrics preserve their photocatalytic activity and can be reused. This is a key feature since a progressive reduction in the photocatalytic efficiency of self-cleaning fibers prepared by wet-chemical methods such as dip coating [74], [75], [76], spin coating [77], or liquid phase deposition [78] has previously been reported after repetitive application. This decrease is attributed to the rather weak physical bonding between fibers and metal oxides, as opposed to the strong, chemical bonding that can be achieved through VPI. For this study, a sample of cotton, infiltrated with 300 cycles of ZnO at 100°C, was selected. The measurement of the RhB degradation was repeated 4 times, allowing the sample to fully dry between each repetition. The results obtained are shown in **Figure 4.10**. During the first 5 hours, 85% of the RhB is degraded. The effectiveness of the degradation is slightly reduced in

the following repetitions, to 75% during the second one, 73% during the third one and 77% during the fourth one. The stabilization of this magnitude after the first measurement shows that the infiltrated fabrics maintain their photocatalytic self-cleaning activity. This also confirms the quality of the chemical bonding between cotton and ZnO and makes the resulting self-cleaning hybrid textiles repeatedly usable.

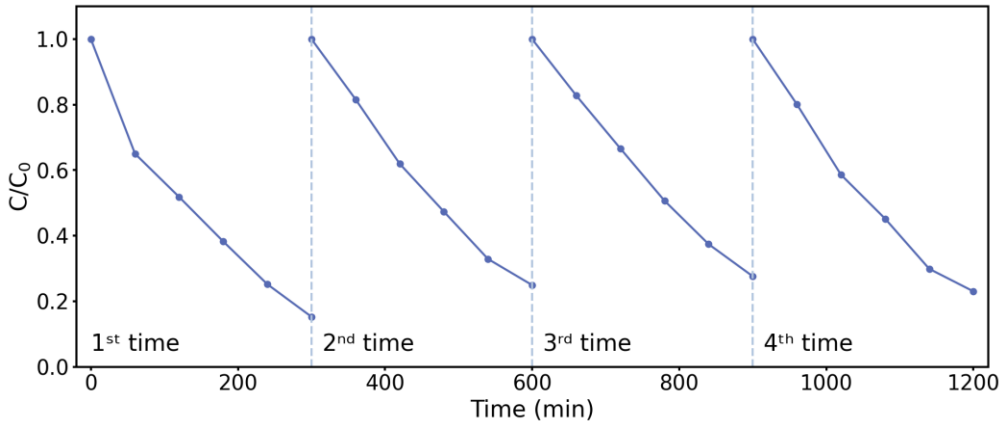

Figure 4.10. Relative concentration of RhB as a function of irradiation time. Repetitive measurement of a cotton sample treated with 300 ZnO infiltration cycles at 100°C.

4.2.2. Physical Self-Cleaning: Hydrophobicity

The fundamental principle of physical hydrophobic self-cleaning technology is the elimination of dirt particles from the surface by uptake and removal with droplets of water. In the case of hydrophobic surfaces, the water droplets roll off the surface quickly due to their water repellent and low adhesive properties, picking up and removing contaminants and dirt from the surface as they advance. This hydrophobic self-cleaning mechanism is schematized in **Figure 4.11**.

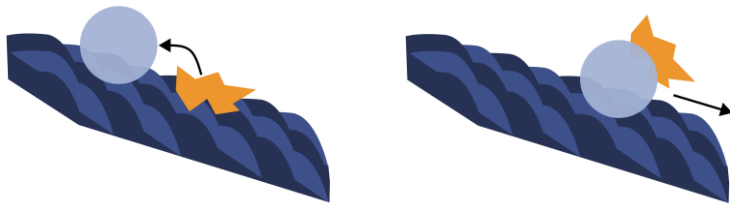

Figure 4.11. Schematic diagram of the hydrophobic self-cleaning mechanism.

The most well-known example of a naturally self-cleaning superhydrophobic surface is the lotus leaf, which is rough and shows a hierarchical structure overlay of micro and nanostructures with a thin surface layer of wax, resulting in excellent water repulsion [79].

To study the hydrophobicity of the treated textiles, we measured their water contact angle and water absorption capacity. The untreated raw cotton woven fabric had a superhydrophobic surface before any treatment. The jeans fabric, in contrast, has a hydrophilic surface and absorbs water droplets very rapidly. For this reason, the following discussion focuses on the changes achieved in the wettability of jeans upon VPI treatment.

4.2.2.1. Contact angle

We measured the contact angle of 10 µL distilled water droplets on the hybrid jeans surface. The results are shown in **Figure 4.12**. The contact angle on the untreated jeans fabrics could not be measured since the water droplets immediately spread and became absorbed by the fabric. After treatment, the fabrics became superhydrophobic, with contact angles between 120 and 130°, even after just 5 infiltration cycles of both metal oxides. In the case of ZnO, the contact angle increased from 121° after 5 infiltration cycles to 126° after 80 cycles and stabilized around 126° for higher cycle numbers. In the case of TiO_2, the rise of the contact angle after the first infiltration cycles was steeper, rising from 121° after 5 infiltration cycles to 126° after 20 cycles. The contact angle had a minimum of 117° around 100 infiltration cycles and stabilized around 124° after 140 cycles.

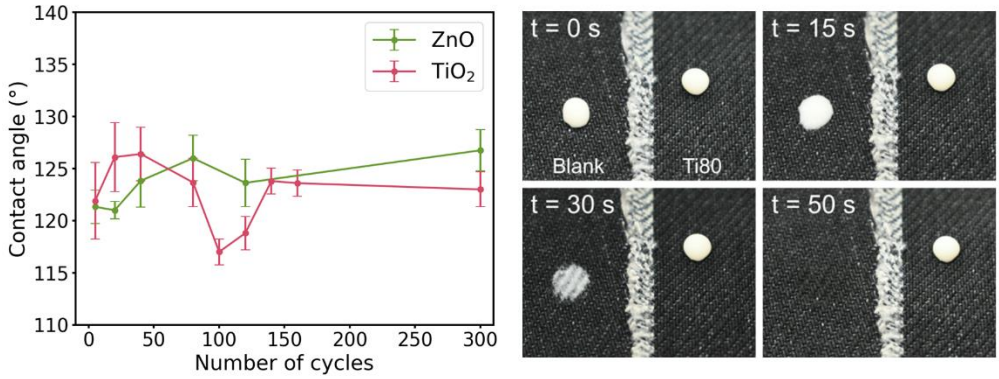

Figure 4.12 Water contact angle as a function of the number of cycles for jeans infiltrated with ZnO or TiO_2 and comparison of the time evolution of a milk drop on pristine jeans and on jeans treated with 80 TiO_2 infiltration cycles.

Besides the contact angle, another indicator of the self-cleaning capacity of the hydrophobic fabrics is the time the droplets remain on the surface without being absorbed. **Figure 4.12** shows the difference between the time evolution of a milk drop on untreated jeans and on jeans after 80 TiO_2 infiltration cycles. A drop of milk (~90% water) was used instead of water to increase the clarity of the images. The pristine fabric started absorbing the drop after just 15 seconds. After 30 seconds most of the drop is absorbed and after 50 seconds the milk is completely absorbed staining the fabric. In the case of the hybrid fabric, the milk drop stays on top of the surface forming a sphere with a low contact area, this shape does not change during the 50 seconds. Similarly, water droplets stayed between a minute and an hour without being absorbed on surfaces of all infiltrated jeans.

4.2.2.2. Water absorption capacity

The measurements of water absorption capacities of the fabrics were carried out according to ISO 62 [45]. 2x2 cm^2 samples were initially dried at 60°C overnight. After measuring the dry mass of the samples, they were immersed in 80 mL of distilled water and weighed with a high precision balance at different time intervals. The water absorption capacity coefficient, w_{AC}, was calculated according to the following equation:

$$w_{AC} = \frac{m_t - m_0}{m_0} \tag{4.11}$$

where m_0 corresponds to the initial dry mass of the sample and m_t to the measured mass at each time interval.

The obtained water absorption capacity coefficients are shown in **Figure 4.13**. Samples infiltrated with both ZnO and TiO_2 absorb less water than untreated samples. This difference is most noticeable during the first 5 minutes, when the treated samples float on the water surface while the untreated samples sink immediately. During the first 30 seconds, the pristine jeans fabric absorbs 1.5 times its own weight in water, while treated samples needed between 4 or 5 minutes to do so. The hybrid fabrics absorbed 60% less water than the untreated ones during the first minute of immersion. During the following 12 minutes the water content stabilized to 50% less than in the untreated fabrics. From this point, the

water absorption of untreated fabrics decreased, reducing the difference in absorption to 30% after 17 minutes of immersion. These values remained constant during the following minutes of immersion.

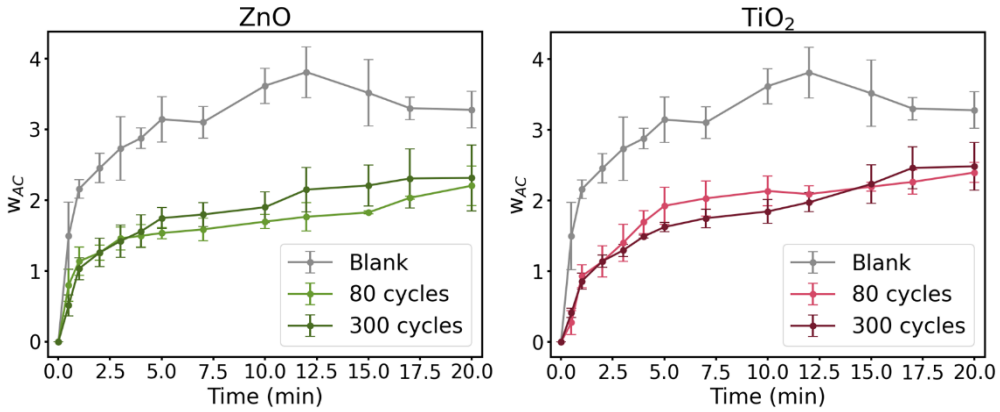

Figure 4.13. Water absorption capacity coefficient as a function of time of jeans treated with 80 and 300 infiltration cycles of ZnO and TiO_2.

The reduction of the water absorption coefficient is independent of the metal oxide and the number of infiltration cycles, meaning that the hydrophobicity of the fabrics is a consequence of the modification of the surface of the polymers. Once it is covered, neither the extra amount of material nor its chemistry play a role in changing the wettability of the surface.

4.3. Antimicrobial activity

Textiles are often used as a barrier that protects our skin from harmful agents from the environment. However, fibers can provide habitat to microbes themselves by supporting the growth of bacteria and fungi. The appearance of microbial growth on textiles can cause unpleasant odors, physical irritation, infectious diseases and damaging and discoloration of the fabrics [15]. Natural fibers, like cotton, are particularly susceptible to microbial attacks, especially after fabric processing in which their protective layers are removed since their molecular structure provides readily accessible nutrients and energy sources for microbes [80].

Antimicrobial textiles are fabrics designed to either kill microorganisms, such as bacteria, fungi, and viruses, which is known as a biocidal mechanism, or inhibit their growth, which is referred to as a biostatic mechanism. Antimicrobial fabrics can also be classified as leaching type, when the antimicrobial agent is released from the material into the surrounding environment where it interacts with the microbes, or non-leaching type, when the antimicrobial agent is bound to the material's surface where it kills or inhibits microbes through direct contact. Antimicrobial textiles have a wide variety of applications, but when it comes to clothing, a biostatic, non-leaching type of fabric is preferred [81]. The combination of these two mechanisms is considered safer for direct skin contact, as it helps to avoid adverse effects on human skin by preserving its natural bacterial flora while maintaining long-term antimicrobial activity.

The addition of metallic and metal oxide nanoparticles is a common method for the fabrication of biostatic, non-leaching antimicrobial textiles. However, the stabilization of the nanoparticles on the surface of cellulose-based fabrics is still a challenge [81]. Alternatively, the strong chemical bonds between the textile fibers and the metal oxide, achieved with VPI, allow to obtain a durable functional textile. Here, we study both the antibacterial and antifungal activity of the hybrid organic-inorganic fabrics.

4.3.1. Antibacterial activity

The bacteriostatic activity of the hybrid fabrics was evaluated against the bacterial strains *Staphylococcus aureus* (*S. aureus*, ATCC 35556) and *Escherichia coli* (*E. coli*, ATCC 25922), the most common model organisms for gram-positive (GRAM+) and gram-negative (GRAM-) bacteria, respectively.

The attachment and proliferation of both bacteria strains on raw cotton and jeans infiltrated with ZnO and TiO_2 were evaluated following the protocol described in **Chapter 2** and using the corresponding pristine fabric as positive control. Samples of 2x2 cm^2 were inoculated with 400µL of a bacterial suspension of $5x10^5$ colony-forming units per milliliter

(CFUs/mL) and incubated at 37°C overnight. After incubation, the samples were washed with phosphate buffered saline (PBS) to remove the bacteria that could not adhere to the textile. Samples were then sonicated for 10 min in 10 mL of PBS to release the bacteria attached to the textile. This solution is serially diluted, plated and incubated following the standard plate count method to obtain the number of viable bacteria attached to the sample (CFU). The antibacterial activity of the infiltrated fabrics, *R*, is defined by the following equation:

$$R = \log(CFU_{Control}) - \log(CFU_{Sample}) \quad (4.12)$$

taking the pristine fabrics as control. According to ISO 22196 [82], a material can be considered antimicrobial when it has an antibacterial activity of $R>2$, corresponding to a bacterial reduction of >99%.

Both raw cotton and jeans permit bacterial attachment before infiltration. On average, $3.1\text{x}10^6$ CFUs of *S. aureus* and $8.3\text{x}10^7$ CFUs of *E. coli* can attach to the surface of raw cotton, and $2.0\text{x}10^6$ CFUs of *S. aureus* and $2.7\text{x}10^6$ CFUs of *E. coli* to the jeans surface. Following the precision of the plate count method, the minimum amount of CFU that can be considered to be correct is $<2\text{x}10^3$ CFUs, even when no colonies are seen on the plate. Therefore, this limits the maximum antibacterial activity achievable to 3.19 for *S. aureus* and 4.61 for *E. Coli* in the case of cotton, and to 3.00 for *S. aureus* and 3.13 for *E. coli* in the case of jeans. The antibacterial activity values obtained are shown in **Figure 4.14.** Overall, all the hybrid fabrics showed a reduction in bacterial attachment, although not all of them met the required $R>2$ standard to be considered antimicrobial. Raw cotton infiltrated with ZnO presented antimicrobial activity against both GRAM+ and GRAM- bacteria. Only the sample treated with 5 cycles shows a weaker antibacterial activity and cannot sufficiently prevent the attachment of *E. coli*. Raw cotton treated with TiO_2 needed 40 infiltration cycles to prevent the attachment of *S. aureus* and cannot be considered bacteriostatic against *E. coli* with the antibacterial activity being between 1 and 1.5, corresponding to a bacterial reduction of between 90 and 97%. Jeans infiltrated with both ZnO and TiO_2 showed no attachment of either of the bacteria, reaching the maximum achievable antibacterial activity in all cases. Only the samples treated with 5 ZnO infiltration cycles allowed some

bacterial attachment, but they can still be considered antimicrobial with an antibacterial activity of $R>2$ against both bacterial strains.

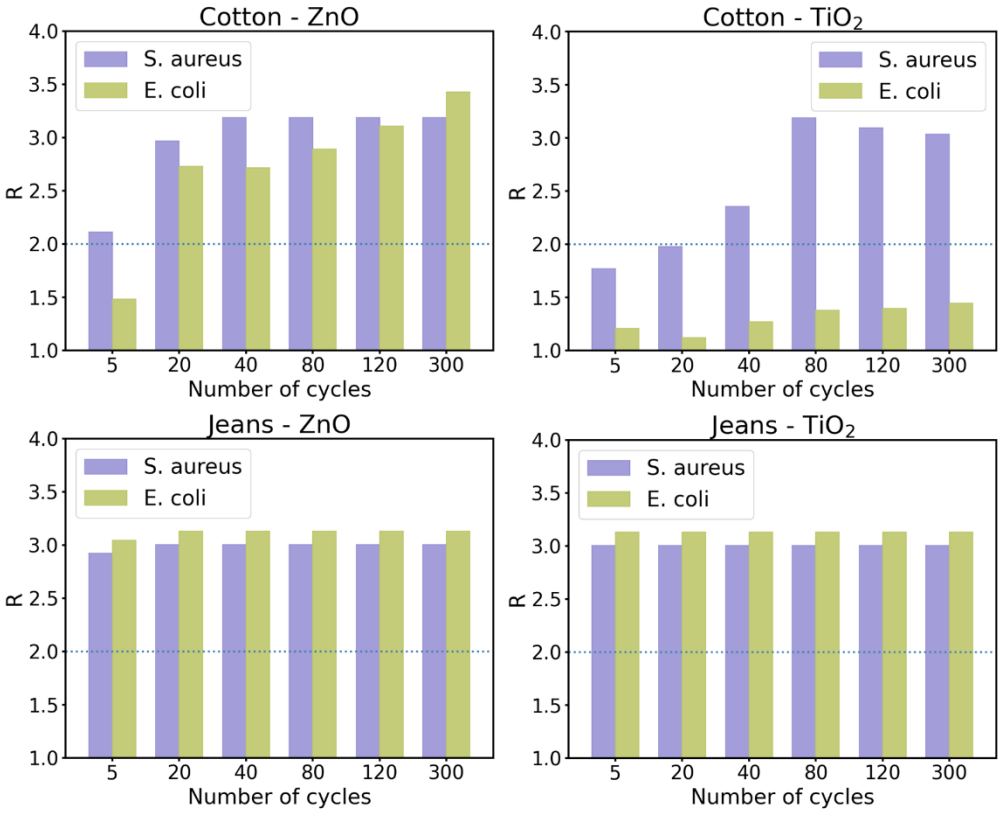

Figure 4.14. Antibacterial activity of cotton and jeans fabrics treated with different infiltration cycles of ZnO and TiO_2 against *S. aureus* and *E. coli*. The blue dotted line marks the R=2 threshold.

Cotton infiltrated with ZnO showed better rejection of the bacteria than that with the equivalent cycle number of TiO_2-infiltration, especially against *E. coli*. Jeans infiltrated with both ZnO and TiO_2 showed an almost perfect antibacterial activity, superior to that of their cotton counterparts. We can conclude that antimicrobial activity can be achieved in textiles by VPI, however, the original fabric plays a critical role in the effectiveness of the resulting hybrid. This effect probably comes from the influence of the surface morphology on bacterial adhesion. The surface of the textiles should be covered with metal oxide, prohibiting direct interaction with the bacteria. However, due to the characteristic conformality of the coating, the original morphology is preserved and can affect bacterial adhesion. Generally, bacteria adhere to rough surfaces, with features comparable to

the bacteria in size, better than to smooth ones. They tend to preferentially attach along creases rather than to uniformly cover the surface [83]. Additionally, the pretreatment of the jeans fabric during manufacturing can reduce or fully eliminate the indigenous proteins of cotton threads, still present in raw cotton, which support bacterial adherence, further reducing the bacterial attachment [84].

The hybrid cotton fabrics show higher antibacterial activity against *S. aureus* than against *E. coli*. The bacteriostatic activity of metal oxides relies on damaging the cell membranes of the bacteria through direct contact with metal ions and surface features, producing physical stress and electrostatic interactions. Although the cell walls of GRAM+ bacteria have a thicker peptidoglycan layer than GRAM- bacteria, it is directly accessible and more susceptible. GRAM- bacteria have an outer membrane that acts as a barrier, protecting this layer and making them more resistant to antibacterial methods and antibiotics than GRAM+ bacteria [85].

It is important to note that the reactive oxygen species (ROS) produced through photocatalysis can also damage the cell walls of bacteria, contributing to the antibacterial activity of the textiles. Since the incubation of the samples was carried out in darkness, this is not the case in the presented results. They would, however, be involved if the fabrics were exposed to solar light or artificial UV irradiation, adding to the antibacterial activity of the hybrid fabrics.

4.3.1.1. Anti-odor activity

Human sweat is almost entirely odorless by itself. However, bacteria on the human skin can metabolize it, producing volatile organic compounds that cause body odor. Some of the most common skin bacteria involved in this process are the members of the *Corynebacterium* species, mostly associated with axillary odor [86].

In order to study the effectiveness of the hybrid fabrics in the reduction of body odors, we studied their bacteriostatic activity against *Corynebacterium striatum* (*C. striatum*) following the previously described protocol. *C. striatum* is a GRAM+ bacterium, known to be a significant contributor to body odor. It can also lead to infections and is becoming resistant to many antibiotics [87].

Both raw cotton and jeans permit bacterial attachment before infiltration. On average, $1.7x10^6$ CFUs of *C. striatum* can attach to the surface of raw cotton, and $1.4x10^6$ CFUs to jeans. Cotton and jeans fabrics treated with 80 and 300 infiltration cycles of ZnO and TiO_2 were tested, all of them showing the maximum possible reduction of bacteria, with no bacteria attached to the surface and an antibacterial activity of R>2.8. Therefore, the hybrid fabrics prepared via VPI present a satisfactory capacity to prevent body odor.

4.3.2. Antifungal activity

Aspergillus nidulans (*A. nidulans*) was selected as the exemplary fungus for our anti-fungal experiments. *A. nidulans* is a saprophytic filamentous fungus that can be found virtually everywhere due to its simple nutritional requirements and rapid growth. Although it is usually harmless, it can cause opportunistic infections in humans. It can also degrade cellulose, causing weakening, discoloration, and even complete disintegration of fabrics [88].

The antifungal activity of the hybrid fabrics was evaluated against *A. nidulans* by analyzing their ability to inhibit polar extension of actively growing hyphae and to hinder spore germination separately, following the protocols detailed in **Chapter 2**. Quantification of the growth was performed visually, by comparing the fungal growth and hyphal extension observed on the prepared hybrid fabrics to those observed on pristine ones. No reports on the antifungal activity of TiO_2 without the involvement of photocatalytic activity were found in literature, whereas ZnO nanoparticles have been introduced as promising antifungal agents [89]. Therefore, these experiments focused on the evaluation of fabrics infiltrated with 300 cycles of ZnO.

To study the inhibition of the polar extension of growing *A. nidulans*' hyphae, fabric samples of 1x1 cm^2 were distributed radially on a minimal culture medium (MMA) plate, equally distanced from its center, and asexual spores (conidia) were point inoculated at the center. The plates were incubated at 37°C for 24 hours until the periphery of the growing

colony approached the samples. The results obtained are shown in **Figure 4.15**.

Figure 4.15. Inhibition of the polar extension of *A. nidulans*' hyphae for cotton and jeans before and after 300 cycles of ZnO infiltration.

Both raw cotton and jeans permitted the extension of the hyphae before infiltration, the fungus grew on top of the fabrics, covering them without impediments. Moreover, pristine raw cotton seems to have hosted a dormant microbial species which activated during the incubation, expanding to the medium and forming pink colonies that compete with *A. nidulans*. This species could not be identified but seems to be a biofilm-producing bacterium. It was effectively eliminated during the infiltration process due to the prolonged exposure to a higher temperature.

The polar extension of the hyphae was observed on the fabrics infiltrated with ZnO, especially the raw cotton. The growth of the hyphae appeared to be slowed down when reaching the ZnO-infiltrated jeans, however the fungi still grew on top of the fabric. In any case, the result of this test was unsatisfactory as the extension of the fungi appeared to be unaffected by the hybrid fabrics.

Once a fungus is growing as hyphae it becomes more difficult to stop due to its continuous branching and adaptability to harsh conditions, such as lack of nutrients [90]. Inhibiting hyphal growth requires interfering with these ongoing cellular processes, which can be more problematic than targeting a single, discrete germination event.

To study the inhibition of spore germination, conidia of *A. nidulans* were collected from 72-hour old cultures, washed and quantified. 10^5 conidia were diluted in liquid MMA and spread onto MMA plates containing the 1x1 cm^2 fabric samples. The plates were incubated at 37°C for 48 hours

until a mycelium was formed. The results obtained are shown in **Figure 4.16**.

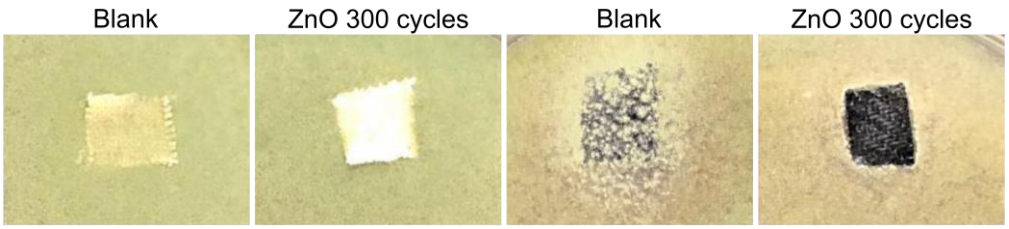

Figure 4.16. Inhibition of the spore germination of *A. nidulans* on cotton and jeans before and after 300 cycles of ZnO infiltration.

Both the pristine raw cotton and jeans appeared significantly covered by fungal growth, confirming that the untreated fabrics have no effect on spore germination. The surfaces of both ZnO-infiltrated fabrics showed no growth, indicating full inhibition of the germination of *A. nidulans* spores. The area of inhibition was reduced to the surface of the samples and the growth of the spores in the area around them was not appreciably affected. This is an indicator of the non-leaching nature of the antifungal activity of the hybrid fabrics, which is preferable in textiles that are in direct contact with human skin.

In conclusion, the prepared hybrid fabrics show partial antifungal activity, being able to inhibit the spore germination of *A. nidulans* but not its hyphal growth. While both cases are important targets for controlling fungal growth, stopping spore germination is key in preserving the integrity and hygiene of fabrics and preventing initial infections.

4.4. Flame retardancy

The development of protective clothing is an increasingly important area in advanced textile engineering. Protective textiles are designed to shield humans from injury or even death caused by natural or industrial hazards, or in the vicinity of hazardous environments. Among the various types of protective textiles, fire protection remains one of the most critical and extensively studied fields.

Natural fibers, cotton in particular, are highly combustible and tend to burn easily and rapidly when exposed to an ignition source. Various biomolecules have been explored in the development of fire-retardant and fire-resistant textiles. However, achieving a self-extinguishing effect typically requires high loadings of these compounds, which negatively impacts the physical and chemical properties of the fabric [91].

Metal oxides have been proposed as an alternative, as they exhibit promising flame-retardant effects at much lower concentrations. Both ZnO and TiO_2 contribute to flame retardancy by acting as heat barriers. As thermally stable inorganic materials, they form an insulating layer on the fiber surface, reducing the transfer of heat, fuel, and oxygen between the flame and the fibers [92]. This results in a lower combustion rate and intensity and suppressed smoke production.

The fire resistance of the hybrid fabrics was evaluated by analyzing their combustion behavior in open air. 2.5×5 cm^2 samples were placed on a metal holder and secured with a magnet, leaving 1 cm of the fabric suspended. One of the suspended corners of the sample was exposed to the flame of a standard lighter until ignition occurred. Fire was allowed to burn either until its extinction or until 4 cm of the sample were burned. Time to ignition, burning duration, char formation, and smoke production were compared visually to those of the pristine fabrics.

The results obtained for raw cotton before and after infiltration are shown in **Figure 4.17**. Untreated cotton ignited immediately upon exposure to the flame. The fire progressed steadily, fully consuming the fabric and reaching the 4 cm mark in less than two minutes. Noticeable smoke was produced during the combustion of the fabric. In the case of ZnO-infiltration, the fabric still ignited quickly upon exposure to the flame, but it self-extinguished fast, within 26 seconds (80 infiltration cycles) and 13 seconds (300 infiltration cycles). The flame affected a considerably smaller area of the fabric, which is not consumed but developed a charred outline around the impacted zone instead. No visible smoke was produced during combustion. In the case of TiO_2-infiltration, the fabric ignited rapidly upon exposure to the flame. However, it self-extinguished faster than the ZnO-infiltrated sample, within 16 seconds (80 infiltration cycles) and 8 seconds (300 infiltration cycles). In this case, although the flame-affected area was

reduced, visible damage was still present. The fabric was partially consumed by the fire and the remaining material appeared scorched. No visible smoke was produced during combustion.

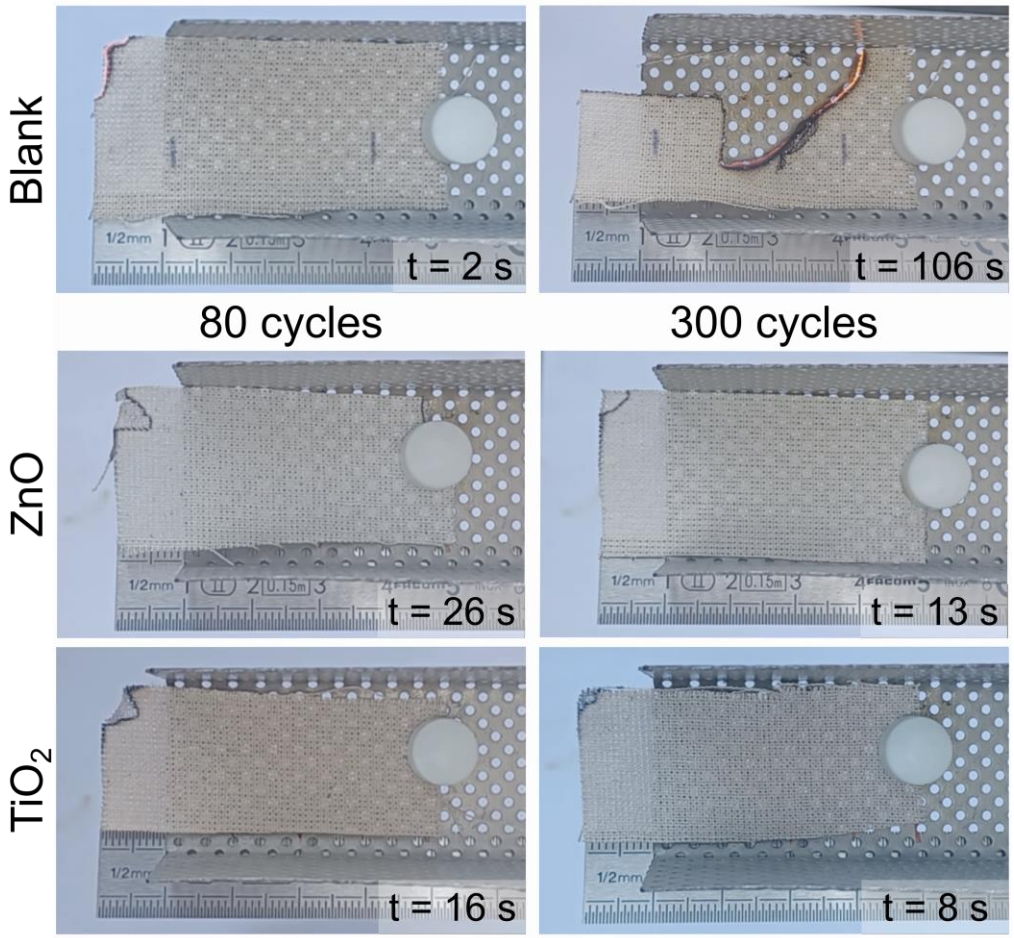

Figure 4.17. Flammability tests of cotton before and after 80 and 300 infiltration cycles of ZnO and TiO_2. The time *t* corresponds to the burning duration until self-extinguishment of the flame or until 4 cm of the sample were burned.

The results obtained for jeans are shown in **Figure 4.18.** Untreated jeans ignited quickly upon exposure to the flame. A large, visible flame formed and spread through the fabric, visibly scorching the material. The textile curled, turned black, and produced a significant amount of smoke during combustion. The fire self-extinguished after 106 seconds, affecting approximately 1 cm of the sample. After infiltration with both ZnO and TiO_2, the fabric required a longer exposure time to the flame for ignition to

occur. In all cases, self-extinguishment took place promptly after the ignition source was removed, with no observable flame propagation. Only the exposed edge of the sample showed slight curling and blackening, following the same burn pattern observed in the pristine fabric. Smoke production was significantly reduced, with little to no visible smoke detected.

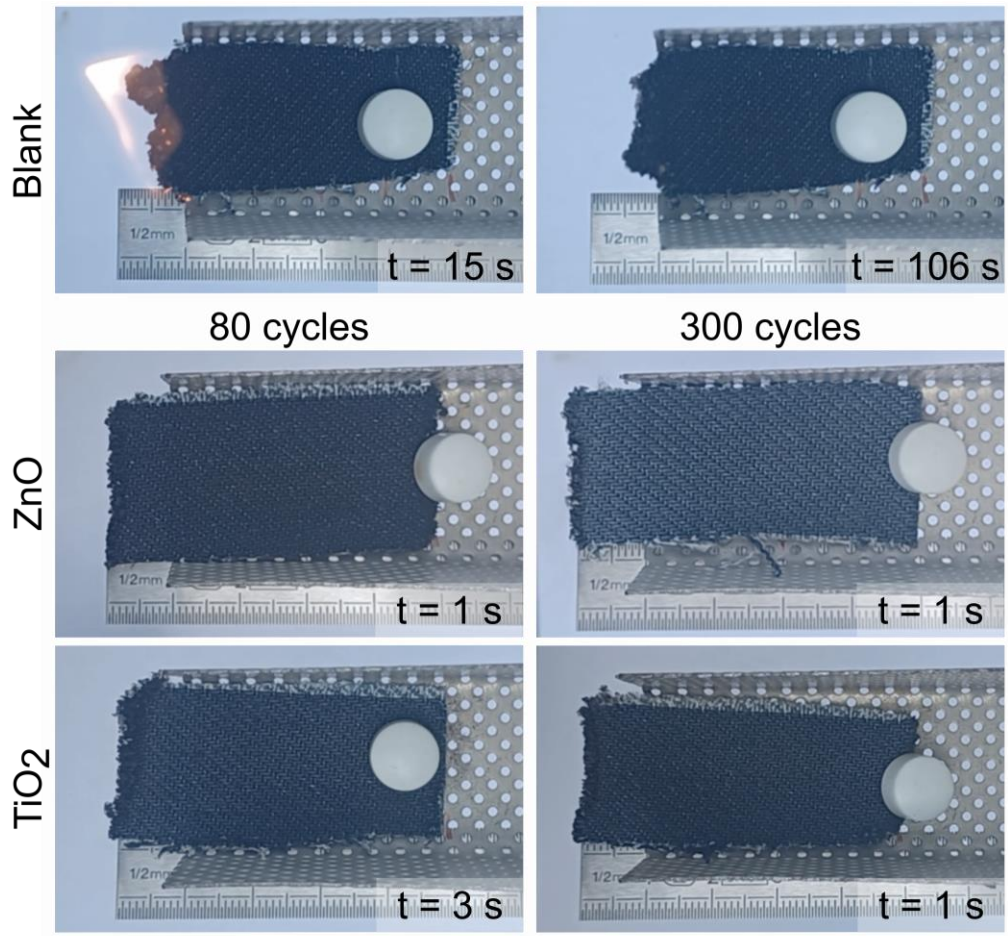

Figure 4.18. Flammability tests of jeans before and after 80 and 300 infiltration cycles of ZnO and TiO_2. The time *t* corresponds to the burning duration until self-extinguishment of the flame.

The hybrid textiles prepared with both ZnO and TiO_2 show a significant flame-retardance performance, reducing the burning time in the case of raw cotton and eliminating it in the case of jeans. In the case of cotton, the hybrid fabrics catch fire upon exposure to the flame, but self-extinguish

after seconds. In the case of ZnO, the burn duration is longer, but the affected material is better preserved, while in the case of TiO_2 the burn duration is shorter, but the affected material is partially consumed and scorched by the fire. In the case of jeans, the time to ignition is significantly reduced and self-extinguishment occurs promptly after removal of the ignition source. Only the very edge of the fabric is damaged after fire exposure. In all cases smoke production is significantly reduced.

4.5. Resistance to laundering

An important matter in multifunctional fabrics is the resistance of the treatment and the durability of the functionalities achieved, as they need to withstand regular washing without deteriorating. Indeed, one of the most common and limiting drawbacks of treated fabrics by methods like sol-gel processing and wet treatments is that they cannot be wetted without damaging the treatment, consequently reducing the potential applicability of their functionalities [66]. The strong chemical bonds and the gradient formed between the textile fibers and the metal oxide achieved with VPI should lead to washable and long-lasting multifunctional textiles.

To ensure the durability of the hybrid organic-inorganic fabrics prepared via VPI, we analyzed their UV-blocking and antibacterial properties after being washed in a regular washing machine 10 times following conventional laundering programs with and without soap. UV protection was measured on the interior fibers while the bacteriostatic activity directly depends on the surface of the fabrics. By confirming the preservation of these two functionalities, we validated the resistance of the infiltration to laundering and expect it to be applicable to other functionalities as well.

4.5.1. Resistance of the UV-protective properties

We measured the UV-Visible absorption of the fibers after being washed, calculated their UV-blocking percentages in the UVB and UVA regions and compared them to the values measured before laundering. Jeans samples

infiltrated with 80 and 300 cycles, either ZnO or TiO_2, were analyzed. The comparison of the UV-Visible absorption spectra measured before and after 10 washing cycles are shown in **Figure 4.19**.

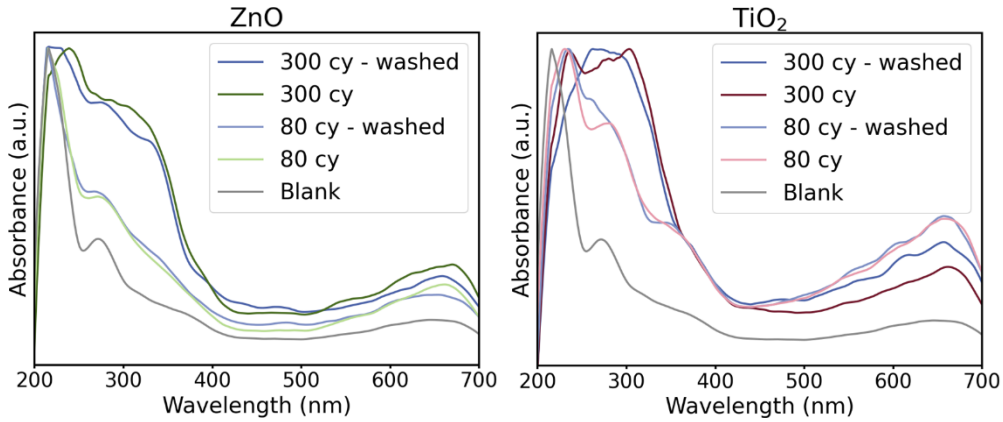

Figure 4.19. UV-Visible absorption spectra of jeans fibers, infiltrated with 80 and 300 cycles of ZnO and TiO_2, before and after 10 conventional washing processes.

For all samples, the extension of the absorption into the UVA wavelengths after infiltration was preserved also after washing and the values of their bandgaps were consequently maintained. Slight deviations between the spectra are due to the statistical deviation of the measurement of different fibers. From these spectra, we can see that the UV-blocking capacity of the fibers is preserved upon laundry.

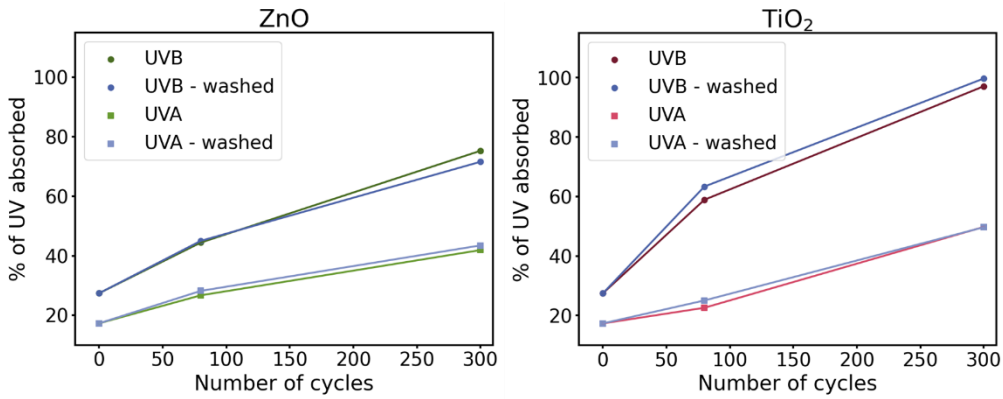

Figure 4.20. UV-blocking percentages in the UVA and UVB regions for jeans fibers infiltrated with 80 and 300 cycles of ZnO and TiO_2, before and after 10 conventional washing processes.

To analyze their effectiveness in preventing erythema more precisely, the UV-blocking percentages in the UVB and UVA regions before and after washing were calculated and are shown in **Figure 4.20**. The infiltrated fibers show very similar absorption percentages of both UVB and UVA radiation after being washed. The hybrid fabrics keep absorbing erythema-inducing UVR after washing and protecting skin from damage.

4.5.2. Resistance of the antibacterial properties

The bacteriostatic activity of the hybrid fabrics infiltrated with 80 cycles of ZnO and TiO_2 was evaluated against *S. aureus* and *E. coli* before and after being washed 10 times, with and without soap. The attachment and proliferation of both bacteria strains were evaluated as described in **Section 4.3.1,** using the corresponding pristine fabric as positive control. The results obtained are shown in **Figure 4.21**.

Both raw cotton and jeans infiltrated with ZnO maintained their antibacterial activity after being washed with water and with water and soap. Raw cotton infiltrated with TiO_2 originally presented a bacteriostatic activity of $R>2$ only against *S. aureus*, which was preserved after washing in both studied conditions. The only hybrid fabric that had its antibacterial activity affected by the laundering processes was jeans infiltrated with TiO_2. *S. aureus* could attach to the fabrics after being washed with water, but not after being washed with water and soap, while *E. coli* could attach after both laundering processes. The washing processes damaged the TiO_2 coating on the surface of the jeans and reduced its efficiency, either by removing inorganic material or by modifying its morphology. The results obtained for *S. aureus* can be explained by the surfactant behavior of the soap molecules, which can form a barrier reducing the interaction between the TiO_2 coating and water. This protection, however, is not enough to maintain the antibacterial activity against *E. coli*, which has a more resistant outer layer that is not sufficiently affected by the TiO_2 coating remaining after the washing processes.

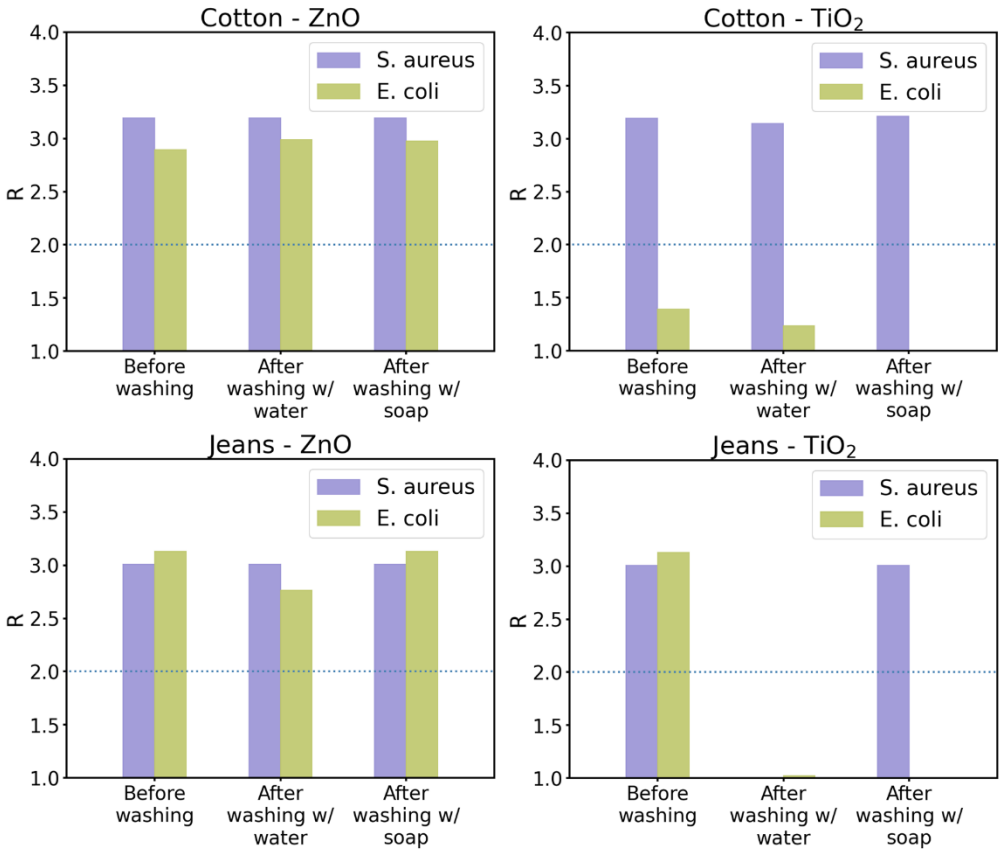

Figure 4.21. Antibacterial activity against *S. aureus* and *E. coli* of cotton and jeans fabrics treated with 80 infiltration cycles of ZnO and TiO_2 before and after 10 conventional washing processes with and without soap. The blue dotted line marks the R=2 threshold.

4.6. Conclusions

We have studied the functionalities induced by the treatment of cotton and jeans with ZnO and TiO_2 through Vapor Phase Infiltration, focusing on the properties of relevance for the textile industry. A summary of the functionalities achieved is given in **Table 4.1**.

To study the enhancement of the photoprotective function of the hybrid textiles against ultraviolet radiation, their UV-Visible absorption spectra were measured. The bandgaps and their dependence on the number of infiltration cycles were obtained, as well as the Ultraviolet Protection Factor and UVB and UVA blocking percentages. All samples presented an extension of the absorption into the UVA wavelengths, reaching the

characteristic bandgaps of bulk ZnO and TiO_2. The calculated UPF of the hybrids was higher for infiltration with TiO_2 than with ZnO. This difference came from the higher efficiency in blocking erythema-inducing radiation in the UVB region of jeans infiltrated with TiO_2.

Fabric		Cotton		Jeans	
Oxide		ZnO	TiO_2	ZnO	TiO_2
UV protection		-	-	✓	✓
Self-Cleaning	Photocatalysis	✓	-	-	-
	Hydrophobicity	-	-	✓	✓
Antibacterial activity	*S. aureus*	✓	✓	✓	✓
	E. coli	✓	✗	✓	✓
	C. striatum (Anti-odor)	✓	✓	✓	✓
Antifungal activity	Spore germination	✓	-	✓	-
	Hyphal growth	✗	-	✗	-
Flame retardancy		✓	✓	✓	✓
Resistance to laundering	UV protection	-	-	✓	✓
	S. aureus	✓	✓	✓	✗/✓
	E. coli	✓	-	✓	✗

Table 4.1. Summary of the studied functionalities. Functionalities achieved are marked with ✓, functionalities not achieved are marked with ✗ and functionalities not measured or already present in the pristine fabrics are marked with -.

To investigate the self-cleaning activity, its chemical and physical aspects were studied separately. The photocatalytic activity of raw cotton fabrics infiltrated with ZnO was studied through measurements of the photodegradation of rhodamine B under simulated solar light. The photodegradation reaction rate increased with the number of infiltration cycles and process temperature, reaching a maximum at 100°C. The hybrid fabrics preserved their photocatalytic activity and did not lose efficiency after repeated use. In order to study the hydrophobicity of the treated textiles, the water contact angle and water absorption capacity of infiltrated jeans were measured. After treatment, the fabrics became superhydrophobic, with contact angles between 120 and 130°. Liquid

drops could remain atop the surface without being absorbed for up to an hour. The water absorption coefficient was significantly reduced, especially during the first minutes of immersion. This change was independent of the metal oxide and the number of infiltration cycles.

The antimicrobial properties of the infiltrated fabrics were proven against bacteria and fungi. The bacteriostatic activity was tested against *Staphylococcus aureus* and *Escherichia coli*, model strains of GRAM+ and GRAM- bacteria, respectively. In the case of cotton, samples infiltrated with a minimum of 20 cycles of ZnO repelled *S. aureus* and *E. coli*. Infiltration with TiO_2 was not effective in hindering the attachment of *E. coli* and needed 40 cycles to repel *S. aureus*. In the case of jeans, the maximum possible antibacterial activity against both bacteria strains was obtained for all analyzed samples. The differences in antibacterial activity are attributed to the different surface roughness of the fabrics and the more resistant cell wall of GRAM- bacteria. Additional tests against *Corynebacterium striatum,* a bacteria responsible for body odor, were carried out obtaining the maximum possible antibacterial activity in each case studied. The antifungal activity of ZnO-infiltrated fabrics was analyzed by observing the inhibition capability of the textiles against polar extension of actively growing hyphae and spore germination of the model filamentous fungus *Aspergillus nidulans*. The studied hybrid fabrics showed partial antifungal activity, inhibiting spore germination of *A. nidulans* but not its hyphal growth.

Regarding the achieved fire resistance, hybrid textiles, infiltrated with both ZnO and TiO_2, showed a considerable flame-retardant performance. Compared to pristine fabrics, they exhibited slower ignition, shorter burning times, and a marked reduction in fire-induced damage to the textile structure. Additionally, smoke production during combustion was significantly suppressed, contributing to an overall safer fire behavior.

To ensure the durability of the hybrid fabrics prepared via VPI, the UV-blocking and antibacterial assessments were repeated after being washed using conventional laundering programs with and without soap. The extension of the absorption into the UVA wavelengths obtained with the infiltration was preserved after washing and the washed hybrid fabrics kept efficiently absorbing erythema-inducing UVR. Both raw cotton and

jeans infiltrated with ZnO maintained an optimal antibacterial activity, while the effectiveness of TiO_2 infiltration was dependent on the use of soap and the bacteria strain.

The combination of the measured properties confirms infiltration of metal oxides into cotton-based fabrics by VPI as a tool to achieve multiple functionalization. Properties with great relevance for the textile industry, including UV protection, self-cleaning activity, increased hydrophobicity, repellence of microbes and odors, and flame retardancy, have been incorporated into the fabrics with just one treatment. The durability of the obtained properties has been tested after washing of the fabrics with water and soap. Functionalities depending on surface modification can be affected by washing, while those depending on the infiltrated material are retained.

5

Human perception of the multifunctional organic-inorganic hybrid textiles

In this part of the thesis, cotton-based fabrics have been infiltrated with metal oxides using VPI with the objective of achieving multiple functionalization. Properties with great relevance for the textile industry, including increased hydrophobicity, repellence of microbes and odors, self-cleaning activity, and UV-blocking, have been incorporated into the fabrics with a single treatment. The obtained properties were retained even after washing of the fabrics with water and soap.

This chapter evaluates the human visual and tactile perception of the fabric after functionalization with varying amounts of metal oxide infiltration. The goal is to identify the threshold of a perceived difference.

For analyzing the visual perception, color measurements were taken before and after the treatment of the fabrics and the differences were quantified using the CIELAB color space.

For analyzing the tactile perception, fingertip friction and movement measurements were combined with a perceptional task with volunteer participants identifying which sample feels different. The later task is generally known as *Odd Sample Out* methodology. This work was carried out during a research stay at the Interactive Surfaces research group of the Leibniz Institute for New Materials (INM) in Saarbrücken, Germany, under the supervision of Prof. Dr. Roland Bennewitz from June to September 2024.

The combination of both studies allows us to identify the optimal amount of each metal oxide infiltrated needed to obtain new functionalities while preserving the appearance and feel of the original textiles.

5.1. Visual perception

In most textile applications, visual appearance is essential. Consequently, maintaining the original aesthetics of infiltrated textiles is important when looking for functional, ready-to-use materials. Humans are highly sensitive to color differences so, considering VPI the last step of the manufacturing process, we must ensure that the color of the textiles remains unchanged after infiltration, as any alteration can be easily noticed and understood as a defect. Additionally, unexpected color changes can suggest damaging treatment processes, indicating degradation of fibers or dyes. By preserving the original color, the integrity of the textile is better guaranteed.

5.1.1. Methodology

5.1.1.1. The CIELAB color space

Colors are an objective physical property of matter; however, they become subjective when perceived and described by the human brain. Precise communication of the colors that we see and want to reproduce requires a numerical system with standardized color definition and universal measurement protocols.

Scientists have defined hue, saturation, and lightness as the three basic dimensions of color characterization [93].

- *Hue* is what we perceive as the color itself and is determined by the dominant wavelength of light reflected or emitted by an object (i.e.: red, green, blue, yellow). Pure white, neutral gray, and black do not possess hue.
- *Saturation* describes the purity or intensity of a color in relation to neutral gray. When the color (hue) becomes more saturated, it becomes less gray.

- *Lightness* describes the relative brightness of a color. It is an achromatic value, meaning that the associated value gives only information about how light or dark the color is and not its hue.

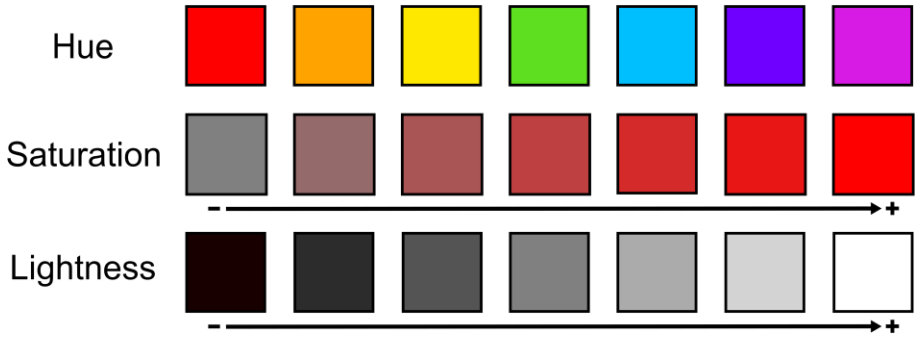

Figure 5.1. Graphical representation of the three basic dimensions of color.

When these properties are assigned numeric values, they become coordinates that represent all colors in a theoretical 3D sphere or color space. One axis characterizes lightness separately, while the other two form a chromatic plane where numeric coordinates define the specific color.

The International Commission on Illumination (*CIE: Commission Internationale d'Eclairage*) proposes various mathematical models to numerically describe all color visible to the human eye in an absolute and unambiguous way. The CIELAB system, published in 1976, has become the universally accepted reference system for quantifying and communicating color. It is based on the *Opponent Process Theory*, which states that the brain perceives color stimuli through three independent receptor types which have opposing pairs: white and black, blue, and yellow, and red and green. Following this theory, the CIELAB color system is a three-dimensional model with the following axes:

- The chromatic axis a^*, which ranges from green ($-a^*$) to red ($+a^*$).
- The chromatic axis b^*, which ranges from blue ($-b^*$) to yellow ($+b^*$).
- The lightness axis L^*, which ranges from pure black ($L^* = 0$) to white ($L^* = 100$).

The point at which the a^* and b^* axes cross at the L^* value of 50 is neutral gray.

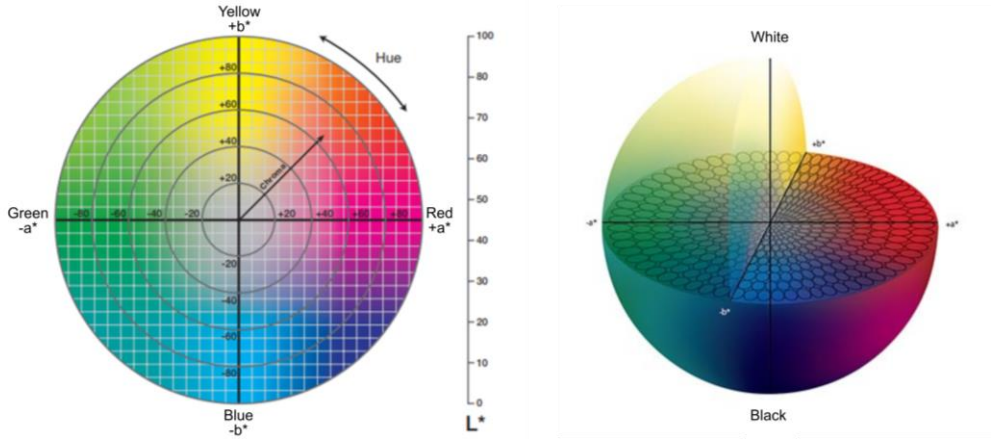

Figure 5.2. 2D and 3D representations of the CIELAB color space. Adapted from [94] and [95].

In practice, it is rarely possible to reproduce the color of a product with complete fidelity. Slight differences in color exist even when the human eye cannot perceive them. Using these coordinates in the color space, color differences can be computed as the relative distance between two points. This difference is typically expressed as:

$$\Delta E^*_{ab} = \sqrt{\Delta L^{*2} + \Delta a^{*2} + \Delta b^{*2}} \tag{5.1}$$

However, the human eye does not perceive differences in hue, saturation, and luminosity equally; variations in hue are the first to be detected, followed by variations in saturation and lastly, variations in luminosity. This means that a color difference of a fixed value ΔE^*_{ab} can be perceived differently depending on the zone of the color space where it is found.

To correlate with the non-uniformities of human perception, different formulas to calculate color differences have been proposed [96], [97]: The CMC formula includes the empirically evaluated correction factors S_L, S_C and S_H, hyperbolic functions that weight each contribution depending on the luminosity (L^*), saturation (chroma, C^*) and hue (H^*) of the colors:

$$C^* = \sqrt{a^{*2} + b^{*2}} \tag{5.2}$$

$$H^* = \tan^{-1}\frac{b^*}{a^*} \tag{5.3}$$

$$\Delta E_{CMC} = \sqrt{\left(\frac{\Delta L^*}{l\,S_L}\right)^2 + \left(\frac{\Delta C^*}{c\,S_C}\right)^2 + \left(\frac{\Delta H^*}{S_H}\right)^2} \tag{5.4}$$

Where the parameters l and c can be chosen by the user. In the textile industry, the *CMC (2:1)* combination is widely used, setting $l = 2$ and $c = 1$, which reduces the impact of the changes in luminosity.

Following a similar approach, the CIE has proposed various modifications to the original formula, with CIE2000 (**Equation 5.5**) being the most recent and precise one. This formula includes a mixt term, called the rotational term, which considers that the human-perceived saturation of a color can be hue-dependent.

$$\Delta E_{00} = \sqrt{\left(\frac{\Delta L^*}{k_L\,S_L}\right)^2 + \left(\frac{\Delta C^*}{k_C\,S_C}\right)^2 + \left(\frac{\Delta H^*}{k_H\,S_H}\right)^2 + R_T\left(\frac{\Delta C^*}{k_C\,S_C}\right)\left(\frac{\Delta H^*}{k_H\,S_H}\right)} \tag{5.5}$$

The thresholds of appreciation and acceptability are not fixed and must always be confirmed by visual perception. As a general rule, a color difference between 3 and 5 is taken as the upper limit for acceptable repeatability and consistency, although color differences might be detected under closer inspection.

5.1.1.2. Equipment and measurement conditions

Color measurements were done using a Konica Minolta CM-17d spectrophotometer in reflectance mode with a wavelength range from 400 to 700 nm. Standard settings for color evaluation were chosen, mimicking how the human eye perceives color: The measurement geometry for diffuse and directional illumination was set to 8º and the aperture size was set to SAV (Small Area View, 3 mm), meaning that the device measured a circular area of 3 mm in diameter. Both the included (SCI) and excluded (SCE) specular components were measured. SCI includes both specular and diffuse reflections, giving an accurate measurement of color independent of the surface finish, while SCE excludes specular reflections, giving a more accurate measurement of the color appearance of the textured samples under normal lighting conditions [98].

5.1.1.3. Sample set

Samples of 5x5 cm^2 of raw woven cotton and jeans were measured before and after infiltration to analyze how the process affects their visual appearance. Each sample was measured in triplicate. Both types of fabrics were infiltrated with zinc oxide (ZnO) and titanium dioxide (TiO_2) following the standardized conditions in this thesis. Samples were processed in a PLAY reactor from CTECHnano, suspended in the chamber in a way that allows both sides of the fabric to be exposed to the precursors. DEZ was used as the zinc source and $TiCl_4$ as the titanium source, both combined with purified water (H_2O) as the counter precursor. All precursors were kept at room temperature. The processing temperature was 60°C for ZnO and 100°C for TiO_2 infiltration. N_2 was used as a carrier gas with a constant flow of 20 sccm. Each VPI half-cycle consisted of 40 ms of precursor dosing, 40 s of exposure and 60 s of purge. The cycle was repeated 5, 20, 40, 80 and 300 times for each metal oxide and fabric type. Samples are labeled *C* or *J* for cotton or jeans respectively, followed by the metal of the oxide infiltrated (*Ti* or *Zn*) and the corresponding number of cycles. For example, samples of raw cotton fabric treated with 20 cycles of TiO_2 will be labeled as *CTi20*.

5.1.2. Results and discussion

The collected CIELAB color space data can be converted into RGB format to visualize each color. **Figure 5.3** shows the measured colors for each type of fabric and treatment. It is important to note that untreated cotton fabrics present a range of natural color variations depending on the manufacturing of each batch. This is the reason for the deviation in color between the two 'Blank' samples. Consequently, the color variation analysis of each of the treated samples is done taking their color before treatment as a reference.

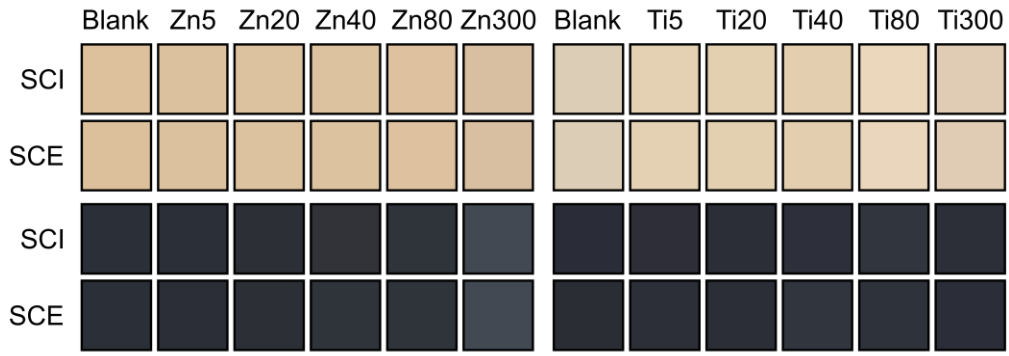

Figure 5.3. Representation of the measured RGB colors for the included (SCI) and excluded (SCE) specular components for each fabric and treatment.

To analyze the changes induced by the infiltration, each of the CIELAB color space coordinates were analyzed separately. **Figure 5.4** shows how each of them varies with the infiltration of ZnO into cotton or jeans.

In both fabrics, a^* decreases with infiltration, meaning that the color of the treated samples shifts more towards green compared to the untreated ones. In cotton, this shift is almost constant and never larger than 1. In jeans, it increases with the number of cycles until it reaches a value of -1.4 at 300 cycles. In both cases the impact of this shift in the perceived color can be considered neglectable.

b^* shows different behavior in either fabric. In the treated cotton fabrics, the color shifts towards blue. However, this change is below the unit for the lower number of cycles and only becomes significant when increasing the number of cycles to 300, where it reaches a value of -4.9. In the case of jeans, the shift in color is towards yellow. The maximum change is seen at 40 cycles with an increase of 2.3, but the original value of b^* is restored after 300 cycles. The reason behind this change was not further investigated due to the complex nature of the substrate.

L^* remains constant in the case of cotton and never deviates more than a unit from the original lightness of the fabric. In the case of jeans, however, this is the coordinate that has the most considerable variation. It increases to 2 for 40 and 80 cycles and to almost 12 for 300 cycles, meaning that infiltration makes the color of the treated samples noticeably lighter than it originally was.

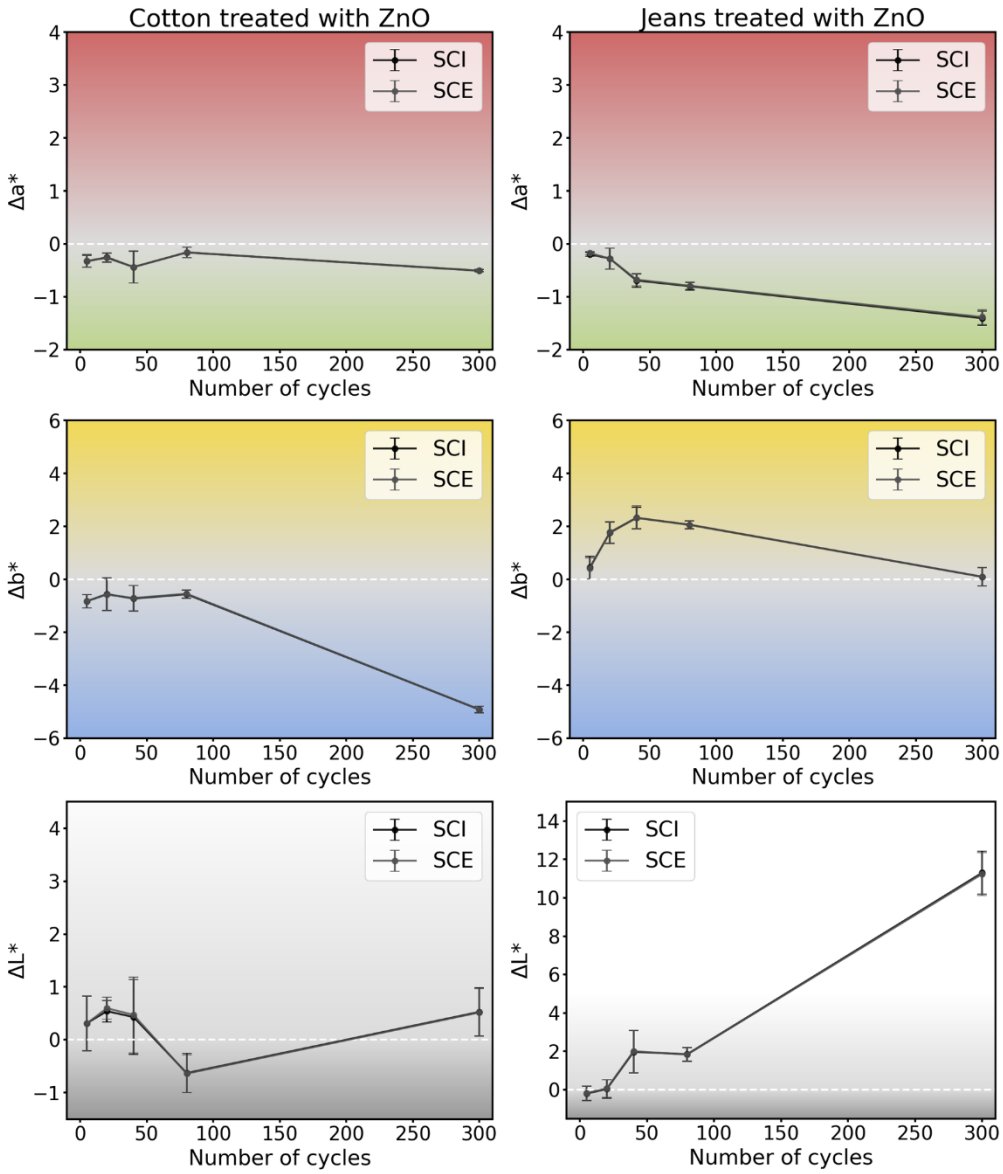

Figure 5.4. Variation of the CIELAB color space coordinates as a function of the number of ZnO infiltration cycles in cotton and jeans.

To commensurate the impact of the changes in the color space coordinates on the visual perception of the fabrics, we calculate the absolute color differences using the CIE76, the CMC and the CIE2000 standards. These differences are shown in **Figure 5.5**.

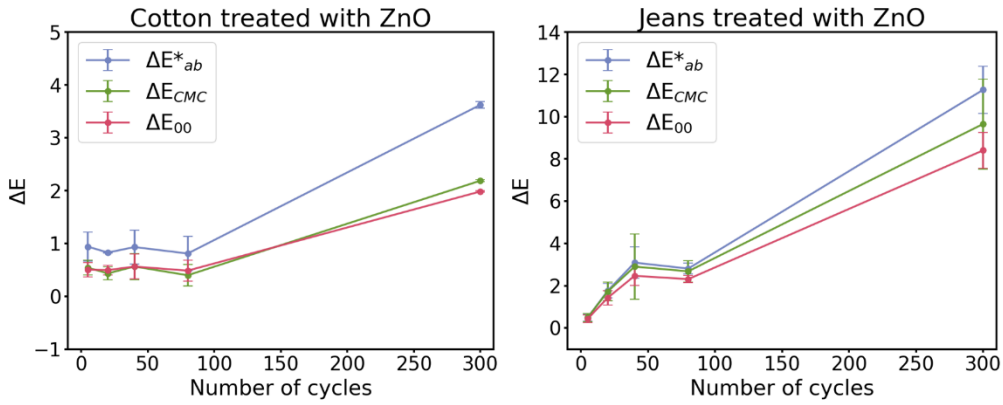

Figure 5.5. Color differences calculated following the CIE76 (ΔE^*_{ab}), CMC and CIE2000 standards, as a function of the number of ZnO infiltration cycles in cotton and jeans.

In the case of cotton, the difference between the colors of the untreated and treated samples is around 1 for cycle numbers between 5 and 80, which means that the colors are undistinguishable under visual inspection according to the three standards used. When the number of cycles is increased to 300, the color difference increases. It stays below 2 according to the CMC and CIE2000 standards, but it reaches a value of 3.5 in CIE76. We can consider the color of this sample to be distinguishable for a trained eye or under close inspection of the fabric, but still within acceptable consistency thresholds.

In the case of jeans, the distances between colors are greater. They only stay below the unit for 5 cycles, making it the only undistinguishable sample under visual perception. Between 20 and 80 cycles, they have values of 2 to 3.5, meaning that the colors of these samples are distinguishable under closer inspection, but the color deviations are acceptable. Samples infiltrated with 300 cycles have color differences exceeding 7 following the three standards. These samples are easily distinguishable from the untreated ones, and their color is perceived as a completely different one. Indeed, these conclusions are supported by visual inspection of the samples as represented in **Figure 5.3**.

In the following, we analyze the color shifts caused by the infiltration of TiO_2 in cotton and jeans. The variations of each of the CIELAB color space coordinates are shown in **Figure 5.6**.

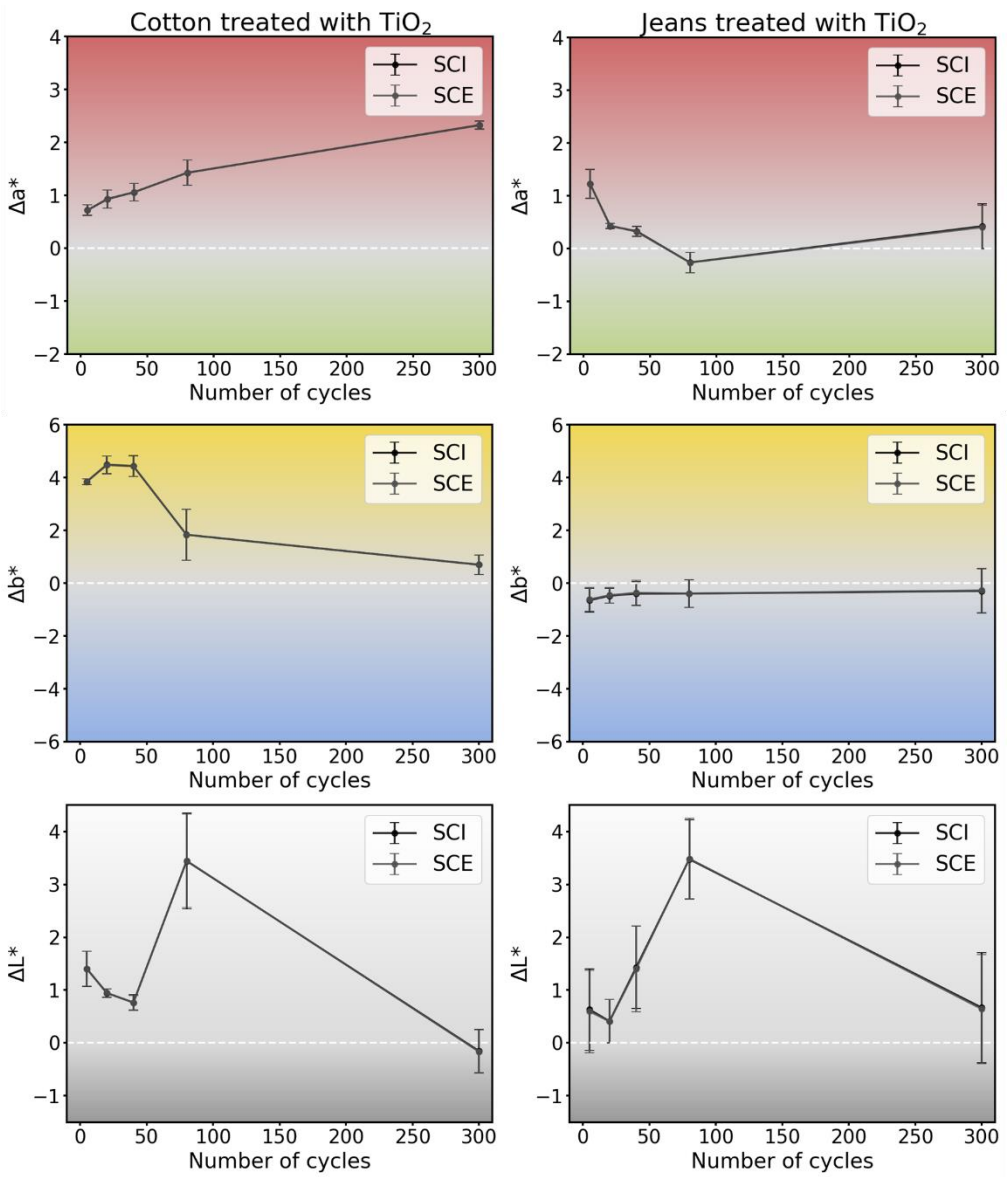

Figure 5.6. Variation of the CIELAB color space coordinates as a function of the number of TiO_2 infiltration cycles in cotton and jeans.

In the case of cotton, *a** steadily increases with infiltration, meaning that the treated sample becomes redder than the untreated. This shift reaches a maximum of 2 for 300 infiltration cycles. In jeans, samples treated with 5, 20, 40 and 300 cycles are redder than the untreated ones, while the sample treated with 80 cycles is slightly greener. However, the total color

shift is always smaller than a unit and its impact on the perceived color can be considered neglectable.

*b** significantly increases and the color shifts towards yellow for the lower number of TiO_2 infiltration cycles into cotton. This shift is lower for 80 cycles and disappears, reverting to the original value of *b** for 300 cycles. In the case of jeans, the color shifts towards blue. However, the change in the coordinate remains constant with the number of cycles and is never greater than the unit, so we can conclude that there is no perceivable change in the blue or yellow hue of the treated jeans samples.

The variations in *L** follow the same tendencies in both cotton and jeans. The value of *L** increases and reaches a maximum variation of 3.5 for 80 infiltration cycles meaning that infiltration makes the color of the treated samples lighter than it originally was. However, the original lightness of the fabric is again restored after 300 infiltration cycles.

The absolute color differences according to the CIE76, CMC and CIE2000 standards, measuring the impact of the changes in the color on the visual perception of the fabrics, are shown in **Figure 5.7**.

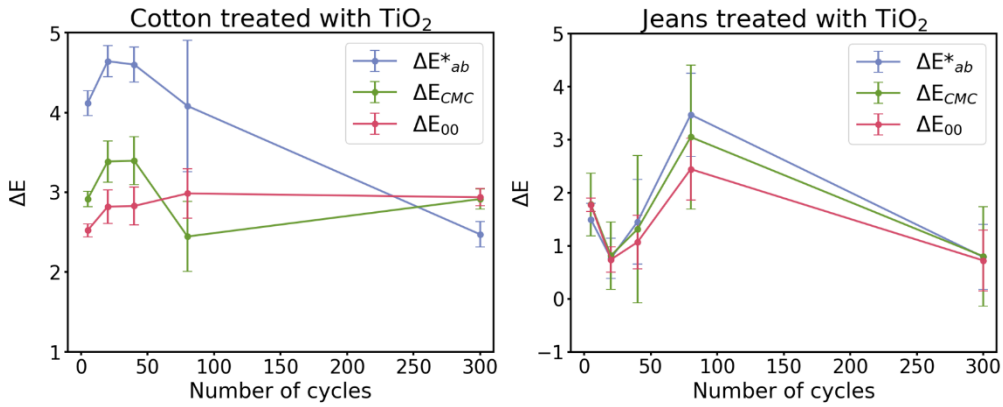

Figure 5.7. Color differences calculated following the CIE76 (ΔE^*_{ab}), CMC and CIE2000 standards as a function of the number of TiO_2 infiltration cycles in cotton and jeans.

In the case of cotton, the distance between the color of the untreated samples and the treated ones is always less than 5. The color differences are larger for the lower number of cycles when using the CIE76 standard. In the case of the more precise CMC and CIE2000 standards, the color differences are more consistent around the value of 3. Therefore, the color

of these samples is distinguishable for a trained eye or under close inspection of the fabric, but it is still acceptable within the repeatability and consistency thresholds.

In the case of jeans, all three standards follow the same trend, showing the maximum difference between colors at 80 cycles. This change is due to the increase in lightness shown in the coordinate analysis. However, in all cases the distance between the color of the untreated and the treated samples is always below 3.5, meaning that the color of these samples is distinguishable for a trained eye or under close inspection of the fabric, but acceptable within the repeatability and consistency thresholds.

5.2. Tactile perception

Our skin is always in contact with textiles. Whether through the clothes we wear, the furniture and vehicle seats we sit on, or the sheets and bandages used in hospitals, we are always touching and experiencing fabrics, making their tactile properties a key factor in comfort and functionality. Consequently, maintaining the tactile feel of textiles after treatment is essential. This study aims to understand whether humans can perceive functionalized fabric through touch and, if so, to determine how they detect functionalization and the minimum detectable amount of metal oxide.

5.2.1. Methodology

5.2.1.1. Odd Sample Out methodology

The Odd Sample Out, Triangular or Triangle test is a sensory evaluation methodology used to determine whether perceptible differences between two samples exist. The method is applicable both if differences exist in a single sensory attribute or in several attributes. This type of task is used in most fast-moving consumer good companies as standard test method as it is useful to evaluate overall differences and determine the effect of a change in ingredients, packaging, processing, handling, or storage conditions [99].

In the task, participants are simultaneously presented with three samples, two of which are identical, and one is different. The participants are asked to identify the different sample. This is a "forced choice" method, where participants are required to respond even if they feel no difference. However, they can indicate a potentially random decision in a complementary scoresheet [100]. Samples are presented in a random order, following one of the six possible sequences:

AAB ABA BAA

BBA BAB ABB

Where A represents an original sample, and B represents a modified sample.

Here, the probability of correctly identifying the sample by random choice is of one third. The participants are allowed to reassess the samples as many times as necessary before making their decision. Repetition of choices by the same participant should be avoided whenever possible.

The optimum number of participants depends on the sensitivity required for the test, as stated in Table A.3. of ISO 4120:2004 [100]. This is determined by the following parameters:

- *Alpha Risk (α Risk):* risk of concluding that perceptible differences exist between two samples when they are the same, or risk of a false positive.
- *Beta Risk (β Risk):* risk of concluding that no perceptible differences exist between two samples when they are different, or risk of a false negative.
- *Maximum allowable proportion of distinguishers (P_d),* maximum number of participants able to perceive a difference between samples tolerated.

The statistical test used for the analysis of the results is a one-tailed binomial test and the interpretation is based on the minimum number of correct answers required for significance [101]. Standards are fixed for studies in which the objective is to prove that a perceptible difference exists (Table A.1. of ISO 4120:2004) and when the objective is to prove that there are no perceptible differences (Table A.2.). In this analysis alone, no

magnitude or direction of the difference should be concluded from the significance level or the probability.

5.2.1.2. Sample set

Both raw cotton and commercial jeans fabrics were infiltrated with ZnO and TiO_2. Samples were processed in a PLAY reactor from CTECHnano, suspended in the chamber in a way that allows both sides of the fabric to be exposed to the precursors. DEZ was used as the zinc source and $TiCl_4$ as the titanium source, both combined with purified water (H_2O) as the counter precursor. All precursors were kept at room temperature. The processing temperature was set to 60°C for ZnO and 100°C for TiO_2 infiltration. Three samples were treated simultaneously in each process. For this study, the samples were cut to a size of 6x6 cm^2. Since the surface area of the samples was modified, the standardized conditions in this thesis were adapted to ensure that they were fully and homogeneously treated, and both the carrier gas flow and the precursor dose were increased. N_2 was used as a carrier gas with a constant flow of 40 sccm. Each VPI half-cycle consisted of 200 ms of precursor dosing, 40 s of exposure and 60 s of purge. Cycles were repeated 5, 10, 20, 40, 80, 100 and 300 times for each metal oxide and fabric type. This gives 14 different treatments for each fabric type, 28 in total. Each treatment will only be compared to the corresponding pristine fabric.

Samples are labeled with *C* or *J* for cotton or jeans, respectively, followed by the metal of the infiltrated oxide (*Ti* or *Zn*) and the corresponding number of cycles. For example, samples of raw cotton fabric treated with 20 cycles of TiO_2 will be labeled as *CTi20*.

5.2.1.3. Odd Sample Out study

To investigate the perception of the infiltrated fabrics by touch, we presented sample triplets to the participants, who were asked to explore the samples in a circular motion of their dominant index fingertip. In each triplet of samples, one or two samples were treated by infiltration and two or one samples were kept pristine. The participants were allowed to explore the samples for as long as they wanted and to change between them as many times as needed. Afterwards the participants had to answer the question:

"Which sample feels different from the others?"

The participants were forced to choose one sample even if they felt no differences. However, they were asked to state if the choice was random in a complementary task sheet.

During the tactile exploration, the applied normal and friction forces were measured with a 3-axis force sensor (K3D120 with GSV-8 amplifier, ME-Messysteme, Germany). The position and velocity of the finger on the sample were simultaneously measured with an infrared camera system (V120: Trio, OptiTrack), synchronized with the force plate. To reproduce the feel of fabric on skin, the textile samples were mounted on top of 5x5 cm^2 metallic sample holders filled with PDMS of 0-30 in the Shore Hardness scale, mimicking the stiffness of thigh skin, and secured by metal frames. During the experiment, participants were asked to wear noise canceling headphones to avoid the influence of sound in their decisions. A semi-opaque screen was placed between the participants and the samples to avoid the influence of slight changes in appearance on their decision.

Before starting the experiment, participants were asked to wash their hands. 10 minutes after, the fingertip skin moisture and viscoelasticity were measured using a corneometer and a cutometer, respectively (CM825 and MPA580, Courage & Khazaka). The measurement of skin moisture was repeated after they touched all the samples in the study.

Each participant was presented with 28 sample triplets divided into two sets, one with 14 triplets of raw cotton and one with 14 triplets of jeans. Each of these triplets had one or two untreated pieces of fabric and two or one of each of the treatments in the sample set. The treated samples in each triplet were always identical, never comparing different treatments. The number of treated/untreated samples, the order of the triplets and the order of the samples inside the triplets was randomized. After each participant, the fabrics were removed from the holders and randomly rearranged to avoid any possible differences induces by the PDMS in the holders.

The experiment was conducted according to the local institutional ethical guidelines and the Declaration of Helsinki, [102] except for the preregistration requirement. Before any measurement, all participants

were asked to sign a consent agreement to participate in the study and to complete a questionnaire about age, gender, dominant hand, usage of cream and experience in haptic studies. After the measurements, they were asked to complete another questionnaire about the difficulty of the task and the criteria used to identify the different samples.

5.2.1.4. Participants

In order to run this Odd Sample Out test with statistically significant risk values, a group of 30 participants, 15 male and 15 female, was invited to the study [103]. The only inclusion criterion used to select the participants was the absence of sensory or movement impairments that could affect their perception when touching surfaces. The participants had ages ranging from 21 to 39 years with an average age of 27.83 and a standard deviation of 3.81. Of the participants, 28 (93.33%) identified their right hand as the dominant one, 2 (6.67%) chose their left hand. 19 participants participated in a haptic study before while for 11 it was the first time; this experience does not have a significant effect on the number of right answers or on the perceived difficulty of the task. Participants took an average of 34.6 minutes to complete the task and identified the different sample correctly in a median of 13 sets out of 28.

5.2.1.5. Bending stiffness measurements

The bending stiffness of the fabrics was measured using samples cut to a size of 15x15 cm^2. Since the surface area of the samples was modified, the conditions were again adapted to ensure that they were fully and homogeneously treated. N_2 was used as a carrier gas with a constant flow of 40 sccm. For the infiltration of TiO_2 in both cotton and jeans, each VPI half-cycle consisted of 300 ms of precursor dosing, 40 s of exposure and 90 s of purge. For the infiltration of ZnO in cotton, each VPI half-cycle consisted of 700 ms of precursor dosing, 40 s of exposure and 60 s of purge. For the infiltration of ZnO into jeans, the precursor dose was increased to 1 s. All other process parameters were maintained. Cycles were repeated 5, 10, 20, 40, 80, 100 and 300 times for each metal oxide and fabric type, reproducing the samples used in the Odd Sample Out study.

Each sample was placed between two aluminum plates of 15x15 cm^2, leaving 7 cm of fabric hanging, and photographed with a camera leveled at

the same height. Each sample was placed and photographed in two positions, following the two directions marked by the weaving of the textiles, as shown in **Figure 5.8**.

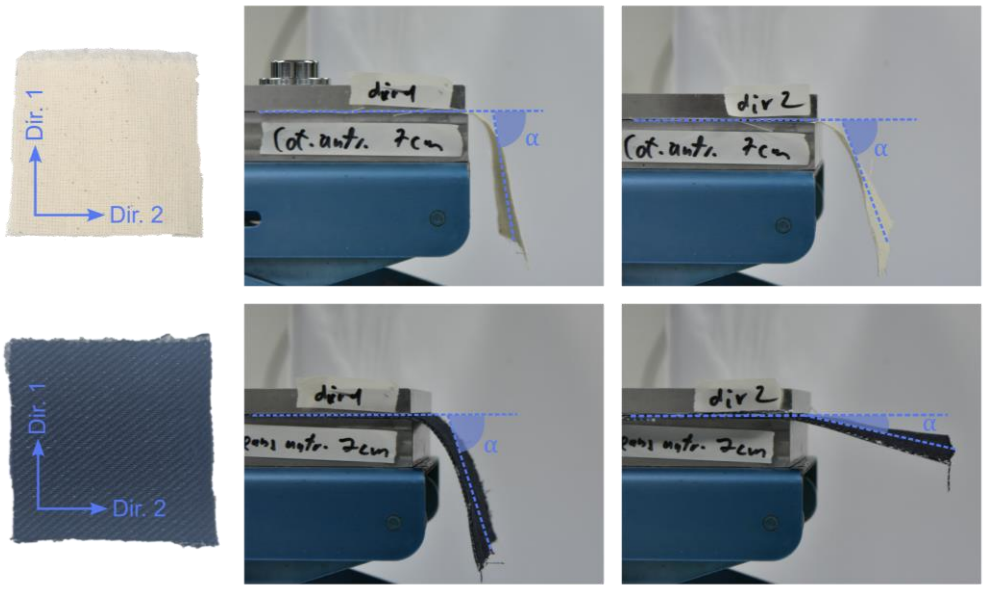

Figure 5.8. Schematics and set-up for the self-deflection angle measurements following the two weaving directions measured for cotton and jeans.

The self-deflection angle α, formed between the plane between the plates and the surface of the sample, was measured using the *ImageJ* software. The self-weight deflection of a soft, thin material is directly proportional to its bending stiffness [104].

5.2.2. Data analysis, results, and discussion

The collected data from finger motion capture and applied forces is combined and analyzed to obtain the coefficient of friction (COF), the dependence of friction on skin moisture, the success rate at identifying the different sample and its dependence on the characteristics of each sample.

5.2.2.1. Coefficient of friction as a function of skin moisture

Since the skin moisture of the finger pad can affect the perception of the sample by the participant, we analyzed its effect of the moisture on the COF.

The COF at each time stamp is obtained from force measurements applying **Equation 5.6**. The median value per sample and participant is then taken as the measured coefficient of friction.

$$COF(t) = \frac{\sqrt{F_x(t)^2 + F_y(t)^2}}{F_z(t)} \tag{5.6}$$

We found a correlation between finger pad moisture and COF best fitting to a linear regression with $r^2 = 0.48$ for all samples, $r^2 = 0.52$ for jeans and $r^2 = 0.49$ for cotton, as shown in **Figure 5.9**. As expected, the dispersion in the COFs is higher for higher values of skin moisture, due to changes in the mechanical properties and/or surface topography of human skin, leading to skin softening and increased real contact area and adhesion [105]. The COFs measured for the participant with the lowest moisture range from 0.24 to 0.38, in the case of the participant with the highest moisture this range is over 8 times wider, from 0.48 to 1.61.

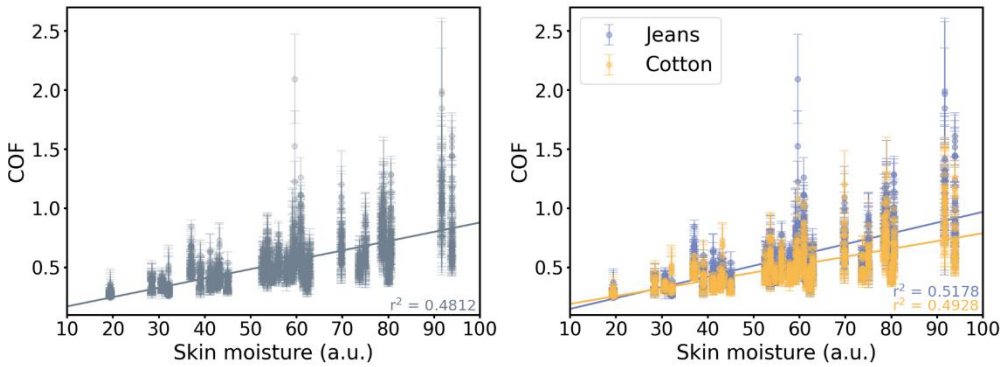

Figure 5.9. Scatter plots and linear regressions of the COFs as a function of skin moisture for all samples, and jeans and cotton samples separately.

As previously discussed, infiltration of the fabrics modifies their hydrophobicity. We found no clear tendencies showing a dependence of this relation on the treatment of the fabrics. The corresponding plots are shown in **Figure 5.10**. Since the treatments do not affect the general trends, for the following analysis of results the COFs are normalized by division by the median COF of each participant, giving equal weight to each of the samples touched. In this way we eliminate the dependence on skin moisture of the absolute values, making it possible to compare the measured COFs of different participants.

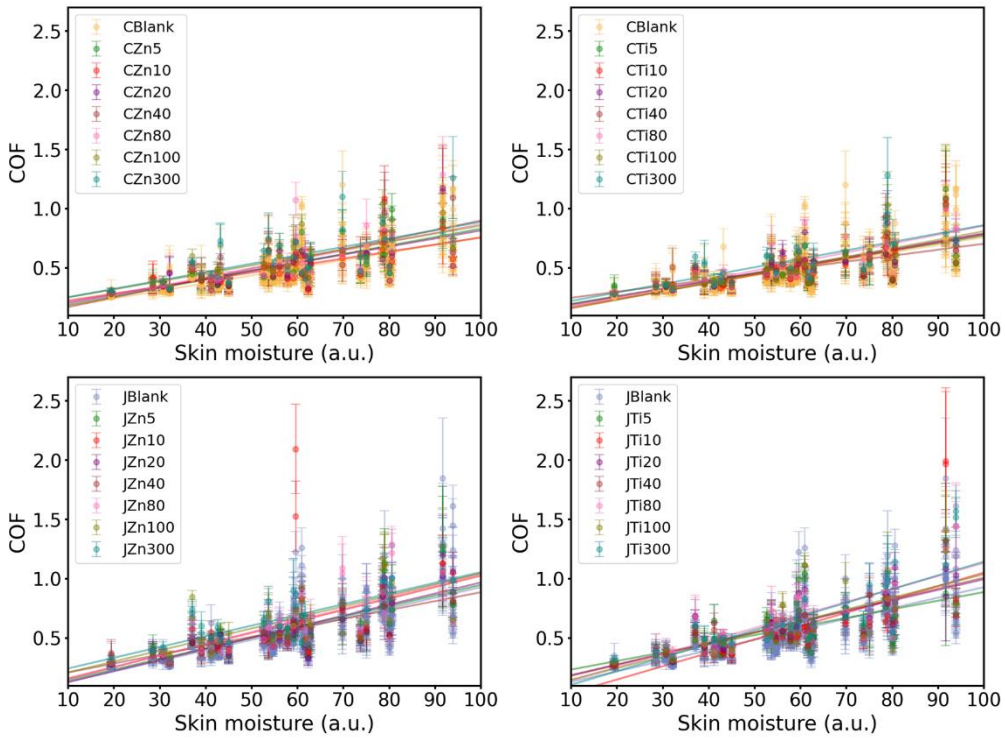

Figure 5.10. Scatter plots and linear regressions of the COF as a function of skin moisture for each treatment.

5.2.2.2. Coefficient of friction as a function of fabric and treatment

We start by comparing the COFs for the two different types of fabric by running a two samples t-test setting $\alpha = 0.05$. This was done separately for each participant with the absolute values of the coefficients of friction, and for all participants together using the normalized ones. When comparing individually, we found a significant difference for 27 of the 30 participants. Coincidentally, the participants for which no significant difference was found had a below average skin moisture. In the t-test for all participants, a significant difference was found *(p = 0.0000, t-stat = -17.6656)*. As shown in **Figure 5.11**, the coefficients of friction of cotton are significantly lower than those of jeans, both with and without treatment.

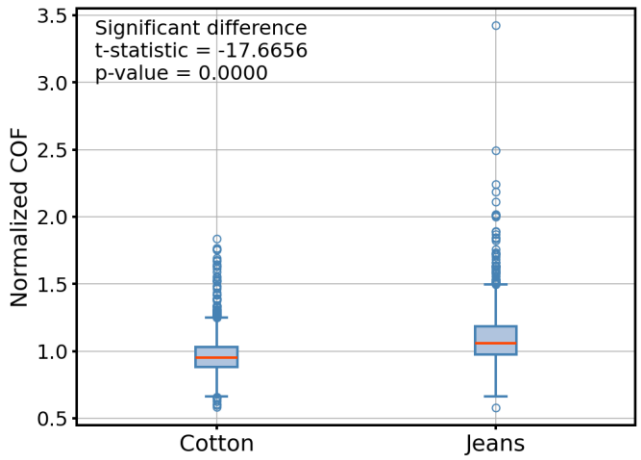

Figure 5.11. Boxplot showing the t-test comparing the normalized coefficients of friction of cotton and jeans measured for the 30 participants.

Therefore, to precisely study the effect of the infiltration on the COF, the values obtained for cotton and jeans are normalized separately per participant, meaning that the COFs of cotton samples are normalized by division by the median COF of only the cotton samples for each participant and not the median COF of all samples, and likewise for the jeans samples. The dependence of the median coefficient of friction on the number of infiltration cycles for each oxide is shown in **Figure 5.12**.

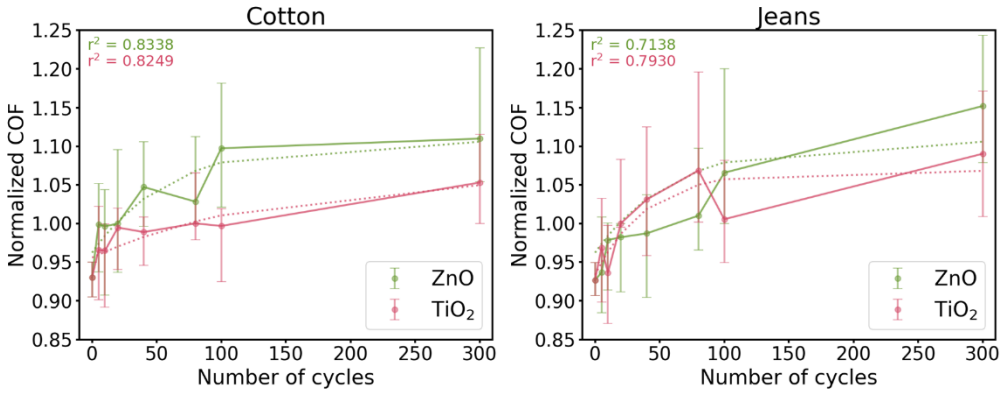

Figure 5.12. Evolution of the normalized COF as a function of the number of cycles of each metal oxide treatment for cotton and jeans, fitted to an exponential function. Error bars correspond to the 25 and 75 percentiles.

The COF generally increases with the number of infiltration cycles, proportional to the amount of metal oxide infiltrated into the fabric. This tendency is best fitting to an exponential function, since an eventual

saturation of the COF is expected. The increase in the COF is 5% higher in the case of jeans than in the case of cotton. Looking at the samples infiltrated with 300 cycles, in the case of cotton the increase is 13% for TiO_2 and 19% for ZnO, while for jeans the increase is of 18% for TiO_2 and 24% for ZnO. In both fabrics, the increase in COF is 6% higher for ZnO than for TiO_2. This difference is explained by the lower reactivity of $TiCl_4$ compared to DEZ, which also reflects on the different growth rates of the equivalent ALD processes. Therefore, for an equal number of cycles of both treatments, the amount of ZnO infiltrated is greater than the amount of TiO_2. The value of the COF for the infiltration with 100 cycles of TiO_2 is lower than expected. There is a drop from 80 to 100 cycles for both textiles, more pronounced in the case of jeans.

To determine whether the changes found in the COF are perceptible, we analyzed the choices of the participants during the Odd Sample Out study. If the probability of correctly identifying the odd or different sample is higher from what would be expected from a random choice, then the treated samples can be distinguished from the untreated ones by touching them. It is important to note that no magnitude of the difference between samples should be concluded from these probabilities.

The percentage of participants who have correctly identified the different sample is plotted as a function of the number of cycles for each sample and treatment in **Figure 5.13**. The number of cycles is taken as a logarithm for clarity. In general, samples treated with a lower number of cycles have a lower probability of being correctly identified than those treated with a larger number of cycles, which is expected from the increase of the COF. Still, most samples have a probability above chance of being correctly identified, showing that participants can detect the treated samples and are not randomly selecting them. The cotton sample infiltrated with 100 cycles of TiO_2 shows again an anomality, with a probability below chance. The same treatment on jeans is also detected less often than what is expected from the general tendency.

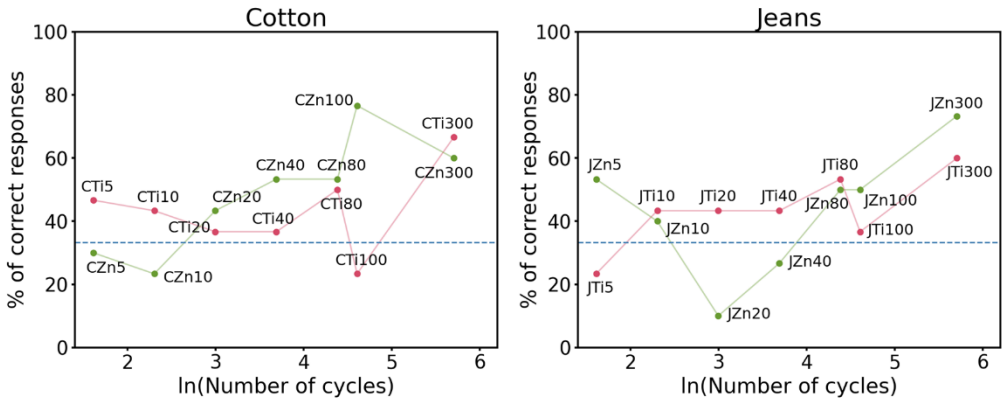

Figure 5.13. Percentage of participants that correctly identified the odd sample as a function of the logarithm of the number of cycles of each treatment for cotton and jeans. The blue dashed line represents the probability of correctly identifying the odd sample by chance.

Certain samples treated with a lower number of cycles may have a higher COF than those treated with a higher number of cycles, which is what influences the perception of participants when touching and ultimately affects the probability of correctly identifying the odd samples. To study this influence, we now correlate the percentage of participants that have correctly identified the odd sample with the COF for each sample and treatment.

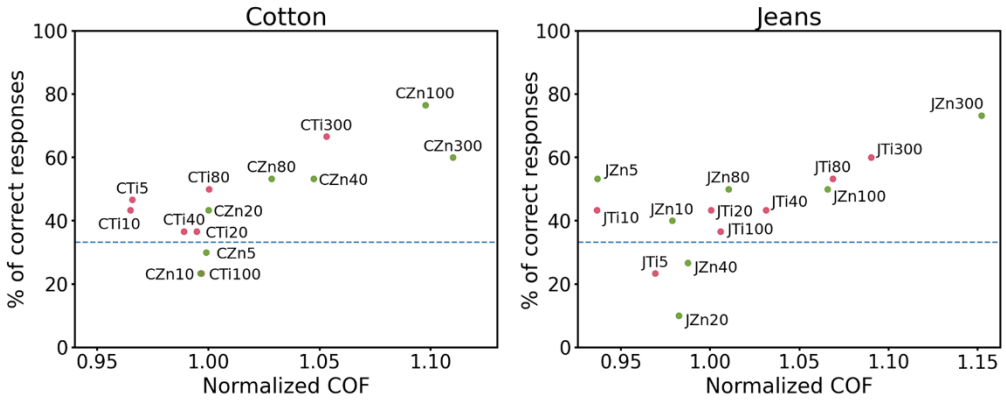

Figure 5.14. Percentage of participants that correctly identified the odd sample as a function of the normalized coefficient of friction of each treatment for cotton and jeans. The blue dashed line represents the probability of correctly identifying the odd sample by chance.

As shown in **Figure 5.14**, there is a higher probability of participants identifying the odd sample as the COF increases and the difference

between the treated samples and the untreated textile becomes more perceptible.

5.2.2.3. Friction oddness

In the previous analysis of the data, a global evaluation of the COF as a function of the number of cycles was made. Nevertheless, one of the strengths of this experimental design is that the COF is recorded for each participant and each trial. This means that we have friction data recorded at the very moment when the identification of the odd sample is made, allowing us to focus on the actual differences felt in each trial and to better analyze the decisions of the participants.

We now analyze whether the COF of the odd sample is more different from each of the even samples than the difference between the COFs of the two even samples, to know how odd the COF of the odd sample actually is. The friction oddness is defined as **Equation 5.7** when the odd sample is treated and as **Equation 5.8** when the odd sample is untreated (blank).

$$Friction\ oddness = \mu_{odd} - \frac{\mu_{even,1} + \mu_{even,2}}{2} - \frac{3}{2}\left|\mu_{even,1} - \mu_{even,2}\right| \quad (5.7)$$

$$Friction\ oddness = \frac{\mu_{even,1} + \mu_{even,2}}{2} - \mu_{odd} - \frac{3}{2}\left|\mu_{even,1} - \mu_{even,2}\right| \quad (5.8)$$

To give the trials of different participants the same weight, the friction oddness is normalized by dividing it by the average coefficient of friction of the two even samples. In the ideal case of $\mu_{even,1} = \mu_{even,2}$ the friction oddness simplifies to:

$$Normalized\ friction\ oddness = \frac{\mu_{odd} - \mu_{even}}{\mu_{even}} \quad (5.9)$$

These formulas separate between three possible cases:

1. If the differences between the COFs of the odd sample and both of the even samples are larger than the difference between the two even samples, the friction oddness will be positive. In this case the odd sample is also odd with respect to friction.
2. If the difference between the COF of the odd sample and one of the even samples equals the one between the two even samples, the

friction oddness will be 0. In this case there is no odd sample with respect to friction.

3. If the difference between the COF of the odd sample and one of the even samples is smaller than the difference between the two even samples, the friction oddness will be negative. In this case one of the even samples is odd with respect to friction.

To determine whether the perceived friction of the samples is actually different from the untreated ones the mean normalized friction oddness of all trials is plotted as a function of the number of cycles of each treatment in **Figure 5.15**. Samples with a friction oddness below or very close to 0 should be undistinguishable from the original textile in terms of friction. In the case of infiltration with ZnO, the friction oddness becomes appreciable after 40 cycles of infiltration in cotton. For jeans, 100 cycles are needed to make the increase of friction of the sample noticeable. For the infiltration with TiO_2, samples only become significantly odd in terms of friction when infiltrated with 300 cycles, for both fabrics. In the case of jeans, it is worth noting that, although the median friction oddness of lower number of cycles (20, 40, 80) is positive, the error bars show that most participants were not able to perceive the difference in COF.

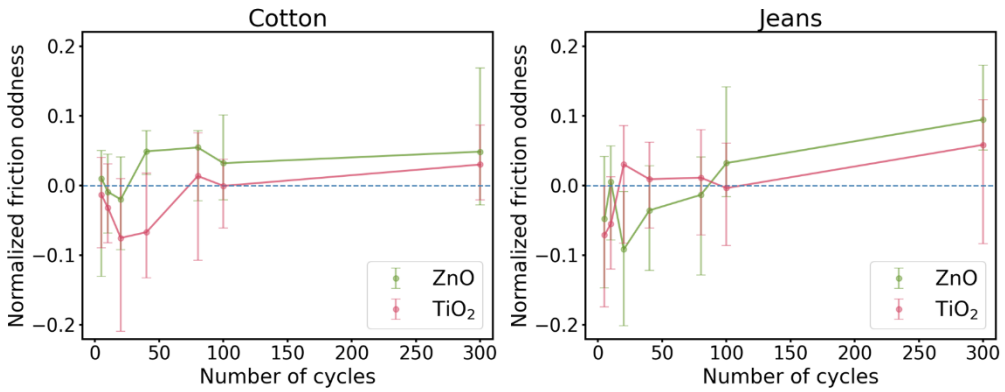

Figure 5.15. Evolution of the normalized friction oddness as a function of the number of cycles of each metal oxide treatment for cotton and jeans. Error bars correspond to the 25 and 75 percentiles.

We now can study the percentage of participants that have correctly identified the odd sample with the friction oddness for each sample and treatment, shown in **Figure 5.16**. In both fabrics, the samples with higher friction oddness are more easily identified as different, this is expected as

they are odd both in terms of treatment and in terms of friction, which is what the participants perceive. These samples are in the second quadrant of the graph, with a positive friction oddness and an above chance probability of being detected. When the participants touch these samples, they can feel the increase in the coefficient of friction and use it to detect the odd sample in the corresponding triplets. However, some samples are in the first quadrant of the graphs, with negative friction oddness and an above-chance probability of being detected. This implies that they are correctly identified, even when their COFs are not distinguishable from those of untreated samples.

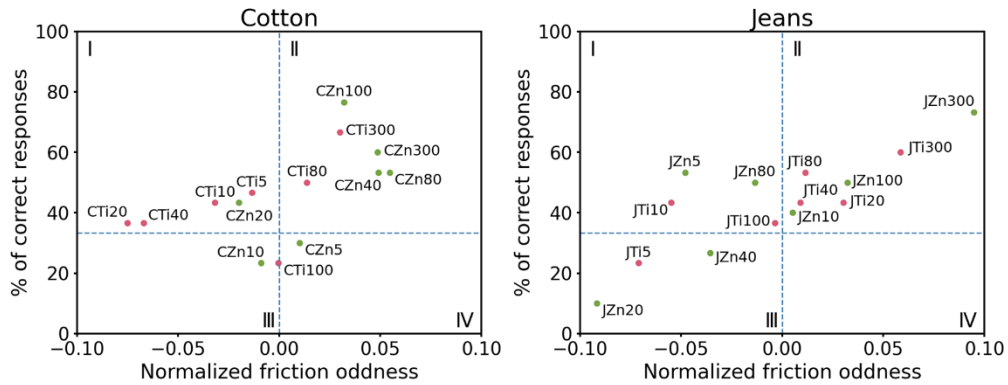

Figure 5.16. Percentage of participants that correctly identified the odd sample as a function of the mean normalized friction oddness of each treatment for cotton and jeans. The horizontal blue dashed line represents the probability of correctly identifying the odd sample by chance, the vertical blue dashed line separates the oddness cases.

The Odd Sample Out methodology allows to determine whether perceptible differences exist between two samples, but it does not give information about what the differences are or their magnitudes. These differences can exist in a single sensory attribute or in several attributes. This analysis of the friction oddness shows that participants can correctly identify the treated samples even when there are no perceivable differences in their COFs. Therefore, the infiltration of metal oxides via VPI is introducing changes in other sensory attributes of the fabrics.

5.2.2.4. Other factors – Structure, texture and bending stiffness

The participants were asked to fill out a questionnaire after completing every Odd Sample Out task. One of the questions they answered was *"Did you use any specific criteria when identifying the different sample? If yes,*

which criterium(a)?" Out of the 30 participants, 18 answered affirmatively. Each participant could list more than one criterium. The following criteria were mentioned with the frequency shown in brackets: roughness (9), friction (7), structure (4), softness (3), stickiness (2), humidity (2), and texture (1).

The roughness and structure of the fabric surface could not be directly measured using AFM, since it was not possible to approach the textile with the AFM tip, even with the addition of oils to reduce static repulsion. With this limitation, we focus on their sensorial perception. We asked participants to describe the differences they feel between the untreated and treated samples in more detail. The participants describe the feeling of the infiltrated samples as flatter and tougher, whereas the feeling of the untreated ones is described as softer and fuzzier. In order to explain the origin of these differences we studied the textile surface with an optical microscope. To do so, samples were cut with a scalpel and placed perpendicular to the objective lenses, the resulting images are shown in **Figure 5.17**.

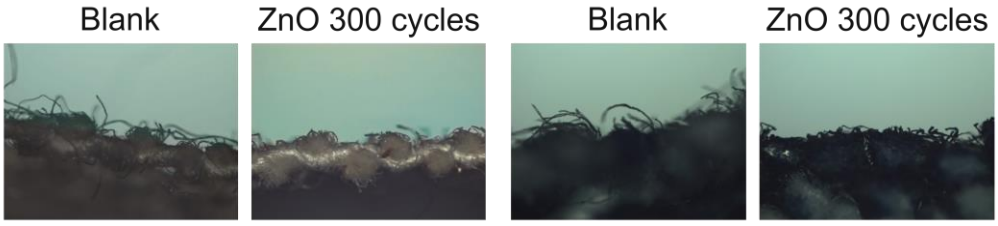

Figure 5.17. Optical microscope cross-section images of the surface of cotton and jeans samples before and after 300 cycles of ZnO infiltration.

In both fabrics, the untreated sample shows a large number of longer fibers that stick out from the compact surface of the woven fabric. Each thread within the woven fabric is formed by coiling of multiple thin fibers, some of which become unstuck and can cause the feeling of fuzz on top of the surface. They function as a cushion between the finger pads and the woven surface and make the samples feel softer. In contrast, the treated fabrics show only the compact surface with much shorter fibers. When the fibers are infiltrated with metal oxides, they become more brittle and can break off the fabric when the samples are manipulated after the treatment. This breakage makes the infiltrated surface feel flatter and firmer to the touch. We expect this change in surface morphology to affect the perception of

roughness, structure, and/or softness, making the samples treated with VPI distinguishable by tactile exploration even when the changes in their COF are not perceptible.

Another interpretation of the change in softness relates to the deformability of the samples affected by treatment. When participants touch the samples they apply a normal force, pushing into the fabric and making it bend around the finger. The resistance of the fabric to this deformation can also make the treated samples distinguishable. To analyze this change, we studied the changes in bending stiffness. A fabric with a greater bending stiffness will show more resistance to the push and will deform less under the same force than a fabric with lower bending stiffness.

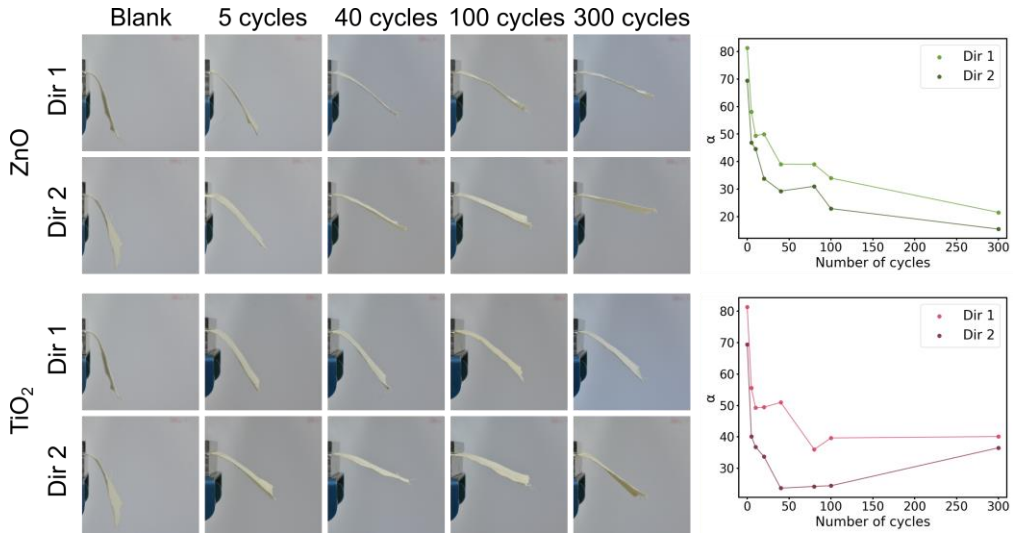

Figure 5.18. Self-bending angles of cotton infiltrated with different cycles of ZnO and TiO_2.

There is a natural anisotropy in the stiffness of the fabrics due to the weaving patterns, making one of the directions more rigid than the other. In cotton, this difference is not easily detected before treatment since the self-bending angle difference between the two measured directions is about 10°. As the number of cycles increases, the self-bending angles of the samples are reduced and the bending stiffness increases, but the difference between both directions remains constant. The anisotropy is only reduced when reaching 300 cycles, when the difference between the self-deflection

angles of the two directions is of 6° for ZnO and 4° for TiO_2. The measured self-bending angles are shown in **Figure 5.18**.

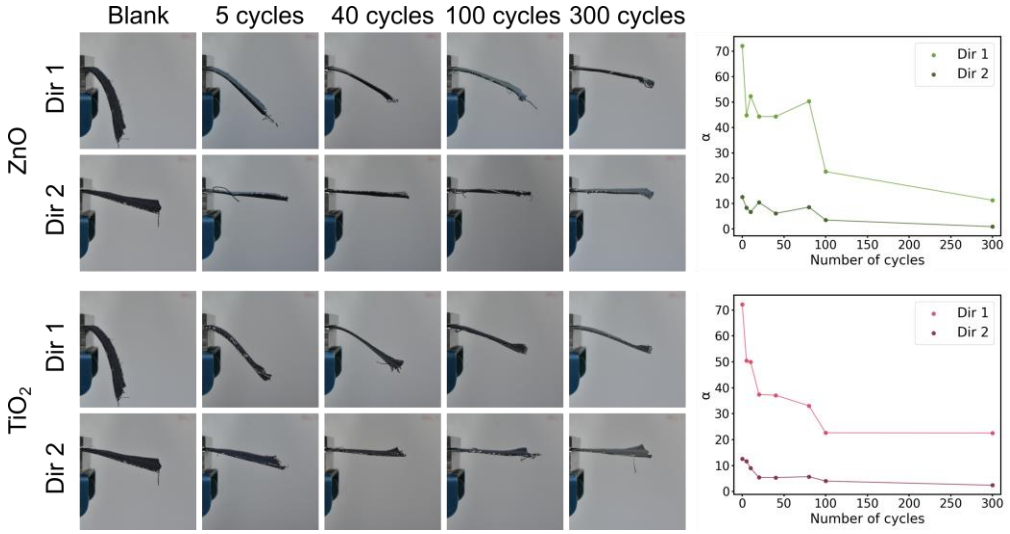

Figure 5.19. Self-bending angles of jeans infiltrated with different cycles of ZnO and TiO_2.

In the case of jeans, the original anisotropy is much more pronounced and easily perceivable, with a difference of 60° between the two directions. The angles in direction 2 are originally around 10°, making the variations introduced by treatment harder to measure, while the differences in direction 1 are clear. Consequently, we see a tendency in the anisotropy to decrease with the number of cycles, until reaching angle differences of 10° for ZnO and 20° for TiO_2 at 300 cycles. The measured self-bending angles are shown in **Figure 5.19**.

In both fabrics, the self-bending angles decrease after infiltration, meaning that the samples become stiffer. This effect becomes more perceivable as the amount of metal oxide is increased. This change is caused by the low ductility of the metal oxides, which are ceramic materials, infiltrated into the flexible fibers. Their combination increasingly affects the flexibility of the resulting hybrid textiles with the amount of infiltrated oxide. Visually, this change is easily perceivable, with the jeans samples even remaining unbent under their own weight. However, it should be harder to detect through tactile exploration, especially since the participants are only allowed to touch the surface with one finger pad and cannot hold or bend

the fabrics. Additionally, the participants only see the sample triplets through a semi-opaque screen and always placed on the metal and PDMS holders. We expect this change to affect tactile perception only when participants push into the samples with a higher normal force, feeling a harder resistance from the fabrics to sink into the PDMS when they are treated. This impression, in combination with the previously described ones, can be one of the factors contributing to the distinguishability of the hybrid textiles.

5.2.2.5. Probability of identifying the infiltrated fabrics

The Odd Sample Out methodology allows us to conclude whether a perceptible difference between samples exists following the standardized values in Table A.1. of ISO 4120:2004 [100]. If the number of participants that identified the different sample correctly is higher than the tabulated value, we can accept the assumption that a perceptible difference exists after the infiltration of the fabric. The minimum of correct responses needed depends on the desired α risk in our test. The results obtained for some of the standard values of α are shown in **Table 5.1** for cotton and in **Table 5.2** for jeans.

We can conclude that the samples treated with 300 cycles are perceived as different for both fabrics and oxides. In the case of infiltration with ZnO, samples treated with 100 and 80 cycles can also generally be perceived as different. Additionally, samples treated with 40 cycles are perceived as different when taking higher values of the α risk in the case of cotton. In the case of infiltration with TiO_2, we find the already mentioned anomality in the samples treated with 100 cycles, which are never distinguishable from the untreated ones. However, samples treated with 80 cycles are still perceived as different when taking higher values of the α risk in both types of fabric. Surprisingly, cotton samples treated with 5 cycles of TiO_2, and jeans samples treated with 5 cycles of ZnO are perceived as different for the higher values of the α risk. This is probably an effect of the higher statistical error that comes from the reduced number of participants. We expect this difference to disappear when significantly increasing the number of participants. As a conclusion, a treatment with 40 and 80 cycles of any of the two oxides is the minimum amount of infiltration needed in

both fabrics to reach just noticeable difference in tactile perception from the untreated sample.

Fabric		Cotton													
Oxide		ZnO							TiO_2						
Cycles		5	10	20	40	80	100	300	5	10	20	40	80	100	300
α	0.2														
	0.1														
	0.05														
	0.01														

Table 5.1. Summary of the Odd Sample Out study results for cotton samples at different values of the α risk. Samples with a perceptible difference from the untreated samples are marked in blue.

Fabric		Jeans													
Oxide		ZnO							TiO_2						
Cycles		5	10	20	40	80	100	300	5	10	20	40	80	100	300
α	0.2														
	0.1														
	0.05														
	0.01														

Table 5.2. Summary of the Odd Sample Out study results for jeans samples at different values of the α risk. Samples with a perceptible difference from the untreated samples are marked in blue.

Following the Odd Sample Out methodology in Annex B of ISO 4120:2004 [100], we calculate the proportions of the population that would be able to distinguish treated and untreated samples and their confidence intervals. Upper and lower confidence limits are calculated with 95% confidence, giving the confidence intervals an error allowance of 10%. In this way, we obtain 90% confidence that the true proportion of distinguishers is somewhere between the percentages shown in **Figure 5.20**. When a confidence interval includes 0%, it supports the conclusion that there is no perceptible difference between treated and untreated samples.

Cotton samples treated with ZnO would be distinguished by 10 to 50% of the population when the number of cycles is between 40 and 80. At 100 cycles, the maximum percentage reaches 85% but goes back to 62% at 300 cycles. Jeans samples treated in the same way need 80 to 100 infiltration cycles to be distinguished by a maximum of 50% of the population but

would be distinguished by 80% of the population when infiltrated with 300 cycles of ZnO.

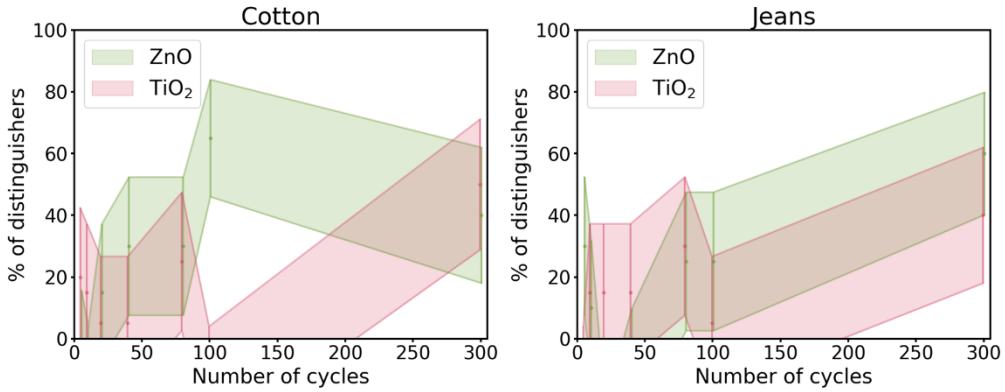

Figure 5.20. Percentages of the population that would be able to distinguish the treated fabrics from the untreated ones for cotton and jeans with 90% confidence.

In the case of infiltration with TiO_2, no treatment with less than 80 cycles would be distinguished for both cotton and jeans. For both fabrics, the maximum percentage of the population who distinguish the fabrics infiltrated with 80 cycles increases to 50%. The fabrics infiltrated with 100 cycles are again an anomality and would not be distinguished by most of the population. The percentage of distinguishers reaches 70% of the population for cotton and 62% for jeans when reaching 300 cycles of infiltration.

5.2.2.6. Change in skin moisture after touching the samples

During the study with participants, we noticed that the skin moisture measured after touching the samples tends to be higher than before, with an average increase of 8.15 a.u.. The corneometer measures in arbitrary units from 0 (no water at all) to 120 (on water) [106], with the measured skin moisture of the participants ranging from 14.96 to 105.88 a.u.. To check the significance of the change we run a paired or dependent samples t-test with α=0.05 comparing the skin moisture values before and after for each participant. The results are shown in **Figure 5.21**.

There is a significant difference between the values (p=0.0000, t-stat=-5.7613), meaning that the increase in the skin moisture during the study is noteworthy. This increase is high compared to that observed in similar studies with different samples. In a study with PU samples, in which

participants touch samples for double the time, the average moisture increased by 3.78 but the difference was not significant. The change observed in this study could be an effect of the hydrophobicity induced in the samples by the treatment.

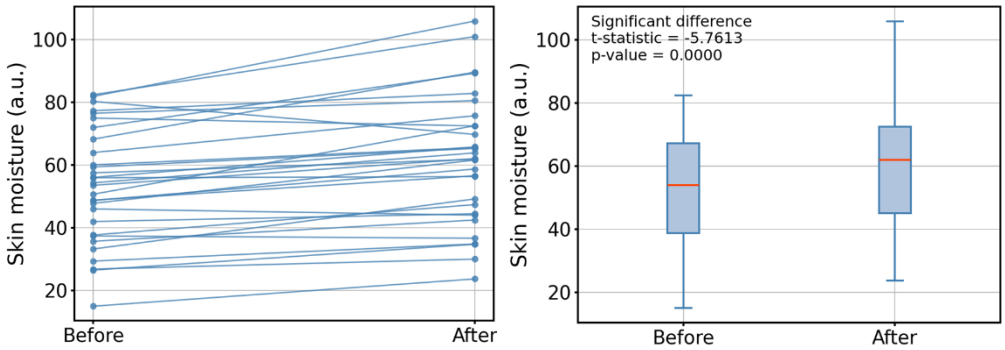

Figure 5.21. Paired samples plot and boxplot of the dependent samples t-test comparing the measured skin moisture of each participant before and after touching all samples.

5.3. Conclusions

We have studied how the treatment of cotton and jeans with ZnO and TiO_2 through Vapor Phase Infiltration affects the visual and tactile human perception of the fabrics.

To identify the changes in visual perception, the color of the fabrics before and after treatment was measured with a spectrophotometer and analyzed within the CIELAB color space system. The variations in each of the color coordinates are individually explored, as well as the absolute color differences. Following the CIE76, CMC, and CIE2000 standards, we can conclude that all samples but the one of jeans infiltrated with 300 cycles of ZnO are within the acceptable thresholds of consistency of reproducibility for the color of samples. Additionally, samples of cotton infiltrated with up to 80 cycles of ZnO are undistinguishable from the untreated ones in terms of color.

To investigate the changes in tactile perception, we have run an Odd Sample Out study with 30 participants and studied whether fabrics infiltrated by VPI can be identified as different from the untreated ones.

Physical measurements of force and position were conducted simultaneously to relate the perceived differences to the coefficient of friction of the samples.

The coefficient of friction of the fabrics is linearly dependent on the skin moisture of the finger pad of the participants. This relation is independent of treatment. The coefficients of friction measured in cotton fabrics are significantly lower than the ones measured in jeans. The increase of the coefficient of friction with the amount of metal oxide infiltrated in the fabric fits to an exponential function. This increase is 5% higher when treating jeans than when treating cotton. Samples infiltrated with 100 cycles of TiO_2 have a lower coefficient of friction than expected. The probability of distinguishing the treated samples increases with the coefficient of friction, as the fabrics become more different from the untreated ones. However, when incorporating the friction oddness into the analysis, we found that some samples can be identified as different even when they are not odd in terms of friction. This means that the treatment is modifying other properties of the fabrics that make the treated samples distinguishable.

The texture and structure of the fabric surface were observed under the microscope. We show that after infiltration the samples appear flatter, with the threads that stick out of the woven surface looking shorter and stiffer. The addition of the ceramic metal oxide makes them more brittle, which makes them break, losing the fluffier feel of the untreated samples. The stiffness of the fabrics was studied by measuring their self-bending angles. We detected a general increase in the stiffness of the samples for every fabric and treatment, making them more resistant to deformation. The original anisotropy due to the weaving of the fabrics is also reduced with the infiltration. We expect these changes to contribute to the distinguishability of the treated fabrics during the tactile exploration, making it possible to correctly identify the odd sample even in cases where the coefficient of friction is not different.

We have applied the Odd Sample Out methodology to conclude which samples present perceivable differences. Samples treated with 300 cycles are always perceived as different for both fabrics and treatments. In the case of infiltration with ZnO, samples treated with 100 and 80 cycles can

also generally be perceived as different as well as samples treated with 40 cycles when taking higher values of the α risk. In the case of infiltration with TiO_2, samples treated with 100 cycles are never distinguishable from untreated ones while samples treated with 80 cycles can still be perceived as different. Finally, we have calculated the percentages of the population that would be able to distinguish each sample. Most of the population would not perceive fabrics infiltrated with less than 80 cycles as different from the untreated ones. Fabrics infiltrated with 80 cycles or more would be distinguished by 50% or more of the population. The samples infiltrated with 100 cycles of TiO_2 would not be distinguished by most of the population. Cotton samples infiltrated with ZnO would be the most easily distinguished.

After touching each of the samples in the study, the skin moisture of the participants significantly increased. This change was not observed in similar studies with other materials, even for longer tactile exploration times. We expect this to be an effect of the enhanced hydrophobicity of the infiltrated samples.

Regarding visual perception, the color of any sample treated with 80 cycles or less can be perceived as the original one. Regarding tactile perception, a treatment of between 40 and 80 cycles of any of the two oxides would be the minimum amount of infiltration needed to reach the just noticeable difference from the untreated sample. Therefore, the combination of both studies allows us to identify the optimal amount of each metal oxide infiltrated while still being close enough to the untreated sample. We can now apply this knowledge to use VPI to obtain multiple new functionalities without disturbing the original appearance and feeling of the original textiles.

6

Summary and outlook

Textiles are omnipresent in our lives and have become so common that we no longer perceive them as technology. Natural textile fibers possess multiple interesting properties that make them well suitable for conventional fabric applications, often outperforming synthetic alternatives. However, they often lack specific functionalities demanded by advanced applications. The implementation of hybrid materials into textiles allows for incorporation of new functional properties while maintaining the inherent benefits of the pristine fibers. Despite the variety of existing methods for the synthesis of hybrid textiles, issues that hinder practical utilization, such as durability, toxicity, and versatility, are still challenging.

VPI is a vapor-to-solid technique that enables the synthesis of durable hybrid materials by infiltrating inorganic compounds into soft polymeric substrates, creating a subsurface gradient through strong chemical bonding between both materials. In this PhD thesis, VPI was applied to synthesize advanced multifunctional hybrid textiles. Two types of cotton-based fabrics were selected as substrates, a natural raw cotton fabric with minimal manufacturing, and a treated commercial jeans fabric with a blended composition of cotton and polymer fibers. Both were infiltrated with ZnO and TiO_2, materials that naturally exhibit a multiplicity of desired functionalities in addition to excellent stability and biocompatibility. Furthermore, these metal oxides can be readily deposited by ALD and derived techniques at low temperatures using standard, inexpensive precursors.

A standard VPI process was developed and optimized for the infiltration of 3 pieces of fabric of 5x5 cm^2 in a single process. Parameters such as process temperature and dosing and purging times were chosen attending to the limitations introduced by the thermal resistance of the substrates, induced chemical damage and homogeneity in the chamber.

The structure and composition of the fibers forming both fabrics were characterized before and after infiltration to confirm the successful modification of the polymers. Imaging and chemically resolved mapping of the cross-section of the fibers by SEM and EDX show that the developed VPI process achieves growth of the metal oxides inside of the threads, individually infiltrating each of the fibers that form the macroscopic pieces of fabrics. ICP-OES was used to quantify the Zn and Ti amounts in the infiltrated fabrics, concluding that natural raw cotton allowed more infiltration of the metal oxides than commercial jeans and that the amount of infiltrated ZnO is higher than that of TiO_2 for the same processing conditions. XRD proved that the structural order of the textile polymers was not affected by the infiltration, infiltrated ZnO grew in its wurtzite crystalline phase with a compressed unit cell while TiO_2 grew amorphous. Uniaxial tensile tests ensured that the mechanical properties of the fabrics were not deteriorated by the infiltration.

Once the prepared hybrid fabrics were thoroughly characterized, their potential functionalities were evaluated. The results confirmed that photoprotection, self-cleaning activity through photocatalysis and hydrophobicity, antimicrobial and anti-odor activity, and flame retardancy can be successfully incorporated into the fabrics through one single VPI process.

Protection against UV radiation was achieved by extending the absorption of the fabrics into UVA and near visible regions, with TiO_2-infiltrated fabrics providing superior protection against erythema-inducing radiation than ZnO-infiltrated fabrics.

The chemical self-cleaning activity of ZnO-infiltrated cotton was demonstrated through photodegradation of rhodamine B under simulated solar light, showing that the hybrid fabrics could repeatedly degrade the organic dye without loss of efficiency. Physical self-cleaning was evaluated

through wettability measurements. Natural raw cotton preserved its inherent hydrophobicity after infiltration, while jeans transformed from superhydrophilic to superhydrophobic, with contact angles above 120°. Furthermore, liquid droplets remained on the fabric surface between several minutes and over an hour without being absorbed. The combination of photocatalytic activity and water repellency provides the hybrid fabrics with self-cleaning capability, preventing staining and contamination.

The antibacterial activity of the fabrics was evaluated against the model strains *S. aureus* and *E. coli*, as well as against the body odor causing strain *C. striatum*. Bacteriostatic, non-leaching antibacterial activity was achieved through VPI, preventing bacterial attachment and proliferation on the fabrics. The antifungal activity of ZnO-infiltrated fabrics was assessed through their inhibition capability against the model fungus *A. nidulans*, showing partial antifungal activity by inhibiting spore germination but not hyphal growth. Overall, the hybrid fabrics demonstrated effective antimicrobial activity, particularly remarkable in the case of ZnO infiltration.

The fire resistance of the hybrid fabrics was assessed by exposing them to an open flame and visually analyzing their combustion behavior. The hybrid fabrics had significantly delayed ignition times and rapid self-extinguishment, which minimized fire-induced damage to the textile structure and effectively suppressed smoke generation.

The durability of the infiltration against conventional laundering was tested by comparing the fabrics´ properties before and after washing. ZnO-infiltrated fabrics retained both their photoprotective and antibacterial functionalities, whereas TiO_2-infiltrated fabrics exhibited a partial loss of performance, preserving photoprotection but losing bacteriostatic activity. These results indicate that laundering damaged the superficial TiO_2 coating, while the subsurface TiO_2-fiber gradient remained intact.

Lastly, the effect of the infiltration on the visual and tactile perception of the fabrics was studied. Visual changes were identified through color measurement and analysis within the CIELAB color space system. All samples, except jeans infiltrated with 300 cycles of ZnO, remained within

acceptable thresholds of color variation. Cotton fabrics treated with up to 80 cycles of ZnO infiltration were visually indistinguishable from the pristine samples. Changes in tactile perception were analyzed by combining fingertip friction and movement measurements with an Odd Sample Out study conducted with 30 volunteers. The results showed that fabrics infiltrated with fewer than 80 cycles were generally perceived as identical to untreated fabrics, while those with 80 cycles or more were distinguished by at least 50% of participants. The coefficient of friction increased with the number of infiltration cycles, although friction oddness analysis indicated that some samples could still be identified as different even without a measurable increase in friction. Further analysis of sensory attributes revealed that the texture and structure of the fabrics were also modified by the infiltration process, making them flatter and stiffer to the touch.

The measured properties confirm infiltration of metal oxides into cotton-based fabrics by VPI as a powerful tool to achieve durable multifunctionalization. Combined with perceptual studies, this knowledge can be applied to the design of advanced hybrid textiles that integrate multiple new functionalities of high relevance for the textile industry while preserving the original appearance and feel of pristine fabrics.

Looking towards the future, further investigation should focus on extending the application of the developed infiltration process to textiles with diverse compositions, as well as exploring alternative functional materials to widen the range of achievable properties, including electrical conductivity, sensing capabilities, and thermal regulation. In parallel, the process and reactor designs need to be scaled to enable the treatment of larger textile pieces. The durability of the functionalization must be evaluated under real use and laundering conditions to assess long-term stability. Finally, systematic studies on biocompatibility and environmental impact will be essential to ensure a safe and sustainable implementation of VPI-functionalized textiles in industrial applications.

Further research

7

Low temperature atomic layer deposition of boron nitride using the in-situ decomposition of ammonium carbamate

This chapter is dedicated to the development of a new atomic layer deposition process for the growth of amorphous boron nitride at low temperatures, between 100 and 275°C, using ammonium carbamate as the nitrogen source. Carbamic acid is formed during the thermal decomposition of ammonium carbamate. This intermediate, highly reactive species, acts as the enabler of nitride deposition at low temperatures.

A brief introduction to the interest in nitrides and their deposition by ALD is given. The ALD process for BN is characterized, and the composition, stoichiometry and structure of the deposited thin films are analyzed. Finally, the reaction pathways are computationally modeled to confirm the enhanced reactivity of the reactants introduced in the studied process.

This work, which started as my master thesis, continued throughout my years as a PhD student and resulted in the publication of the scientific communication: Álvarez-Yenes, A.; Koroteev, V.; Ryzhikov, M.; Ilyn, M.; Kozlova, S.; Knez, M. Low temperature atomic layer deposition of boron nitride using the in situ decomposition of ammonium carbamate. ***Chem. Commun.,*** 2025, **61**, 11774-11777.

7.1. Introduction

Nitrides are critically important materials in modern technology because of their unique combination of properties. They are chemically and thermally stable, with melting points often exceeding 2000°C, which makes them highly resistant to wear and corrosion. Depending on the specific nitride compound, they can either act as electrical conductors or as insulators, while semiconducting nitrides are particularly valued for their wide bandgaps. These characteristics make nitrides essential for applications ranging from high-power electronics, where gallium nitride (GaN) enables energy-efficient power transistors, to optoelectronic emitters such as GaN-based LEDs and laser diodes [107]. In sensing technologies, aluminum nitride (AlN) is used in piezoelectric sensors and resonators due to its high acoustic velocity and thermal stability [108]. Nitrides also serve as protective coatings, for example titanium nitride (TiN), which provides wear resistance and a biocompatible surface for medical implants and surgical tools [109], [110].

The rapid development of these application fields, particularly the continued scaling down of semiconductor devices, has created a demand for highly conformal, pin-hole free nanoscale thin films. At the same time, process temperature limitations have become increasingly relevant due to the introduction of novel materials into the fabrication processes. This includes polymers in both flexible electronics and as low-k dielectric materials, which are highly temperature-sensitive and require deposition techniques compatible with delicate substrates [111]. As a result, processing temperatures are typically restricted to less than 400°C [112]. Inherently, ALD is a very suitable and promising technique for the coating of high aspect-ratio structures with excellent conformality, as well as precise compositional and thickness control. However, the ALD of nitrides for practical application is limited by the availability of sufficiently reactive nitrogen precursors.

Although over 100 processes for the deposition of nitrides by ALD have been reported, most of them use ammonia (NH_3) as the nitrogen source [113]. Due to its low reactivity, ammonia typically requires elevated process temperatures to thermally activate its adsorption and reaction, which restricts its applicability [114]. Moreover, ammonia is a colorless,

toxic, and corrosive gas that is difficult to detect with standard laboratory sensors, making its handling a safety issue in many research and industrial settings. Hydrazine (N_2H_4) and its derivatives have been used as more reactive alternatives, but their toxicity and explosiveness make them even more hazardous and harder to handle than ammonia, again impeding their widespread industrial adoption [115].

In Plasma-Enhanced ALD (PEALD), a plasma source is introduced to generate highly reactive species that enhance precursor reactivity and allow deposition at lower process temperatures. For nitride growth, plasmas of NH_3, N_2 or N_2/H_2 mixtures are generally used. Unfortunately, PE-ALD has some limitations regarding substrate compatibility. The high reactivity of the radicals produced by plasma can damage or even etch other materials used in device fabrication processes, such as silicon substrates and polymer-based materials [112].

In this work, we propose ammonium carbamate ($[NH_4][H_2NCO_2]$) as an alternative nitrogen source for ALD. Ammonium carbamate is a solid at ambient conditions that thermally decomposes into various reactive gaseous species. This allows for the growth of nitrides at relatively low processing temperatures while making the handling of the chemicals safer, widening the possible applications of the deposition processes. To explore its potential, we combine it with boron tribromide (BBr_3) to grow boron nitride (BN) by ALD.

BN is a binary compound of boron and nitrogen, alternatively linked, which can be obtained in various crystalline forms. It is the lightest of the III-V compounds, making the BN allotropes analogous and isoelectric to the carbon ones, forming bonds with sp^2 and sp^3 hybridization. In all these forms, BN exhibits interesting optical and electronic properties while being highly thermally and chemically stable, making it attractive for numerous applications, especially in nanoscience and nanotechnology. The sp^2-hybridized hexagonal boron nitride (h-BN) is the better-known BN allotrope. B and N crystallize in the characteristic planar sheet layered structure which is typical of Van-der-Waals materials [116]. It has high electrical resistivity, excellent thermal conductivity, and wide bandgap and has been applied as protective coating due to its corrosion-resistance, as lubricant, as insulator layer in semiconductors, as emitter and as

photodetector in the deep UV region [117], [118], [119], [120]. The sp^3-hybridized cubic boron nitride (c-BN) is the second most common BN allotrope. It is the second hardest material known after diamond, with a Vickers hardness of around 50 GPa [121]. c-BN is, however, more thermically and chemically stable than diamond, making it abrasion resistant and particularly useful for applications in the manufacturing industry [122], [123]. It can be used as protective in optics since it is transparent in the visible range, and applied in high temperature, high power electronics operating in harsh environments as a heat sink [124]. Boron nitride can also be obtained in a non-crystalline form, with no discernible long-range order in its atomic arrangement. This allotrope is known as amorphous boron nitride (a-BN) and is sp^2 hybridized. This material has great potential as diffusion barrier in electronic devices; it readily adheres to the substrates and has a hardness higher than that of silicon [125]. Moreover, a-BN has been reported to have an ultralow dielectric constant, which would extend its applicability to insulating layers in CMOS technology [126], [127], [128], [129]. The synthesis and post-treatment of BN determine its allotropic shape and, therefore, its physical properties and optimal future applications [130], [131].

Atomic layer deposition has been previously used to deposit BN thin films, primarily by using boron halides in combination with ammonia, a precursor selection derived from CVD. The growth of BN from BCl_3 and NH_3 by ALD was first reported by Ferguson et al. [132]. However, BBr_3 is less thermodynamically stable than BCl_3 and reacts readily with ammonia. This combination of precursors has been used by Mårlid et al. [133] and Weber et al. [134] in high temperature ALD processes (400-750°C). To lower the process temperature, Olander et al. [135] introduced the photo-dissociation of BBr_3 with an ArF excimer, increasing its reactivity with the surface and enabling the deposition of BN at 250°C.

The process proposed here allows the ALD-growth of BN at lower temperatures, between 100 and 275°C, using BBr_3 and ammonium carbamate as precursors. Ammonium carbamate coexists in equilibrium with a mixture of NH_3 and carbon dioxide (CO_2) at ambient conditions. This chemical system has been thoroughly characterized and there are several studies describing its vapor pressure and composition as a function of

temperature [136], [137], [138], [139]. The kinetics of the decomposition are less well understood. Multiple studies point at the involvement of carbamic acid (H_2NCOOH), a highly reactive intermediate, in the process. Carbamic acid has never been isolated, although organic derivates have been prepared [140]. Experimental and computational studies conclude that it appears as a surface-bound intermediate species that can be evacuated, making it compatible with ALD [141]. The proposed scheme of the ALD reaction is shown in **Figure 7.1**. Reaction (A) describes the decomposition of ammonium carbamate into NH_3 and CO_2, with the intermediate formation of carbamic acid. Reaction (B) is the proposed surface reaction between carbamic acid and BBr_3 during an ALD cycle.

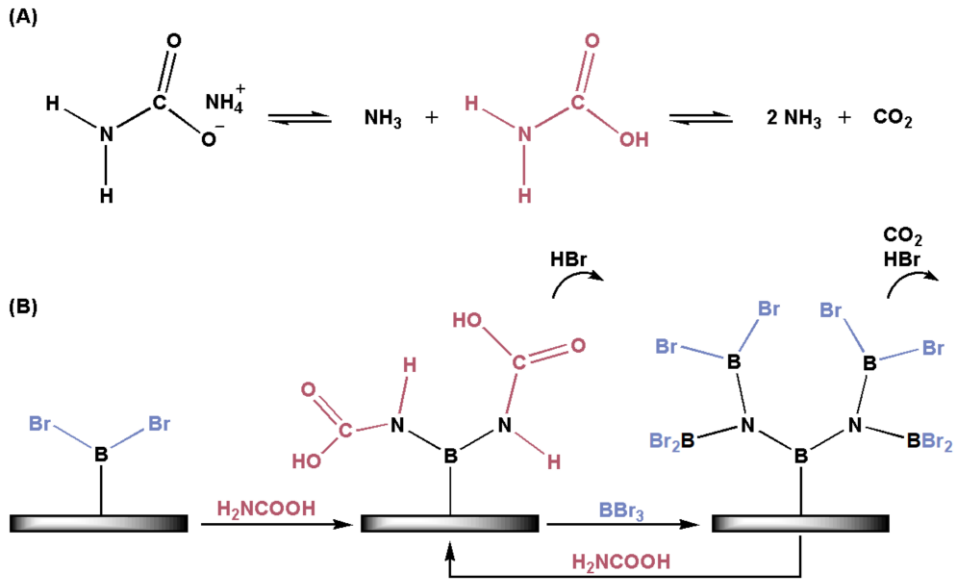

Figure 7.1. Schematic reactions that take place during the deposition process. (A) Decomposition of ammonium carbamate. (B) ALD-growth of BN from surface-bound BBr_3 and carbamic acid.

7.2. ALD process

7.2.1. Experimental details

The ALD processes were performed in a Savannah reactor from Cambridge Nanotech. The deposition was carried out under a constant N_2 flow of 20 sccm. Boron tribromide (BBr_3, 99%, Acros Organics) was used as boron

source and ammonium carbamate ([NH_4][H_2NCO_2], +99%, Sigma Aldrich) was used as nitrogen source. BBr_3 was kept at room temperature during the deposition and ammonium carbamate was heated to 50°C to provide sufficient vapor pressure. Depositions were done at various process temperatures between 100 and 275°C.

The thicknesses of the samples were extracted from X-ray reflectivity (XRR) measurements performed with a PANalytical X'pert PRO diffractometer with a CuKα (λ=1.542 Å) radiation source and working voltage and current of 45 kV and 40 mA, respectively. Silicon (100) wafers with native oxide were used as substrates.

7.2.2. Characterization of the process

Experiments varying the pulsing time of BBr_3 were carried out to study the self-limiting nature of the surface reactions. An ALD cycle for the BBr_3 saturation experiment consisted of a BBr_3 pulse of X ms, followed by a N_2 purge of 5 s, a [NH_4][H_2NCO_2] pulse of 15 ms and a subsequent N_2 purge of 10 s, where X stands for a variable dosing time. **Figure 7.2** shows the results obtained for 400 ALD cycles at 150°C.

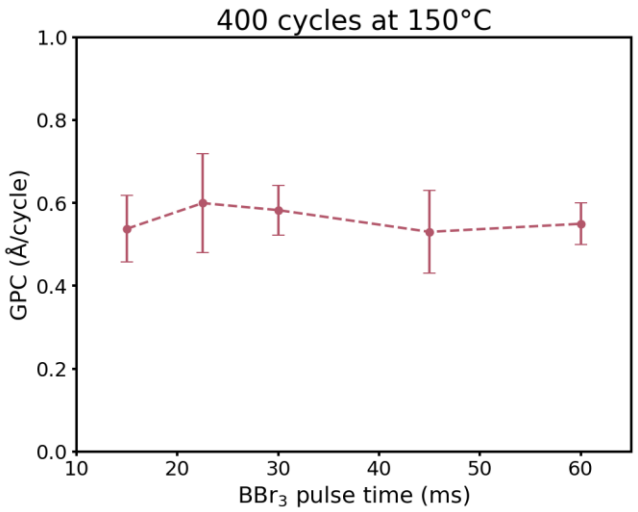

Figure 7.2. Growth per cycle (GPC) of the process as a function of the BBr_3 pulse time, extracted from XRR measurements of thin films grown by 400 ALD cycles at 150°C.

The obtained growth per cycle (GPC) remains constant as the dosing of the precursor is increased. The graph verifies the self-limiting nature of the film deposition already at shortest possible dosing times. Therefore, the dosing time of BBr_3 was set to 15 ms in following experiments, the minimum precision allowed by the dosing valve. The dosing time of $[NH_4][H_2NCO_2]$ was not varied since the minimum dosing of 15 ms already caused a large pressure increase in the reaction chamber. Increasing the purge times after each pulse from 5 and 10 s, respectively, to 60 s did not alter the growth rates. Consequently, an ALD cycle was set as 15 ms of BBr_3 dosing, 5 s of N_2 purge, 15 ms of $[NH_4][H_2NCO_2]$ dosing and 10 s of N_2 purge for all further experiments to fulfill a self-saturated condition for the studied ALD processes.

We studied the dependence of the GPC on the deposition temperature in the range from 100 to 275°C with the timing sequence determined before. The measured thicknesses of the deposited BN thin films as a function of the number of ALD cycles and the GPC of the process at different deposition temperatures are shown in **Figure 7.3**. The error bars represent the data spread from different experiments; each point averages a minimum of 4 measurements.

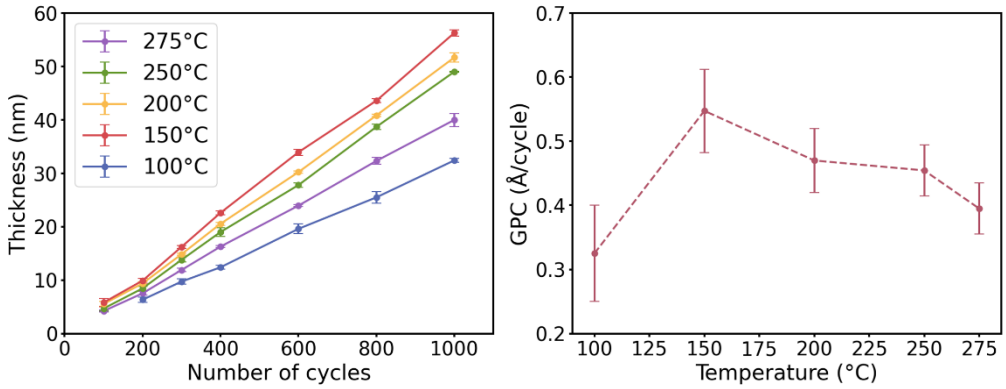

Figure 7.3. Measured thicknesses of the deposited films as a function of the number of ALD cycles at different deposition temperatures (left) and dependence of the GPC of the ALD process on the deposition temperature (right).

Deposition at 100°C yields the lowest GPC, about 0.33 Å/cycle, probably limited due to lower kinetic activation of the precursors at lower temperatures. The maximum GPC of 0.55 Å/cycle is reached at 150°C. The GPC stabilizes around 0.47 Å/cycle at 200 and 250°C. A further increase of

the temperature to 275°C leads to a slight decrease in the GPC reaching a value of 0.40 Å/cycle. At each temperature, a lower GPC is observed during the first few deposition cycles, corresponding to the number of cycles needed to fully coat the substrate surface with BN. Once this phase is completed and the surface is fully covered, the thickness of the deposited films increases linearly with the number of cycles, as expected from an ALD process. This process has been used to successfully grow BN on etched silicon, anodic alumina, sputtered nickel, glass, and sapphire substrates, obtaining similar GPCs.

7.3. Characterization of the as-deposited material

7.3.1. Composition and stoichiometry

The composition of the deposited films was analyzed using X-ray photoelectron spectroscopy (XPS). XPS measurements were carried out with a Phoibos 100 photoelectron spectrometer, using a non-monochromatic Al–Kα X-ray source in an ultra-high vacuum chamber with a base pressure of $5x10^{-10}$ mbar. The analyzer energy resolution was 0.1 eV. Before the XPS measurements, the sample was sputter-etched with 500 eV Ar ions for 5 minutes to remove a surface layer of an estimated thickness of 1-2 nm. These measurements were carried out by Dr. Maxim Ilyn at the Nanophysics Lab of the Material Physics Center (CFM) in Donostia-San Sebastián, Spain. The resulting spectra, corresponding to a 12 nm thick BN film deposited at 150°C, are shown in **Figure 7.4**.

The B 1s and N 1s peaks are localized at binding energies of 190.7 and 398.1 eV, respectively. These values are characteristic of h-BN and indicate that the films are composed of alternatively bonded, sp^2-hybridized B and N atoms. The relative atomic fraction of each element can be extracted from the area of the peaks weighted by the corresponding elemental sensitivity factors. The B:N atomic ratio obtained by applying this method is 1:1.05, well corresponding to the expected stoichiometry of BN.

Signals corresponding to C, O and Si atoms were also found. The Si signal stems from the etched silicon wafer used as substrate, Si atoms mostly

form Si-Si bonds with a small contribution of Si bonded to O. To kickstart the growth of BN on top of etched silicon, the substrate surface was exposed to ozone (O_3) before the deposition process, terminating the Si substrate surface with oxygen. Peak deconvolution of the B 1s peak shows a small concentration of B-O bonds. This contribution is likely to stem from the oxygen monolayer introduced by ozone, which would react only with BBr_3 and not with ammonium carbamate, which can explain the lower GPC during the first few cycles of the process until the substrate surface is completely functionalized with B-Br bonds.

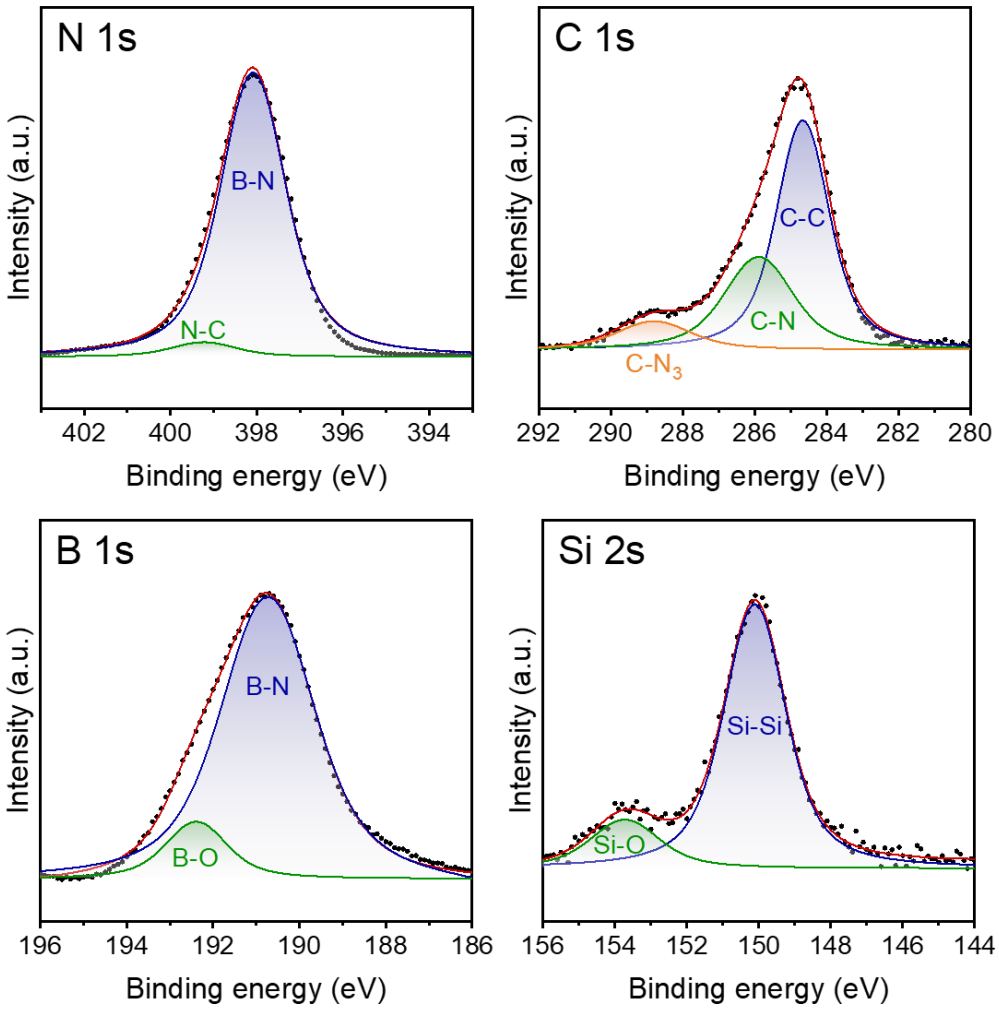

Figure 7.4. XPS spectra around the N 1s, C 1s, B 1 s and Si 2 s core-levels of a 12 nm film of BN deposited on etched silicon at 150°C.

The carbon atoms found in the sample are attributed to organic impurities in the precursors. The C atoms found in the sample appear either bonded to N atoms or forming sp^2 C-C bonds. Such defects are commonly reported in CVD-grown BN films, as C atoms are similar in size to both B and N atoms and can substitute them without introducing any lattice mismatch [142].

7.3.2. Atomic arrangement and structure

In order to study the atomic arrangement of the deposited films, as well as to obtain their spatially resolved composition, transmission electron microscopy (TEM) and electron energy loss spectroscopy (EELS) were used. TEM characterization was carried out with a Cs-corrected microscope ThermoFisher FEI Titan 60-300, operated in monochromatic mode at an accelerating voltage of 300 kV. The presented results correspond to a multilayered sample of 500 nm Ni/10 nm ALD BN/10 nm Fe in which the metallic layers were grown by sputtering and the ALD BN layer deposited at 150°C. The obtained EELS maps are shown in **Figure 7.5**.

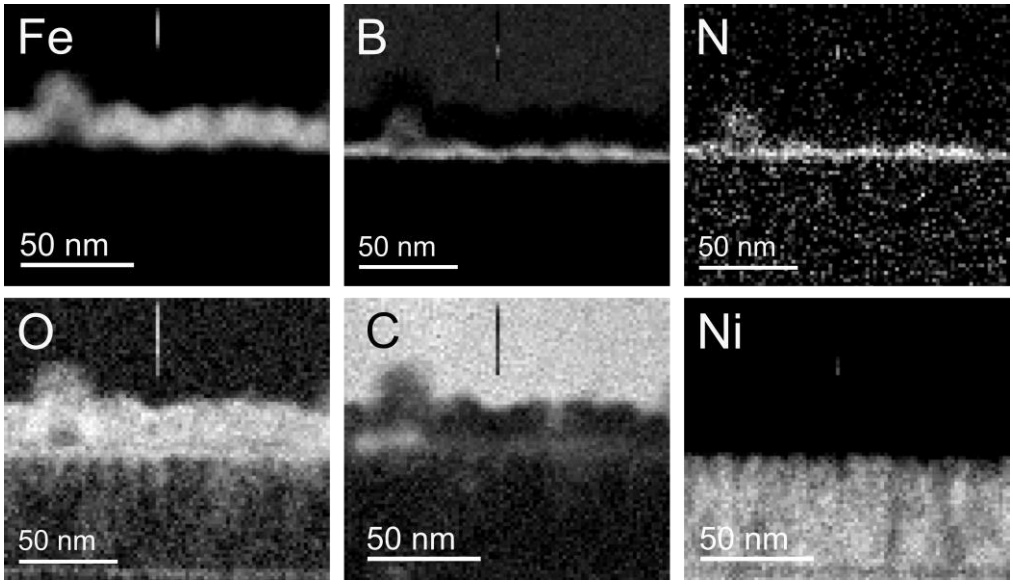

Figure 7.5. Cross-sectional EELS mapping of the chemical elements detected in a 500 nm Ni/10 nm ALD BN/10 nm Fe stack.

EELS mapping proves that B and N atoms are localized in the middle layer of the sample, further confirming the formation of boron nitride during the deposition. The thickness of the ALD BN film obtained by TEM (10 nm)

matches that obtained by XRR (10.36 nm), validating the results obtained by the latter method. Fe atoms in the sample coincide with oxygen, showing that the sputtered Fe layer oxidizes upon exposure to air. The Ni surface is also oxidized. Some oxygen is also found in the BN layer. We expect the incorporation of oxygen to result from post deposition exposure to air. The even distribution of oxygen throughout the film indicates that the incorporated O diffuses through the deposited film, a phenomenon already reported for the deposition of nitrides by different techniques, including ALD [143]. The diffused O atoms may hydrolyze remains of incompletely ammonolyzed BBr_3, likely due to the lower deposition temperatures, resulting in the formation of some boron oxide within the deposited BN film. C atoms corresponding to the previously mentioned precursor contamination, as well as from potential atmospheric contamination, are also found in the sample.

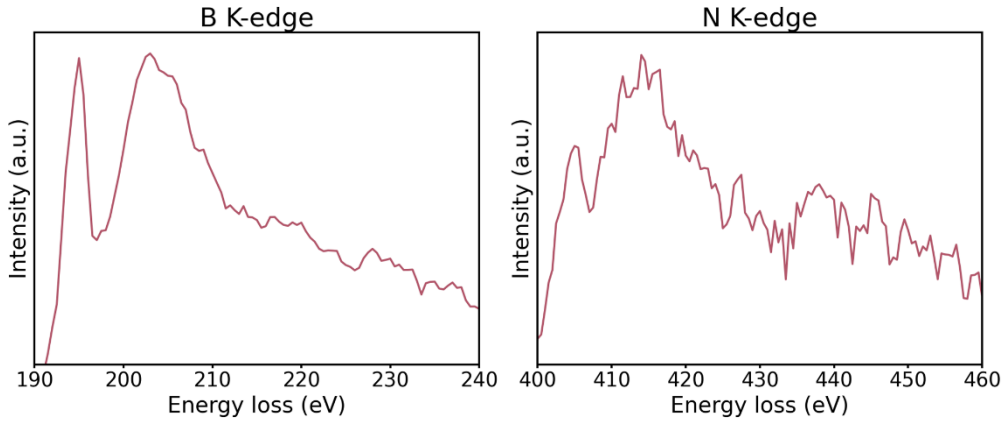

Figure 7.6. EELS Spectra of the K-edges of B and N from a 500 nm Ni/10 nm ALD BN/ 10 nm Fe stack.

The near edge EELS spectra, measured for B and N atoms, are shown in **Figure 7.6**. The B K-edge presents two peaks, one sharper corresponding to an energy loss of 195 eV and one wider around an energy loss of 202 eV. The N K-edge has a sharp peak at 405 eV and a wider region of high intensity in energy losses of between 410 and 420 eV. These energy values coincide with those found in the near edge spectra of h-BN and are characteristic of the sp^2 hybridization of B and N, respectively [144]. Considering the shape of the spectra, the features are wider and more diffuse than those typically obtained from h-BN, pointing to a somewhat

ill-defined binding energy of the photoemitted electrons and a lower level of long-range order in the deposited films. We therefore expect the allotropic form of the grown BN to be amorphous.

To confirm the amorphous nature of the deposited BN, Raman spectroscopy and grazing incidence X-ray diffraction measurements (GI-XRD) were performed. The results are shown in **Figure 7.7**.

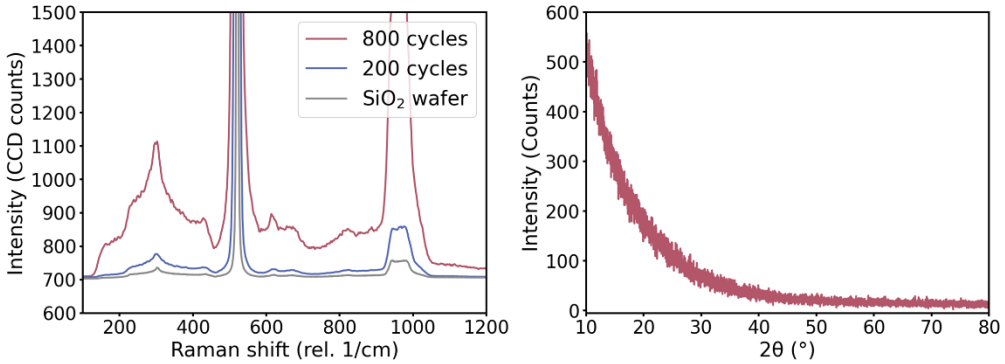

Figure 7.7. Raman spectra (left) and GI-XRD pattern (right) of ALD-grown BN films.

The Raman spectra correspond to BN thin films of different thicknesses deposited on SiO_2 wafers at 250°C. The measured intensity increases with the number of cycles, proportionally to the thickness of the film. However, the spectrum of a-BN is identical to that of the SiO_2 substrate, suggesting that no distinct crystalline h-BN modes are present in the film. Similar results have been previously reported in CVD-grown a-BN thin films [126]. The GI-XRD pattern corresponds to a 23 nm thick BN film deposited on sapphire at 150°C. The absence of diffraction peaks further confirms the lack of a crystalline structure.

7.3.3. Density

To complete the characterization, the density of the thin a-BN films, deposited as a function of the deposition temperature, was obtained from XRR fitting. The results are shown in **Figure 7.8**. Each point averages the density obtained from 3 different films of varying thickness. The density remains constant at each deposition temperature studied, with values ranging from 1.73 to 1.78 g/cm^3. These values are in good accordance with

those previously reported for ALD-grown BN by Mårlid et al. [133] who obtained densities of 1.65-1.70 g/cm^3 at a deposition temperature of 400°C and of 1.90-1.95 g/cm^3 at 750°C.

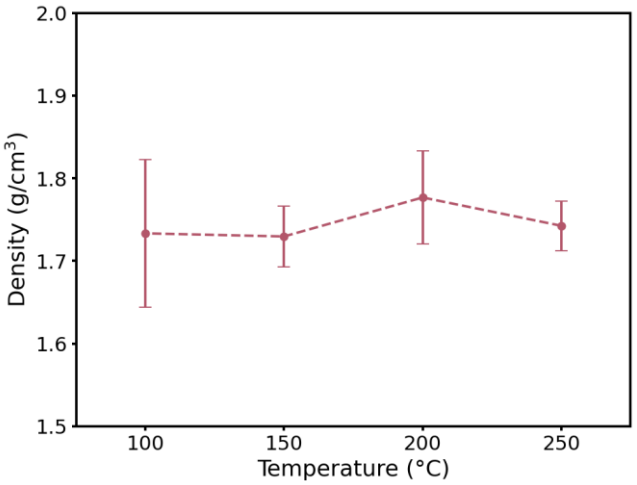

Figure 7.8. Fitted density of the deposited BN films as a function of the deposition temperature.

7.4. Computational modeling of the reactions

To prove that the enhanced reactivity of the proposed nitrogen source is what enables the deposition at lower temperatures, the reaction pathways between carbamic acid and NH_3 in combination with BBr_3 were modeled. The calculations of the model systems were performed within ADF engine of the AMS2023 program suite [145]. The TPSSh meta-hybrid density functional [146], Grimme D4(EEQ) dispersion correction [147], all-electron Slater Type Orbitals QZ4P basis set [148] and Zero Order Regular Approximation (ZORA) for scalar relativistic effects [149] were used in all calculations. These calculations were carried out by Dr. Maxim R. Ryzhikov and Dr. Svetlana G. Kozlova at the Nikolaev Institute of Organic Chemistry in Novosibirsk, Russian Federation.

The Gibbs free energy of the model reactions between H_2NCOOH and BBr_3, and NH_3 and BBr_3 were calculated at 100°C to identify their transition states and local minima. The Intrinsic Reaction Coordinate (IRC) [150]

method was used to link the reagents, transition states, and products of the model reactions. The evolution of the Gibbs energy differences, and molecular structures of both reactions are shown in **Figure 7.9.** The Gibbs energy difference values plotted are relative to the pre-reaction complexes $H_2NCOOH\cdots BBr_3$ and $NH_3\cdots BBr_3$, respectively.

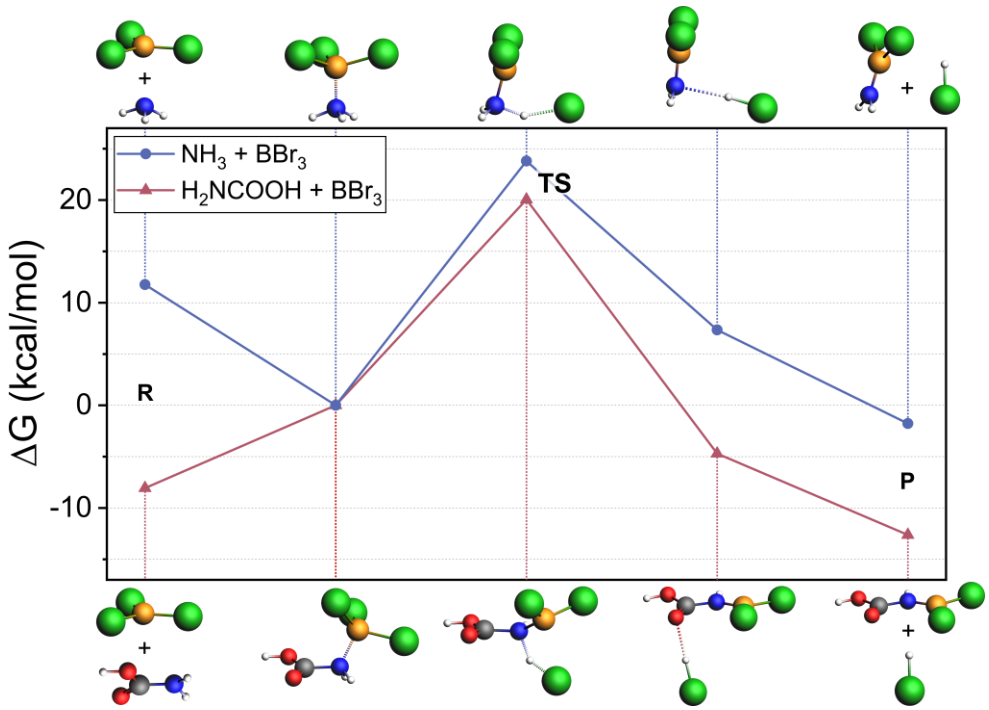

Figure 7.9. Evolution of the Gibbs energy differences (ΔG) of the reactions $H_2NCOOH+BBr_3 \rightarrow Br_2BNHCOOH+BrH$ and $NH_3+BBr_3 \rightarrow H_2NBBr_2+BrH$. The corresponding structures of the initial reagents (R), intermediate complexes, transition states (TS), and final products (P) are shown above (NH_3+BBr_3) and below ($H_2NCOOH+BBr_3$) the graph.

In the first reaction step, the initial reagents (R), NH_3 and BBr_3, and H_2NCOOH and BBr_3, are separate and do not interact with each other. In the next step, the pre-reaction complexes are formed as the reagents come closer together and start to interact, forming weak B···N bonds. The distance between the B and N atoms bonded is 1.611 Å for $NH_3\cdots BBr_3$ and 1.673 Å for $H_2NCOOH\cdots BBr_3$. Next, the pre-reaction complexes pass through the transition states (TS), transient, unstable molecular configurations with a higher energy. These states correspond to the peak of the energy barrier and are the rate-limiting steps of the model reactions. Once they are passed, the post-reaction complexes, with short, strong B-N

bonds are formed, with distances of 1.395 Å for the H_2NBBr_2···BrH complex and 1.422 Å for the $Br_2BNHCOOH$···BrH one. Lastly, the reactions are completed when the post-reaction complexes decompose into the reaction products (P), which are H_2NBBr_2 and BrH, and $Br_2BNCOOH$ and BrH, respectively. The lower Gibbs energy of the TS of the reaction of BBr_3 with carbamic acid confirms that it is energetically more favorable than the corresponding reaction with ammonia.

To quantitatively study this difference, the transition state theory equation (**Equation 7.1**) was used to calculate the reaction rate constants k of the model reactions at 100°C:

$$k = \frac{k_B T}{h} e^{-\frac{\Delta G}{RT}} \tag{7.1}$$

where k_B is the Boltzmann constant, T is the temperature, h is Planck's constant, ΔG is the Gibbs free energy of activation between the reactants and the transition state and R is the ideal gas constant.

The obtained rate constants are 0.0895 Hz for the reaction of NH_3 with BBr_3 and 14.0566 Hz for the reaction of H_2NCOOH with BBr_3, proving that the proposed reaction with ammonium carbamate is 157 faster than the corresponding reaction with ammonia at 100°C, thereby enabling low temperature deposition of BN.

7.5. Conclusions

A new process for the low temperature growth of amorphous boron nitride by ALD using ammonium carbamate as the nitrogen source was developed.

The self-limiting nature of the reactions and constant GPC characteristic of ALD processes were demonstrated within the studied temperature range and film growth was achieved at temperatures as low as 100°C. The GPC of the process is approximately 0.5 Å/cycle between 150 and 250°C. A lower GPC was observed during the first deposition cycles, until the substrate surface is fully covered with BN. The deposition was performed successfully on various substrates.

The composition and structure of the as-deposited material were characterized by XPS and EELS. Boron and nitrogen atoms were found bound to each other through sp^2 hybridization and with the expected 1:1 stoichiometry of BN. Carbon and oxygen atoms are additionally found in the sample. The carbon atoms are expected to stem from precursor imperfections and substitute both B and N. Oxygen atoms are more likely to be due to post-deposition air exposure. The BN grown has an amorphous structure, as confirmed by Raman spectroscopy and XRD.

Computational modeling showed that the rate limiting step of the reaction between carbamic acid and boron tribromide is more energetically favorable and proceeds 157 times faster than the corresponding reaction between ammonia and boron tribromide. These results support the hypothesis that carbamic acid, formed as an intermediate species during the decomposition of ammonium carbamate, is the enabler of the lowering of the deposition temperature.

With this process, ammonium carbamate is introduced as a promising nitrogen precursor for the ALD of nitrides. This approach eliminates the direct handling of hazardous nitrogen precursors, such as ammonia, making laboratory work safer and more convenient. Simultaneously, the lower deposition temperatures allow the application of nitride ALD to thermally sensitive substrates, even toward polymers. This combination gives new prospects for the deposition of a variety of nitride materials and expands their potential applications.

8

Summary of complementary industrial work

This chapter presents a brief summary of the additional work carried out as part of the company CTECHnano Coating Technologies S.L. in the framework of an industrial PhD. The activities described were conducted in an industrial setting, in parallel with the academic research presented in this thesis and provide insights into the connection between fundamental research and its practical implementation. This complementary work focused on addressing specific industrial needs, contributing to product development, process optimization and characterization of materials grown by ALD and VPI for real-world applications. The work also included communication with clients and provision of technical services related to the ALD reactors manufactured by the company.

Certain details of the work described in this chapter cannot be disclosed as they involve confidential information and protected intellectual property of the customers.

The following sections outline the main tasks performed during the PhD, including client services, participation in research and innovation projects, and other industrial responsibilities.

8.1. Client services

Client services refer to projects carried out upon request from external companies, in which samples are prepared and delivered according to

specific requirements defined by the client. These services typically involve the application of established deposition or infiltration processes, occasionally adapted to meet particular material specifications. In some cases, they also include process development for the deposition of a specific material or additional in-house characterization to ensure that the final samples meet the intended specifications.

A typical service began with a discussion in which the client either requested the deposition of a specific material or described the desired properties, after which we proposed suitable material options to meet their needs. If the requested deposition process was not already established or had not been previously carried out in our reactors, a bibliography and precursor search was conducted, followed by process testing and optimization. The prepared samples were routinely characterized by X-ray reflectivity to verify successful deposition of a film with the desired thickness, and by SEM and EDX to assess film quality and provide elemental analysis. In some cases, additional characterization was performed prior to delivery, including various electrical measurements, X-ray diffraction, atomic force microscopy measurements, Raman, IR, and UV-Visible spectroscopies, as well as permeability tests. Some of these services were recurring, consisting of regular preparation and weekly delivery of samples.

A summary of the client services carried out during my industrial collaboration with CTECHnano Coating Technologies S.L. is presented in **Table 8.1**. Materials which involved process development are underlined, and services which included additional in-house characterization are marked with an asterisk (*).

Materials	Substrates	Applications
Al_2O_3	SiO_2 wafers Silver Wax Stone Macroporous silicon PET Polyimide*	Electronic devices Semiconductors Jewelry Cultural heritage Photonics Neuroelectronics
TiO_2	Macroporous silicon	Photonics
HfO_2	SiO_2 wafers*	Electronic devices
SiO_2	SiO_2 wafers Macroporous silicon*	Semiconductors Photonics
Al_2O_3/TiO_2 bilayer	Silver	Jewelry
HfO_2/Al_2O_3 bilayer	SiO_2 wafers	Electronic devices
HfO_2/SiO_2 bilayer	Glass	Optics
Alumina-doped ZnO (AZO)	Silver Wax PET*	Semiconductors Jewelry
FeO_x	Macroporous silicon*	Photonics
Si_3N_4	Macroporous silicon	Photonics
PbTe	Macroporous silicon	Photonics

Table 8.1. Summary of the client services performed within the company. Materials which involved process development are underlined and services which included additional in-house characterization are marked with an asterisk (*).

8.2. Research and innovation projects

Research and innovation projects at CTECHnano Coating Technologies S.L. are internally developed investigation initiatives aimed at advancing the company's technological capabilities and expanding the potential commercial applications of ALD and VPI. These projects involve collaboration between the industrial and academic sectors, focusing on applying fundamental research to potential real-world applications which allow the development of new client service lines.

The projects presented here are mainly based on processes which are already established in the industry, utilizing relatively inexpensive and readily available precursors, but applied in novel fields. The development of a research and innovation project consists of an initial literature review to analyze the state of the art of the target application field and identify the potential contributions of ALD and VPI to it. Then, the chosen deposition process was adapted to the requirement of each substrate and optimized. The prepared samples were characterized according to their intended application to study the influence of deposition parameters on their performance.

These projects were the main link between the scientific research on multifunctional fibers and the industrial work presented in this thesis, transferring the insights obtained from one research context to the other. Furthermore, the knowledge obtained about the use of VPI for the preparation of multifunctional fibers contributed to the opening of a new service line within the company.

A summary of the research and innovation projects and the specific tasks carried out for their development is presented in **Table 8.2**.

Project	Research	Applications
Functionalization of delignified wood through VPI	• Wood delignification • Infiltration of different metal oxides (Al_2O_3, TiO_2, HfO_2, SiO_2, ZnO) • Mechanical pressing • Transmittance measurements	Manufacturing of transparent wood
UV-protective ALD coating of sustainable materials *(In collaboration with the University of Minho)*	• Coating of cork and rubber with Al_2O_3, TiO_2 and ZnO • Cork particles were coated in a fluidized bed reactor (FBR) • Pieces of rubber of different colorations were coated in a PLAY reactor • Simulated sunlight exposure and damage assessment	Reduction of aging and degradation of cork and rubber when exposed to sunlight
ALD coating of seeds	• Lentil seeds coated with ZnO in a fluidized bed reactor (FBR) • Study of the effect on germination under different conditions (illumination, water quantity and acidity, ventilation)	Protection of the seeds and stimulated growth through nutrient and water supply

Table 8.2. Summary of the research and innovation projects developed in the company.

8.3. Other activities

- Optimization and validation of a new ALD reactor prototype with an adjustable volume chamber. The developed ALD reactor prototype allows selecting between three operational volumes through the placement of separators into the chamber as shown in **Figure 8.1**. The deposition of Al_2O_3 and ZnO at varying process temperatures was used to validate the performance of the prototype in each volume configuration, attending to uniformity and reproducibility. A user manual and standard recipes for the reactor were prepared.

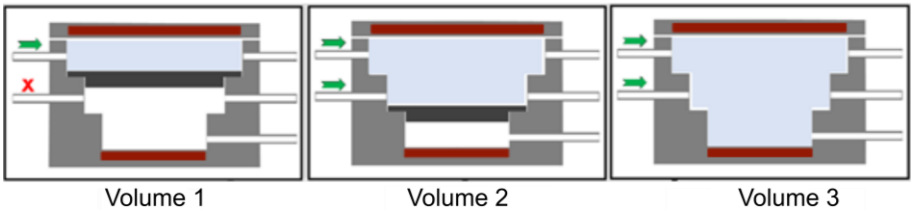

Figure 8.1. Schematics of the three possible operational volumes of the ALD reactor.

- Involvement in the design of a new fluidized bed reactor (FBR). The company had an initial FBR prototype which was modified in order to enhance its performance. This work included vacuum and evacuation tests to analyze different chamber configurations, verifying the fluidization of different particles and the addition of inlet lines.

Figure 8.2. Picture and control schematics of the designed FBR.

- Testing of a new plasma reactor for Plasma-Enhanced Atomic Layer Deposition (PEALD). To incorporate a plasma source into the existing PLAY ALD reactor, an alternative lid with 4 electronic cyclotron resonance (ECR) microwave coaxial heads was used. A metal ring was added to the set-up to increase the height of the chamber and facilitate the uniform production of plasma. The generation of plasma of different gases was tested and preliminarily applied to ALD processes.

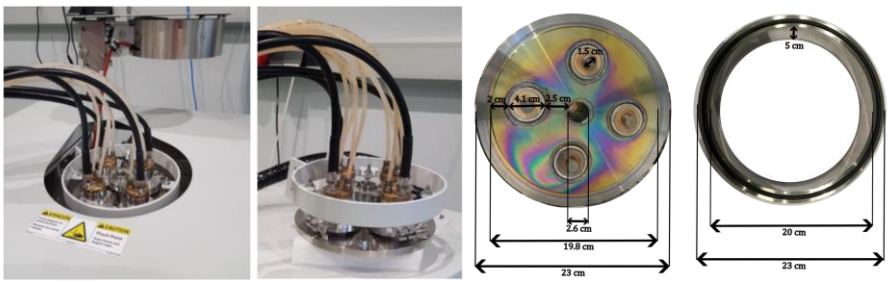

Figure 8.3. Pictures and measurement schematics of the plasma head accessory.

- Installation and testing of an ozone generator. Different values of the oxygen flow and ozone concentrations were tested in ALD processes.
- Installation and maintenance of ALD reactors. Including leak checking, vacuum system conservation, replacement and/or reconditioning of deteriorated components, and troubleshooting of deposition irregularities.
- Technical support for clients

References

[1] V. Postrel, *The Fabric of Civilization: How Textiles Made the World*. 2020.

[2] D. Paret and P. Crégo, *Wearables, Smart Textiles and Smart Apparel*. ISTE Press - Elsevier, 2019.

[3] K. Ashurbekova, K. Ashurbekova, G. Botta, O. Yurkevich, M. Knez, and M. Knez, "Vapor phase processing: A novel approach for fabricating functional hybrid materials," *Nanotechnology*, vol. 31, no. 34, 2020, doi: 10.1088/1361-6528/ab8edb.

[4] P. Gomez-Romero, A. Pokhriyal, D. Rueda-García, L. N. Bengoa, and R. M. González-Gil, "Hybrid Materials: A Metareview," Jan. 09, 2024, *American Chemical Society*. doi: 10.1021/acs.chemmater.3c01878.

[5] K. Gregorczyk and M. Knez, "Hybrid nanomaterials through molecular and atomic layer deposition: Top down, bottom up, and in-between approaches to new materials," Jan. 01, 2016, *Elsevier Ltd*. doi: 10.1016/j.pmatsci.2015.06.004.

[6] H. Berke, "The invention of blue and purple pigments in ancient times," *Chem Soc Rev*, vol. 36, no. 1, pp. 15–30, Dec. 2006, doi: 10.1039/B606268G.

[7] M. Faustini, L. Nicole, E. Ruiz-Hitzky, and C. Sanchez, "History of Organic–Inorganic Hybrid Materials: Prehistory, Art, Science, and Advanced Applications," Jul. 04, 2018, *Wiley-VCH Verlag*. doi: 10.1002/adfm.201704158.

[8] "Stock Photo Conch Shell mother-of-pearl-1 | Adobe Stock." Accessed: Sep. 10, 2025. [Online]. Available: https://stock.adobe.com/es/images/conch-shell-mother-of-pearl-1/7802906

[9] "African Elephant in savanna. Close up. Masai Mara National Park.... News Photo - Getty Images." Accessed: Sep. 10, 2025. [Online]. Available: https://www.gettyimages.fi/detail/uutiskuva/african-elephant-in-savanna-close-up-masai-mara-national-uutiskuva/1277563693?adppopup=true

[10] "Stylized Anatomy of the human Femur stock photo - iStock." Accessed: Sep. 10, 2025. [Online]. Available: https://www.istockphoto.com/es/foto/anatom%C3%ADa-estilizada-del-f%C3%A9mur-humano-gm1166831165-321570915

[11] L. Pelayo Alonso, "Altamira," *World History Encyclopedia*, Dec. 2015, Accessed: Sep. 10, 2025. [Online]. Available: https://www.worldhistory.org/trans/es/1-11600/altamira/

[12] "Aztec Plate stock photo - iStock." Accessed: Sep. 10, 2025. [Online]. Available: https://www.istockphoto.com/es/foto/placa-aztec-gm146782214-11723375

[13] L. A. Belfiore, P. Das, and F. Bossé, “Synergistic mechanical response in blends of diene polymers and their complexes with palladium chloride,” *J Polym Sci B Polym Phys*, vol. 34, no. 16, pp. 2675–2687, Sep. 1996, doi: 10.1002/(SICI)1099-0488(19961130)34:16<2675::AID-POLB1>3.0.CO;2-P.

[14] Y. Zhang *et al.*, “Functional Textiles with Smart Properties: Their Fabrications and Sustainable Applications,” Aug. 15, 2023, *John Wiley and Sons Inc*. doi: 10.1002/adfm.202301607.

[15] D. Sanders, A. Grunden, and R. R. Dunn, “A review of clothing microbiology: The history of clothing and the role of microbes in textiles,” Jan. 01, 2021, *Royal Society Publishing*. doi: 10.1098/rsbl.2020.0700.

[16] M. K. Singh and M. K. Singh, “Textiles Functionalization - A Review of Materials, Processes, and Assessment,” *Textiles for Functional Applications*, Apr. 2021, doi: 10.5772/INTECHOPEN.96936.

[17] S. Omar and A. Goel, “Hybrid Textiles: A Review.” [Online]. Available: https://www.researchgate.net/publication/267155270

[18] S. Lee, “Polypyrrole-wool composite with electrical heating properties fabricated via layer-by-layer method,” *Sci Rep*, vol. 14, no. 1, pp. 1–13, Dec. 2024, doi: 10.1038/S41598-024-54678-6;SUBJMETA=301,357,403,638,639,923;KWRD=NANOSCALE+MATERIALS,ORGANIC+CHEMISTRY,SOFT+MATERIALS.

[19] L. Abilevitch *et al.*, “Polyaniline for Smart Textile Applications,” *Trends and Developments in Modern Applications of Polyaniline*, Aug. 2023, doi: 10.5772/INTECHOPEN.1001939.

[20] C. Chen, D. Weng, A. Mahmood, S. Chen, and J. Wang, “Separation Mechanism and Construction of Surfaces with Special Wettability for Oil/Water Separation,” *ACS Appl Mater Interfaces*, vol. 11, no. 11, pp. 11006–11027, 2019, doi: 10.1021/acsami.9b01293.

[21] S. J. Sbai, A. Boukhriss, S. Majid, and S. Gmouh, “The recent advances in nanotechnologies for textile functionalization,” in *Advances in Functional and Protective Textiles*, Elsevier, 2020, pp. 531–568. doi: 10.1016/b978-0-12-820257-9.00020-5.

[22] P. J. Rivero, A. Urrutia, J. Goicoechea, and F. J. Arregui, “Nanomaterials for Functional Textiles and Fibers,” Dec. 01, 2015, *Springer New York LLC*. doi: 10.1186/s11671-015-1195-6.

[23] “Nanoscale ceramic surface modification of textiles by atomic layer deposition.” [Online]. Available: www.ceramics.org

[24] I. Azpitarte and M. Knez, “Vapor phase infiltration: From a bioinspired process to technologic application, a prospective review,” *MRS Commun*, vol. 8, no. 3, pp. 727–741, 2018, doi: 10.1557/mrc.2018.126.

[25] S. M. Lee *et al.*, “Greatly increased toughness of infiltrated spider silk,” *Science (1979)*, vol. 324, no. 5926, pp. 488–492, Apr. 2009, doi: 10.1126/SCIENCE.1168162,.

[26] C. Z. Leng and M. D. Losego, “Vapor phase infiltration (VPI) for transforming polymers into organic-inorganic hybrid materials: A critical review of current progress and future challenges,” *Mater Horiz*, vol. 4, no. 5, pp. 747–771, 2017, doi: 10.1039/c7mh00196g.

[27] M. D. Losego and Q. Peng, “Atomic layer deposition and vapor phase infiltration,” *Surface Modification of Polymers: Methods and Applications*, pp. 135–159, 2019, doi: 10.1002/9783527819249.ch5.

[28] S. V. Gudkov, D. E. Burmistrov, D. A. Serov, M. B. Rebezov, A. A. Semenova, and A. B. Lisitsyn, “A Mini Review of Antibacterial Properties of ZnO Nanoparticles,” *Front Phys*, vol. 9, no. March, pp. 1–12, 2021, doi: 10.3389/fphy.2021.641481.

[29] D. A. Karajz and I. M. Szilágyi, “Review of photocatalytic ZnO nanomaterials made by atomic layer deposition,” Aug. 01, 2023, *Elsevier B.V.* doi: 10.1016/j.surfin.2023.103094.

[30] L. Budama, Ö. Topel, and N. Hoda, “Synthesis of ZnO nanoparticles using PS-b-PAA reverse micelle cores for UV protective , self-cleaning and antibacterial textile applications,” vol. 414, pp. 132–139, 2012, doi: 10.1016/j.colsurfa.2012.08.015.

[31] Q. F. Sun, Y. Lu, Y. Z. Xia, D. J. Yang, J. Li, and Y. X. Liu, “Flame retardancy of wood treated by TiO2/ZnO coating,” *Surface Engineering*, vol. 28, no. 8, pp. 555–559, Sep. 2012, doi: 10.1179/1743294412Y.0000000027.

[32] M. J. Torralvo *et al.*, “Anatase photocatalyst with supported low crystalline TiO2: The influence of amorphous phase on the activity,” *Appl Catal B*, vol. 221, no. August 2017, pp. 140–151, 2018, doi: 10.1016/j.apcatb.2017.08.089.

[33] S. Sun, P. Song, J. Cui, and S. Liang, “Amorphous TiO2 nanostructures: Synthesis, fundamental properties and photocatalytic applications,” *Catal Sci Technol*, vol. 9, no. 16, pp. 4198–4215, 2019, doi: 10.1039/c9cy01020c.

[34] S. Banerjee, D. D. Dionysiou, and S. C. Pillai, “Self-cleaning applications of TiO2 by photo-induced hydrophilicity and photocatalysis,” *Appl Catal B*, vol. 176–177, pp. 396–428, Oct. 2015, doi: 10.1016/j.apcatb.2015.03.058.

[35] L. Liu, R. Bhatia, and T. J. Webster, “Atomic layer deposition of nano-TiO2 thin films with enhanced biocompatibility and antimicrobial activity for orthopedic

implants," *Int J Nanomedicine*, vol. 12, pp. 8711–8723, 2017, doi: 10.2147/IJN.S148065.

[36] "Scanning Electron Microscopy | Electrons in SEM | Thermo Fisher Scientific - ES." Accessed: Jul. 23, 2025. [Online]. Available: https://www.thermofisher.com/es/es/home/materials-science/learning-center/applications/sem-electrons.html

[37] "SEM working principle: the detection of backscattered electrons | Thermo Fisher Scientific - ES." Accessed: Jul. 23, 2025. [Online]. Available: https://www.thermofisher.com/es/es/home/global/forms/industrial/backscattered-electrons-sem.html

[38] H. Günzler and H. Gremlich, "IR-Spektroskopie," *IR-Spektroskopie*, May 2003, doi: 10.1002/9783527662852.

[39] "What Is ICP-OES? Principles & Technique | Agilent." Accessed: Jul. 23, 2025. [Online]. Available: https://www.agilent.com/en/support/atomic-spectroscopy/inductively-coupled-plasma-optical-emission-spectroscopy-icp-oes/icp-oes-faq

[40] Y. Waseda, E. Matsubara, and K. Shinoda, *X-Ray Diffraction Crystallography*. Springer Berlin Heidelberg, 2011. doi: 10.1007/978-3-642-16635-8/COVER.

[41] "ISO 13934-1:2013 - Textiles — Tensile properties of fabrics — Part 1: Determination of maximum force and elongation at maximum force using the strip method." Accessed: Jul. 23, 2025. [Online]. Available: https://www.iso.org/standard/60676.html

[42] G. Gauglitz, "Ultraviolet and Visible Spectroscopy," in *Handbook of Analytical Techniques*, vol. 1–2, John Wiley & Sons, Ltd, 2008, pp. 419–463. doi: 10.1002/9783527618323.CH16.

[43] P. Makuła, M. Pacia, and W. Macyk, "How To Correctly Determine the Band Gap Energy of Modified Semiconductor Photocatalysts Based on UV-Vis Spectra," *Journal of Physical Chemistry Letters*, vol. 9, no. 23, pp. 6814–6817, Dec. 2018, doi: 10.1021/ACS.JPCLETT.8B02892/SUPPL_FILE/JZ8B02892_LIVESLIDES.MP4.

[44] "Contact angle | KRÜSS Scientific." Accessed: Sep. 12, 2025. [Online]. Available: https://www.kruss-scientific.com/en/know-how/glossary/contact-angle

[45] "ISO 62:2008 - Plastics — Determination of water absorption." Accessed: Jul. 23, 2025. [Online]. Available: https://www.iso.org/standard/41672.html

[46] A. Arputharaj, V. Nadanathangam, and S. R. Shukla, "A simple and efficient protocol to develop durable multifunctional property to cellulosic materials using in situ generated nano-ZnO," *Cellulose*, vol. 24, no. 8, pp. 3399–3410, Aug. 2017, doi: 10.1007/s10570-017-1335-5.

[47] “What is a Spectrophotometer? - Principle, Types, Uses, and Benefits.” Accessed: Sep. 12, 2025. [Online]. Available: https://www.testronixinstruments.com/blog/what-does-spectrophotometer-measures/

[48] R. L. Long, M. P. Bange, S. G. Gordon, and G. A. Constable, “Measuring the Maturity of Developing Cotton Fibers using an Automated Polarized Light Microscopy Technique,” *Textile Research Journal*, vol. 80, no. 5, pp. 463–471, 2010, doi: 10.1177/0040517509343784.

[49] “Polyethylene wax – Database of ATR-FT-IR spectra of various materials.” Accessed: Jun. 13, 2025. [Online]. Available: https://spectra.chem.ut.ee/paint/binders/polyethylene-wax/

[50] “Cotton – Database of ATR-FT-IR spectra of various materials.” Accessed: Jun. 13, 2025. [Online]. Available: https://spectra.chem.ut.ee/textile-fibres/cotton/

[51] “Periodic Table of Elements | EDAX.” Accessed: Jun. 13, 2025. [Online]. Available: https://www.edax.com/resources/periodic-table

[52] “ICP Periodic Table Guide”.

[53] J. Malm, E. Sahramo, J. Perälä, T. Sajavaara, and M. Karppinen, “Low-temperature atomic layer deposition of ZnO thin films: Control of crystallinity and orientation,” *Thin Solid Films*, vol. 519, no. 16, pp. 5319–5322, Jun. 2011, doi: 10.1016/J.TSF.2011.02.024.

[54] J. Aarik, A. Aidla, H. Mändar, and T. Uustare, “Atomic layer deposition of titanium dioxide from TiCl4 and H2O: investigation of growth mechanism,” *Appl Surf Sci*, vol. 172, no. 1–2, pp. 148–158, Mar. 2001, doi: 10.1016/S0169-4332(00)00842-4.

[55] J. Albertsson, S. C. Abrahams, and A. Kvick, “Atomic displacement, anharmonic thermal vibration, expansivity and pyroelectric coefficient thermal dependences in ZnO,” vol. 45, no. 1, pp. 34–40, Feb. 1989, Accessed: Jun. 13, 2025. [Online]. Available: https://inis.iaea.org/records/58jsa-h1117

[56] Y. Nishiyama, P. Langan, and H. Chanzy, “Crystal structure and hydrogen-bonding system in cellulose Iβ from synchrotron X-ray and neutron fiber diffraction,” *J Am Chem Soc*, vol. 124, no. 31, pp. 9074–9082, Aug. 2002, doi: 10.1021/JA0257319/SUPPL_FILE/JA0257319_S1.CIF.

[57] F. Kayaci, S. Vempati, I. Donmez, N. Biyikli, and T. Uyar, “Role of zinc interstitials and oxygen vacancies of ZnO in photocatalysis: a bottom-up approach to control defect density,” *Nanoscale*, vol. 6, no. 17, pp. 10224–10234, Aug. 2014, doi: 10.1039/C4NR01887G.

[58] “ISO 13934-1:2013 - Textiles — Tensile properties of fabrics — Part 1: Determination of maximum force and elongation at maximum force using the strip method.” Accessed: Jun. 13, 2025. [Online]. Available: https://www.iso.org/standard/60676.html

[59] D. Srivastava, M. S. Kuklin, J. Ahopelto, and A. J. Karttunen, “Electronic band structures of pristine and chemically modified cellulose allomorphs,” *Carbohydr Polym*, vol. 243, p. 116440, Sep. 2020, doi: 10.1016/J.CARBPOL.2020.116440.

[60] L. Chen, T. D. Huan, and R. Ramprasad, “Electronic Structure of Polyethylene: Role of Chemical, Morphological and Interfacial Complexity,” *Sci Rep*, vol. 7, no. 1, pp. 1–10, Dec. 2017, doi: 10.1038/S41598-017-06357-Y;TECHMETA=118,119;SUBJMETA=1005,1007,1034,1038,301,639;KWRD=ELECTRONIC+DEVICES,ELECTRONIC+STRUCTURE.

[61] P. Makuła, M. Pacia, and W. Macyk, “How To Correctly Determine the Band Gap Energy of Modified Semiconductor Photocatalysts Based on UV-Vis Spectra,” *Journal of Physical Chemistry Letters*, vol. 9, no. 23, pp. 6814–6817, Dec. 2018, doi: 10.1021/ACS.JPCLETT.8B02892/SUPPL_FILE/JZ8B02892_LIVESLIDES.MP4.

[62] A. Mang, K. Reimann, and S. Rübenacke, “Band gaps, crystal-field splitting, spin-orbit coupling, and exciton binding energies in ZnO under hydrostatic pressure,” *Solid State Commun*, vol. 94, no. 4, pp. 251–254, Apr. 1995, doi: 10.1016/0038-1098(95)00054-2.

[63] H. Tang, H. Berger, P. E. Schmid, F. Lévy, and G. Burri, “Photoluminescence in TiO2 anatase single crystals,” *Solid State Commun*, vol. 87, no. 9, pp. 847–850, Sep. 1993, doi: 10.1016/0038-1098(93)90427-O.

[64] R. M. Sayre, C. Cole, W. Billhimer, J. Stanfield, and R. D. Ley, “Spectral comparison of solar simulators and sunlight.,” *Photodermatol Photoimmunol Photomed*, vol. 7, no. 4, pp. 159–165, Aug. 1990, Accessed: Aug. 01, 2025. [Online]. Available: https://europepmc.org/article/med/2076371

[65] Q. Mushtaq, T. Awan, M. Momna, M. Amjad, A. Intisar, and A. Afzal, “Sustainable self-cleaning fabrics enabled by sunlit metal oxide catalysts: A critical review,” *Sustainable Materials and Technologies*, vol. 41, p. e01009, Sep. 2024, doi: 10.1016/J.SUSMAT.2024.E01009.

[66] W. S. Tung and W. A. Daoud, “Self-cleaning fibers via nanotechnology: A virtual reality,” *J Mater Chem*, vol. 21, no. 22, pp. 7858–7869, 2011, doi: 10.1039/c0jm03856c.

[67] E. Pakdel, J. Wang, S. Kashi, L. Sun, and X. Wang, “Advances in photocatalytic self-cleaning, superhydrophobic and electromagnetic interference shielding textile treatments,” *Adv Colloid Interface Sci*, vol. 277, p. 102116, Mar. 2020, doi: 10.1016/J.CIS.2020.102116.

[68] A. Baddouh *et al.*, "Electrochemical decolorization of Rhodamine B dye: Influence of anode material, chloride concentration and current density," *J Environ Chem Eng*, vol. 6, no. 2, pp. 2041–2047, Apr. 2018, doi: 10.1016/J.JECE.2018.03.007.

[69] B. Ohtani, "Photocatalysis by inorganic solid materials: Revisiting its definition, concepts, and experimental procedures," *Adv Inorg Chem*, vol. 63, pp. 395–430, Jan. 2011, doi: 10.1016/B978-0-12-385904-4.00001-9.

[70] A. Di Mauro, M. Cantarella, G. Nicotra, V. Privitera, and G. Impellizzeri, "Low temperature atomic layer deposition of ZnO: Applications in photocatalysis," *Appl Catal B*, vol. 196, pp. 68–76, Nov. 2016, doi: 10.1016/j.apcatb.2016.05.015.

[71] S.-M. Lee *et al.*, "Low-temperature ZnO atomic layer deposition on biotemplates: flexible photocatalytic ZnO structures from eggshell membranes," *Physical Chemistry Chemical Physics*, vol. 11, no. 19, p. 3607, 2009, doi: 10.1039/b905768d.

[72] E. Guziewicz *et al.*, "Extremely low temperature growth of ZnO by atomic layer deposition," *J Appl Phys*, vol. 103, no. 3, Feb. 2008, doi: 10.1063/1.2836819/902340.

[73] J. H. Zeng, B. Bin Jin, and Y. F. Wang, "Facet enhanced photocatalytic effect with uniform single-crystalline zinc oxide nanodisks," *Chem Phys Lett*, vol. 472, no. 1–3, pp. 90–95, Apr. 2009, doi: 10.1016/J.CPLETT.2009.02.082.

[74] A. Bozzi, T. Yuranova, and J. Kiwi, "Self-cleaning of wool-polyamide and polyester textiles by TiO2-rutile modification under daylight irradiation at ambient temperature," *J Photochem Photobiol A Chem*, vol. 172, no. 1, pp. 27–34, May 2005, doi: 10.1016/J.JPHOTOCHEM.2004.11.010.

[75] W. A. Daoud, J. H. Xin, and Y. H. Zhang, "Surface functionalization of cellulose fibers with titanium dioxide nanoparticles and their combined bactericidal activities," *Surf Sci*, vol. 599, no. 1–3, pp. 69–75, Dec. 2005, doi: 10.1016/J.SUSC.2005.09.038.

[76] N. Abidi, L. Cabrales, and E. Hequet, "Functionalization of a cotton fabric surface with titania nanosols: Applications for self-cleaning and UV-protection properties," *ACS Appl Mater Interfaces*, vol. 1, no. 10, pp. 2141–2146, Oct. 2009, doi: 10.1021/AM900315T/ASSET/IMAGES/MEDIUM/AM-2009-00315T_0011.GIF.

[77] W. A. Daoud, J. H. Xin, Y. H. Zhang, and K. Qi, "Surface characterization of thin titania films prepared at low temperatures," *J Non Cryst Solids*, vol. 351, no. 16–17, pp. 1486–1490, Jun. 2005, doi: 10.1016/J.JNONCRYSOL.2005.03.036.

[78] H. Yu, S. C. Lee, J. Yu, and C. H. Ao, "Photocatalytic activity of dispersed TiO2 particles deposited on glass fibers," *J Mol Catal A Chem*, vol. 246, no. 1–2, pp. 206–211, Mar. 2006, doi: 10.1016/J.MOLCATA.2005.11.007.

[79] H. J. Ensikat, P. Ditsche-Kuru, C. Neinhuis, and W. Barthlott, "Superhydrophobicity in perfection: the outstanding properties of the lotus leaf," *Beilstein Journal of Nanotechnology 2:19*, vol. 2, no. 1, pp. 152–161, Mar. 2011, doi: 10.3762/BJNANO.2.19.

[80] Y. Gao and R. Cranston, "Recent Advances in Antimicrobial Treatments of Textiles," *Textile Research Journal*, vol. 78, no. 1, pp. 60–72, 2008, doi: 10.1177/0040517507082332.

[81] R. Gulati, S. Sharma, and R. K. Sharma, "Antimicrobial textile: recent developments and functional perspective," Aug. 01, 2022, *Springer Science and Business Media Deutschland GmbH*. doi: 10.1007/s00289-021-03826-3.

[82] "ISO 22196:2011 - Measurement of antibacterial activity on plastics and other non-porous surfaces." Accessed: Aug. 01, 2025. [Online]. Available: https://www.iso.org/standard/54431.html

[83] R. D. Boyd, J. Verran, M. V. Jones, and M. Bhakoo, "Use of the atomic force microscope to determine the effect of substratum surface topography on bacterial adhesion," *Langmuir*, vol. 18, no. 6, pp. 2343–2346, Mar. 2002, doi: 10.1021/la011142p.

[84] E. T. J. Rochford, R. G. Richards, and T. F. Moriarty, "Influence of material on the development of device-associated infections," 2012, *Blackwell Publishing Ltd*. doi: 10.1111/j.1469-0691.2012.04002.x.

[85] Z. Breijyeh, B. Jubeh, and R. Karaman, "Resistance of Gram-Negative Bacteria to Current Antibacterial Agents and Approaches to Resolve It," *Molecules*, vol. 25, no. 6, p. 1340, Mar. 2020, doi: 10.3390/MOLECULES25061340.

[86] "Microbial Origins of Body Odor." Accessed: Aug. 01, 2025. [Online]. Available: https://asm.org/articles/2021/december/microbial-origins-of-body-odor

[87] S. Alibi *et al.*, "Occurrence of Corynebacterium striatum as an emerging antibiotic-resistant nosocomial pathogen in a Tunisian hospital," *Sci Rep*, vol. 7, no. 1, p. 9704, Dec. 2017, doi: 10.1038/S41598-017-10081-Y.

[88] Â. Pinheiro, D. Piontkivska, P. Sequeira, T. M. Martins, and C. Silva Pereira, "Aspergillus nidulans," Feb. 01, 2023, *Elsevier Ltd*. doi: 10.1016/j.tim.2022.09.013.

[89] Q. Sun, J. Li, and T. Le, "Zinc Oxide Nanoparticle as a Novel Class of Antifungal Agents: Current Advances and Future Perspectives," *J Agric Food Chem*, vol. 66, no. 43, pp. 11209–11220, 2018, doi: 10.1021/acs.jafc.8b03210.

[90] G. Steinberg, "Hyphal Growth: a Tale of Motors, Lipids, and the Spitzenkörper," *Eukaryot Cell*, vol. 6, no. 3, p. 351, Mar. 2007, doi: 10.1128/EC.00381-06.

[91] S. Basak, A. Laha, M. Bar, and R. Roy, “3 Recent Advances in Protective Textile Materials,” 2018.

[92] A. Verbič, M. Gorjanc, and B. Simončič, “Zinc oxide for functional textile coatings: Recent advances,” Sep. 01, 2019, *MDPI AG*. doi: 10.3390/coatings9090550.

[93] “Defining and Communicating Color: The CIELAB System,” 2013.

[94] “LAB Espacio de color y valores | Blog del color X-Rite.” Accessed: May 05, 2025. [Online]. Available: https://www.xrite.com/blog/lab-color-space

[95] “La tolerancia del color para asegurar precisión | X-Rite.” Accessed: May 05, 2025. [Online]. Available: https://www.xrite.com/blog/tolerancing-part-3

[96] Datacolor, “The fundamentals of colorimetry. Color and color measurement.,” no. Book 4, 2017, ch. Color management.

[97] A. Martin, *Colour Management in the Graphic Technologies*. BCcampus, 2015.

[98] “Specular Component Included (SCI) vs. Specular Component Excluded (SCE).” Accessed: May 05, 2025. [Online]. Available: https://sensing.konicaminolta.us/us/blog/specular-component-included-sci-vs-specular-component-excluded-sce/

[99] C. Sinkinson, “Triangle Test,” in *Discrimination Testing in Sensory Science*, Elsevier, 2017, pp. 153–170. doi: 10.1016/B978-0-08-101009-9.00007-1.

[100] *BS ISO 4120:2004. Sensory analysis-Methodology-Triangle test.* 2004.

[101] M. O’Mahony, “Who told you the triangle test was simple?,” *Food Qual Prefer*, vol. 6, no. 4, pp. 227–238, 1995.

[102] World Medical Association, “World Medical Association Declaration of Helsinki: Ethical Principles for Medical Research Involving Human Subjects,” *JAMA*, vol. 310, no. 20, pp. 2191–2194, Nov. 2013, doi: 10.1001/JAMA.2013.281053.

[103] P. Schlich, “Risk tables for discrimination tests,” *Food Qual Prefer*, vol. 4, no. 3, pp. 141–151, 1993.

[104] P. Potluri, J. Atkinson, and I. Porat, “Large Deformation Modelling of Flexible Materials,” *Journal of the Textile Institute*, vol. 87, no. 1, pp. 129–151, 1996, doi: 10.1080/00405009608659062.

[105] L. C. Gerhardt, V. Strässle, A. Lenz, N. D. Spencer, and S. Derler, “Influence of epidermal hydration on the friction of human skin against textiles,” *J R Soc Interface*, vol. 5, no. 28, p. 1317, Nov. 2008, doi: 10.1098/RSIF.2008.0034.

[106] “Corneometer® CM 825 - Skin Hydration Measurement.” Accessed: Jul. 01, 2025. [Online]. Available: https://www.courage-khazaka.com/en/scientific-products/corneometer-cm-825

[107] T. J. Flack, B. N. Pushpakaran, and S. B. Bayne, “GaN Technology for Power Electronic Applications: A Review,” *J Electron Mater*, vol. 45, no. 6, pp. 2673–2682, Jun. 2016, doi: 10.1007/S11664-016-4435-3/METRICS.

[108] S. T. Haider, M. A. Shah, D. G. Lee, and S. Hur, “A Review of the Recent Applications of Aluminum Nitride-Based Piezoelectric Devices,” *IEEE Access*, vol. 11, pp. 58779–58795, 2023, doi: 10.1109/ACCESS.2023.3276716.

[109] A. P. Serro *et al.*, “A comparative study of titanium nitrides, TiN, TiNbN and TiCN, as coatings for biomedical applications,” *Surf Coat Technol*, vol. 203, no. 24, pp. 3701–3707, Sep. 2009, doi: 10.1016/J.SURFCOAT.2009.06.010.

[110] R. del Castillo, K. Chochlidakis, P. Galindo-Moreno, and C. Ercoli, “Titanium Nitride Coated Implant Abutments: From Technical Aspects And Soft tissue Biocompatibility to Clinical Applications. A Literature Review,” *Journal of Prosthodontics*, vol. 31, no. 7, pp. 571–578, Aug. 2022, doi: 10.1111/JOPR.13446.

[111] P. G. Chiu, D. T. Hsu, H.-K. Kim, F. G. Shi, H. S. Nalwa, and B. Zhao, “Low-k materials for microelectronics interconnects,” *Handbook of Advanced Electronic and Photonic Materials and Devices*, pp. 201–234, Jan. 2001, doi: 10.1016/B978-012513745-4/50041-X.

[112] H. Kim, “Atomic layer deposition of metal and nitride thin films: Current research efforts and applications for semiconductor device processing,” *Journal of Vacuum Science & Technology B: Microelectronics and Nanometer Structures*, vol. 21, no. 6, p. 2231, 2003, doi: 10.1116/1.1622676.

[113] “Database of ALD processes.” Accessed: Sep. 11, 2025. [Online]. Available: https://www.atomiclimits.com/alddatabase/

[114] M. Leskelä and M. Ritala, “Atomic layer deposition (ALD): From precursors to thin film structures,” *Thin Solid Films*, vol. 409, no. 1, pp. 138–146, 2002, doi: 10.1016/S0040-6090(02)00117-7.

[115] “Hydrazine - American Chemical Society.” Accessed: Sep. 11, 2025. [Online]. Available: https://www.acs.org/molecule-of-the-week/archive/h/hydrazine.html

[116] A. K. Geim and I. V. Grigorieva, “Van der Waals heterostructures,” *Nature*, vol. 499, no. 7459, pp. 419–425, Jul. 2013, doi: 10.1038/NATURE12385;SUBJMETA.

[117] Y. Kubota, K. Watanabe, O. Tsuda, and T. Taniguchi, “Deep Ultraviolet Light-Emitting Hexagonal Boron Nitride Synthesized at Atmospheric Pressure,” *Science (1979)*, vol. 317, no. 5840, pp. 932–934, Aug. 2007, doi: 10.1126/SCIENCE.1144216.

[118] K. Ahmed, R. Dahal, A. Weltz, J. Q. Lu, Y. Danon, and I. B. Bhat, "Growth of hexagonal boron nitride on (111) Si for deep UV photonics and thermal neutron detection," *Appl Phys Lett*, vol. 109, no. 11, Sep. 2016, doi: 10.1063/1.4962831.

[119] D. H. Cho, J. S. Kim, S. H. Kwon, C. Lee, and Y. Z. Lee, "Evaluation of hexagonal boron nitride nano-sheets as a lubricant additive in water," *Wear*, vol. 302, no. 1–2, pp. 981–986, Apr. 2013, doi: 10.1016/j.wear.2012.12.059.

[120] S. Jia *et al.*, "CVD growth of high-quality and large-area continuous h-BN thin films directly on stainless-steel as protective coatings," *Mater Today Nano*, vol. 16, Dec. 2021, doi: 10.1016/j.mtnano.2021.100135.

[121] S. Dub *et al.*, "Vickers Hardness of Diamond and cBN Single Crystals: AFM Approach," *Crystals (Basel)*, vol. 7, no. 12, p. 369, Dec. 2017, doi: 10.3390/cryst7120369.

[122] L. Tu *et al.*, "Cutting performance of cubic boron nitride-coated tools in dry turning of hardened ductile iron," *J Manuf Process*, vol. 56, pp. 158–168, 2020, doi: https://doi.org/10.1016/j.jmapro.2020.04.081.

[123] J. H. C. Yang, K. Teii, C.-C. Chang, S. Matsumoto, and M. Rafailovich, "Biocompatible Cubic Boron Nitride: A Noncytotoxic Ultrahard Material," *Adv Funct Mater*, vol. 31, no. 4, p. 2005066, Jan. 2021, doi: https://doi.org/10.1002/adfm.202005066.

[124] O. Mishima, J. Tanaka, S. Yamaoka, and O. Fukunaga, "High-Temperature Cubic Boron Nitride P-N Junction Diode Made at High Pressure," *Science (1979)*, vol. 238, no. 4824, pp. 181–183, Oct. 1987, doi: 10.1126/SCIENCE.238.4824.181.

[125] M. F. Plass, W. Fukarek, S. Mändl, and W. Möller, "Phase identification of boron nitride thin films by polarized infrared reflection spectroscopy," *Appl Phys Lett*, vol. 69, no. 1, pp. 46–48, Jul. 1996, doi: 10.1063/1.118113.

[126] S. Hong *et al.*, "Ultralow-dielectric-constant amorphous boron nitride," *Nature*, vol. 582, no. 7813, pp. 511–514, 2020, doi: 10.1038/s41586-020-2375-9.

[127] Y. Li, J. Guo, W. Zheng, and F. Huang, "Amorphous boron nitride for vacuum-ultraviolet photodetection," *Appl Phys Lett*, vol. 117, no. 2, p. 023504, Jul. 2020, doi: 10.1063/5.0007606.

[128] A. C. Khot *et al.*, "Amorphous Boron Nitride Memristive Device for High-Density Memory and Neuromorphic Computing Applications," *ACS Appl Mater Interfaces*, vol. 14, no. 8, pp. 10546–10557, Mar. 2022, doi: 10.1021/acsami.1c23268.

[129] C. Y. Chen *et al.*, "Tailoring amorphous boron nitride for high-performance two-dimensional electronics," *Nat Commun*, vol. 15, no. 1, p. 4016, 2024, doi: 10.1038/s41467-024-48429-4.

[130] X. Zhang and J. Meng, *Recent progress of boron nitrides*. 2019. doi: 10.1016/b978-0-12-815468-7.00004-4.

[131] P. M. Revabhai, R. K. Singhal, H. Basu, and S. K. Kailasa, "Progress on boron nitride nanostructure materials: properties, synthesis and applications in hydrogen storage and analytical chemistry," *J Nanostructure Chem*, vol. 13, no. 1, pp. 1–41, 2023, doi: 10.1007/s40097-022-00490-5.

[132] J. D. Ferguson, A. W. Weimer, and S. M. George, "Atomic layer deposition of boron nitride using sequential exposures of BCl3 and NH3," *Thin Solid Films*, vol. 413, no. 1–2, pp. 16–25, 2002, doi: 10.1016/S0040-6090(02)00431-5.

[133] B. Mårlid, M. Ottosson, U. Pettersson, K. Larsson, and J. O. Carlsson, "Atomic layer deposition of BN thin films," *Thin Solid Films*, vol. 402, no. 1–2, pp. 167–171, 2002, doi: 10.1016/S0040-6090(01)01706-0.

[134] M. Weber *et al.*, "Boron Nitride Nanoporous Membranes with High Surface Charge by Atomic Layer Deposition," *ACS Appl Mater Interfaces*, vol. 9, no. 19, pp. 16669–16678, 2017, doi: 10.1021/acsami.7b02883.

[135] J. Olander, L. M. Ottosson, P. Heszler, J. O. Carlsson, and K. M. E. Larsson, "Laser-assisted atomic layer deposition of boron nitride thin films," *Chemical Vapor Deposition*, vol. 11, no. 6–7, pp. 330–337, 2005, doi: 10.1002/cvde.200506365.

[136] T. R. Briggs and V. Migrdichian, "The Ammonium Carbamate Equilibrium," *J Phys Chem*, vol. 28, no. 11, pp. 1121–1135, Nov. 1924, doi: 10.1021/j150245a001.

[137] E. P. Egan, J. E. Potts, and G. D. Potts, "Dissociation Pressure of Ammonium Carbamate," *Ind Eng Chem*, vol. 38, no. 4, pp. 454–456, Apr. 1946, doi: 10.1021/ie50436a027.

[138] R. N. Bennett, P. D. Ritchie, D. Roxburgh, and J. Thomson, "The system ammonia + carbon dioxide + ammonium carbamate. Part I.—The equilibrium of thermal dissociation of ammonium carbamate," *Transactions of the Faraday Society*, vol. 49, no. 0, pp. 925–929, 1953, doi: 10.1039/TF9534900925.

[139] D. Janjic, "Etude de l'èquilibre de dissociation du carbamate d'ammonium à l'aide d'un appareil nouveau," *Helv Chim Acta*, vol. 47, no. 7, pp. 1879–1883, Jan. 1964, doi: https://doi.org/10.1002/hlca.19640470726.

[140] N. Wen and M. H. Brooker, "Ammonium Carbonate, Ammonium Bicarbonate, and Ammonium Carbamate Equilibria: A Raman Study," *J Phys Chem*, vol. 99, no. 1, pp. 359–368, Jan. 1995, doi: 10.1021/j100001a054.

[141] B. R. Ramachandran, A. M. Halpern, and E. D. Glendening, "Kinetics and Mechanism of the Reversible Dissociation of Ammonium Carbamate: Involvement of Carbamic Acid," 1998. [Online]. Available: https://pubs.acs.org/sharingguidelines

[142] S. X. Li *et al.*, “Prolonged photostability in hexagonal boron nitride quantum emitters,” *Commun Mater*, vol. 4, no. 1, Dec. 2023, doi: 10.1038/s43246-023-00345-8.

[143] M. Ritala, M. Leskelä, E. Rauhala, and P. Haussalo, “Atomic Layer Epitaxy Growth of TiN Thin Films,” *J Electrochem Soc*, vol. 142, no. 8, p. 2731, Aug. 1995, doi: 10.1149/1.2050083.

[144] J. Verbeeck, S. Van Aert, and G. Bertoni, “Model-based quantification of EELS spectra: Including the fine structure,” *Ultramicroscopy*, vol. 106, no. 11-12 SPEC. ISS., pp. 976–980, Oct. 2006, doi: 10.1016/j.ultramic.2006.05.006.

[145] G. te Velde *et al.*, “Chemistry with ADF,” *J Comput Chem*, vol. 22, no. 9, pp. 931–967, Jul. 2001, doi: https://doi.org/10.1002/jcc.1056.

[146] J. Tao, J. P. Perdew, V. N. Staroverov, and G. E. Scuseria, “Climbing the Density Functional Ladder: Nonempirical Meta--Generalized Gradient Approximation Designed for Molecules and Solids,” *Phys Rev Lett*, vol. 91, no. 14, p. 146401, Sep. 2003, doi: 10.1103/PhysRevLett.91.146401.

[147] E. Caldeweyher *et al.*, “A generally applicable atomic-charge dependent London dispersion correction,” *J Chem Phys*, vol. 150, no. 15, p. 154122, Apr. 2019, doi: 10.1063/1.5090222.

[148] E. Van Lenthe and E. J. Baerends, “Optimized Slater-type basis sets for the elements 1–118,” *J Comput Chem*, vol. 24, no. 9, pp. 1142–1156, Jul. 2003, doi: https://doi.org/10.1002/jcc.10255.

[149] E. van Lenthe, E. J. Baerends, and J. G. Snijders, “Relativistic regular two-component Hamiltonians,” *J Chem Phys*, vol. 99, no. 6, pp. 4597–4610, Sep. 1993, doi: 10.1063/1.466059.

[150] C. Gonzalez and H. B. Schlegel, “Reaction path following in mass-weighted internal coordinates,” *J Phys Chem*, vol. 94, no. 14, pp. 5523–5527, Jul. 1990, doi: 10.1021/j100377a021.

Acknowledgments

It doesn't feel easy to express my gratitude to all the people who have been by my side during the last four years, but here goes my best try.

First, I want to thank my supervisors, Prof. Dr. Mato Knez and Dr. Catalina Mansilla. Mato, thank you for your knowledge, guidance, good humor and, most importantly, for always believing I could achieve all that we set out to do. Catalina, muchas gracias por darme la oportunidad de ser parte de CTECH y por todo lo que he aprendido a lo largo de esta experiencia.

Gracias infinitas a Marina y a Susan, las mejores compañeras y amigas que podría haber encontrado. Esta tesis también es mérito vuestro, por vuestro apoyo, ayuda y todo lo que nos hemos reído juntas. Nire taldean beti. Mil gracias a Silvia, que vino para aprender de mí, pero terminó enseñándome cosas mucho más importantes que la ciencia.

To the former and current members of the Nanomaterials team, thank you for the good times and tunes in lab 18.

To Chris, for your unvaluable support and guidance with SEM imaging, you always cared about my tricky samples as if they were yours and I will be forever thankful. To Dr. Ana Beloqui and Dr. Soledad Orellano from POLYMAT, thank you for welcoming me into your lab and for your patience teaching me everything I know about working with bacteria. To Dr. Oier Etxebeste, thank you for your help with working with fungi and for your constant, ironic words of encouragement.

I want to express my gratitude to Prof. Dr. Roland Bennewitz for giving me the opportunity of temporally being part of his wonderful team and explore the world of haptics. I could not have received a warmer welcome, and I am especially thankful to Maja, Sairam, Nedim and Fabian for their support and kindness. On the same note, I want to thank Cami, Sara, Alpcan, Viky and Mónica for making my summer in Saarbrücken a memorable one. Vielen Dank!

A mis compañeros de cafés (o tés) y escalada de nanoGUNE: Cova, Jokin, Nuria, Nico, Maryam, Samuele, Eoin, Jone, José, María, Daniel, Manu, Ortu, Julien, Yasiel, Uxue, Laura, Alba, Ane… Gracias por estar siempre dispuestos

a ayudar, por los ánimos, el apoyo, los dulces y las risas, incluso en los peores momentos. Sois la mejor parte de este centro de investigación.

A Ander, Erlaitz, Fran, Mikel, Pelayo y Yaiza, gracias por haber sido mi familia en Donosti, os echaré de menos cada día. Gracias por todos los viajes, los conciertos, las cenas, las fiestas, los planes de chicas, los partidos del Athletic, pero sobre todo gracias por hacer que terminara llorando de risa los días en los que solo tenía ganas de llorar.

A mis amigos de Valladolid, Carla, Carrasco, Coca, Marina (y Kira) y Rodri, gracias por haber estado ahí desde siempre, por todas vuestras visitas para comer helado y por hacerme un hueco en vuestras agendas cuando vuelvo.

A Diego (Carito), porque todos estos años estabas a mi lado cuando nos caíamos.

Por último, pero lo más importante, gracias a mi familia, a mi padre y a mi madre que es estupenda, a mis tíos y a mi primo Héctor, por apoyarme y hasta darme ideas, aunque no siempre entendáis lo que hago. A mi hermana Nax, gracias por ser la persona más divertida que conozco, te admiro un montón. Os quiero.

Mila esker,

Ana

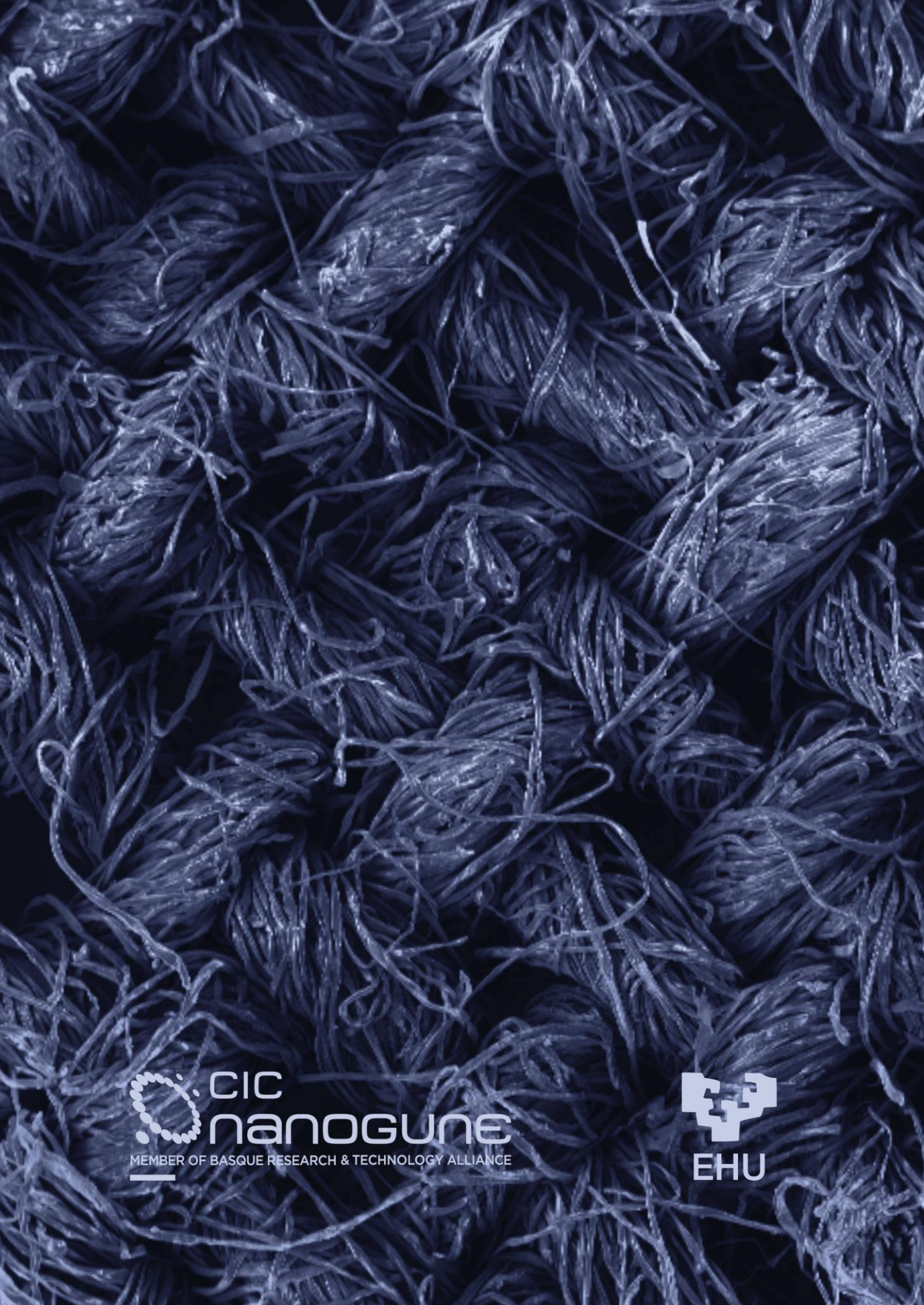
CIC
nanoGUNE
MEMBER OF BASQUE RESEARCH & TECHNOLOGY ALLIANCE
EHU